NORTHWESTERN UNIVERSITY

Numerical Studies of Lasing and Electromagnetic Fluctuations in Open Complex Systems

A DISSERTATION

SUBMITTED TO THE GRADUATE SCHOOL
IN PARTIAL FULFILLMENT OF THE REQUIREMENTS

for the degree

DOCTOR OF PHILOSOPHY

Field of Physics and Astronomy

By

Jonathan Andreasen

EVANSTON, ILLINOIS

December 2009

ABSTRACT

Numerical Studies of Lasing and Electromagnetic Fluctuations
in Open Complex Systems

Jonathan Andreasen

This dissertation explores lasing behavior and the effects of electromagnetic fluctuations in open complex systems in one dimension. It consists of three topics: thermal electromagnetic field fluctuations in open passive systems, fluctuations due to atomic interactions with external reservoirs in open active systems, and spatially nonuniform gain distributions in open systems.

Numerical models which do not require prior knowledge of cavity modes are developed to simulate fluctuations which must accompany associated dissipations. First, thermal noise is simulated in open cavities due to output coupling. The absorbing boundary of the numerical grid is treated as a blackbody which emits thermal radiation that penetrates the cavity. It is demonstrated that in the non-Markovian regime, the buildup of intracavity field noise depends on the ratio of the cavity field lifetime to the coherence time of thermal radiation. Second, fluctuations which accompany the dephasing of atomic polarization and the change of the excited state's population are simulated in dielectric slab lasers and

random lasers. This method is based on the Maxwell-Bloch equations for two-level atoms with real noise terms derived from stochastic c-number evolution equations. In random lasers, noise is found to influence lasing thresholds. In the transition from amplified spontaneous emission to clear lasing oscillation, spectral narrowing around mode frequencies is observed. Discrete lasing peaks are found to manifest themselves more clearly with partial pumping even when noise is included.

This leads to a study of the effects of optical gain nonuniformly distributed in random systems. It is demonstrated that even without gain saturation and mode competition, the spatial nonuniformity of gain can cause dramatic and complicated changes to lasing modes. Mode mixing increases as the gain distribution changes gradually from uniform to nonuniform. Furthermore, new lasing modes are created by nonuniform gain distributions. They may disappear together with existing lasing modes, thereby causing fluctuations in the local density of lasing states. Some new lasing modes are examined in detail and found to exhibit high output directionality, meaning random laser properties may be modified significantly without changing the underlying structures.

Acknowledgements

This work would not have been possible without the help of many talented people at Northwestern University and Yale University. I want to thank my advisor, Prof. Hui Cao, for guidance and support and my thesis committee members Prem Kumar, James A. Sauls, and Xu Li. Many thanks to the members of Prof. Cao's group over the years, Alexey Yamilov, Wei Fang, Heeso Noh, Qinghai Song, Xiaohua Wu, Jin-Kyu Yang, and Mikhail Erementchouk. I thank Allen Taflove and Jamesina Simpson for instruction and many helpful discussions concerning FDTD. I thank Adilson Motter for his support in my doctoral research. I also thank Christian Vanneste and Patrick Sebbah at Université de Nice-Sophia Antipolis for providing guidance during my stay in Nice. For stimulating conversations, I thank A. Douglas Stone and the members of his group at Yale University, Li Ge and Robert Tandy. The Yale Biomedical High Performance Computing Center and the Yale Faculty of Arts and Sciences HPC Center have provided the means to complete these numerical studies. I particularly thank Brian Dobbins for his support with numerical issues. To the many dedicated professors at Illinois State University, I greatly appreciate the instruction I received. They inspired in me a love for computational physics. I thank my first physics teacher, Betty Harberts, for imparting excitement about learning.

I thank my parents for helping me throughout my education and offering their support whenever needed. To my beautiful wife Myric, I am deeply grateful for her patience and encouragement along this journey towards my degree at Northwestern University.

Preface

Considering that this thesis focuses on studies of the laser (light amplification by stimulated emission of radiation), it seems appropriate to begin with the thoughts of a man largely responsible for the conception of the laser. Charles Townes, Nobel Prize winner in Physics (1964), is also a winner of the Templeton Prize, awarded for exceptional contribution to affirming life's spiritual dimension. Invited to speak at Yale University on the topic of science and religion, Townes remarked that scientists hypothesize based on principles that ultimately cannot be proven. Thus, like religion, science builds on a form of faith. This statement is not meant to equate science and religion, but merely to illustrate that science and religion are not mutually exclusive. Townes went on to exclaim that many of the scientific breakthroughs he has been privy to revealed the hidden beauty of God's creation. Based on my own Christian faith, I too believe nature has much to reveal about the different aspects of God. C. S. Lewis, the Oxford scholar and well known Christian apologist, describes this point of view elegantly in *The Four Loves*,

> Nature never taught me that there exists a God of glory and of infinite majesty. I had to learn that in other ways. But nature gave the word glory a meaning for me. I do not see how the 'fear' of God could have ever meant to me anything but the lowest prudential efforts to be safe, if I had never seen certain ominous ravines and unapproachable crags.

> And if nature had never awakened certain longings in me, huge areas of what I can now mean by 'love' of God would never, so far as I can see, have existed. A true philosophy may sometimes validate an experience of nature; an experience of nature cannot validate a philosophy. Nature will not verify any theological or metaphysical proposition; she will help us to show what it means. And not, on the Christian premises, by accident. The created glory may be expected to give us hints of the uncreated; for the one is derived from the other and in some fashion reflects it.

The research presented in this thesis has produced and is a result of "certain longings" in myself and colleagues around me. As for myself, the longing to understand basic processes of nature is not the result of a personal decision, but an awakened quality, somehow already present. That gift and these theoretical investigations, based on mathematical frameworks that, in themselves, show beauty, have inspired praise. To quote the Psalmist, "I will praise you, O Lord, with all my heart; I will tell of all your wonders. I will be glad and rejoice in you; I will sing praise to your name, O Most High."

Table of Contents

ABSTRACT 3

Acknowledgements 5

Preface 6

List of Tables 11

List of Figures 12

Chapter 1. Introduction 17

1.1. Light Scattering 17

1.1.1. Scattering Cross Section 18

1.1.2. Characteristic Length Scales 19

1.2. Lasing in Multiple Scattering Systems 21

1.2.1. Nonresonant Feedback 22

1.2.2. Resonant Feedback 25

1.2.3. Spatially Nonuniform Gain Distributions 26

1.3. Fluctuation and Dissipation 29

1.3.1. Brownian Motion 30

1.3.2. Fluctuations in Lasers 32

1.3.3. Blackbody Radiation 37

1.4. Numerical Methods 40
1.4.1. Finite-Difference Time-Domain 40
1.4.2. Parallelization 42
1.4.3. Maxwell-Bloch Equations 43
1.4.4. Transfer Matrix 51
1.4.4.1. Solving For Boundary Conditions 54
1.4.4.2. Linear Gain Model 57
1.5. Overview of this Thesis 60

Chapter 2. Thermal Electromagnetic Field Fluctuations 62
2.1. Noise Model 63
2.2. Thermal Noise in Vacuum 69
2.3. Thermal Noise in an Open Cavity 71
2.3.1. Markovian Regime 73
2.3.2. Non-Markovian Regime 74
2.4. Analytical Examination and Discussion 76

Chapter 3. Atomic State Population and Polarization Fluctuations 83
3.1. Noise Model 84
3.2. Superfluorescence 90
3.3. Lasing Behavior in a Dielectric Slab 97
3.3.1. Intensity and Spectral Behavior 102
3.3.2. Linewidth 105

Chapter 4. Effects of Noise on Random Lasers 113

4.1. Random System 115

4.2. Analysis with Linear Gain 119

4.3. From Amplified Spontaneous Emission to Lasing Oscillation 122

4.3.1. High Index Contrast 122

4.3.2. Low Index Contrast 129

4.3.2.1. Intensity 129

4.3.2.2. Spectra 131

4.3.2.3. Linewidths 140

4.3.3. Low Index Contrast–Nonuniform Gain Distribution 148

4.4. Discussion 150

Chapter 5. Spatially Nonuniform Gain Distributions 154

5.1. Numerical Methods 154

5.1.1. Biorthogonal Decomposition of Lasing Modes 156

5.1.2. Standing Wave and Traveling Wave Components 158

5.1.3. Effective Potential of a Dielectric Structure 161

5.2. Passive and Uniform Gain Systems 162

5.3. Modal Behavior with Gain Region Reduction 168

5.4. Mode Mixing 173

5.5. Lasing Mode Disappearance and Appearance 174

Chapter 6. Conclusion 184

References 189

Vita 203

List of Tables

3.1 Variables and parameters of the light, gain material, cavity, and FDTD grid settings used for the simulation of the dielectric slab ($n = 3$, $L = 1$ μm). 99

4.1 Variables and parameters of the light, gain material, cavity, and FDTD grid settings used for the simulation of the random system ($L = 6.1$ μm). 118

List of Figures

1.1 Laser system coupled to external reservoirs. 33

1.2 Two-level atom diagram. 44

2.1 Thermal noise source electric field $E_s(t_j)$... 64

2.2 FDTD-calculated energy density of blackbody radiation... 65

2.3 Temporal correlation function$\langle E_s(t_1)E_s(t_2)\rangle$ vs. $t_2 - t_1$... 67

2.4 Spatially-averaged EM energy density $U(\omega)$... 75

2.5 The number of thermal photons in individual cavity modes as L is varied... 76

2.6 The number of thermal photons in individual cavity modes as T is varied... 77

2.7 Intensity distributions of off-resonant modes. 78

2.8 Energy inside a dielectric cavity as a function of index of refraction. 79

2.9 $B_m(\tau_c, \tau) \equiv n_m/n_T(\omega_m)$ vs. the ratio of noise correlation time to cavity decay time τ_c/τ... 81

3.1 Self-Induced Transparency results... 90

3.2 Diagram of the system model used to study superfluorescence. 92

3.3 Numerical results of the output EM energy from initially-inverted two-level atoms... 93

3.4 Comparison of delay times of emission pulse... 95

3.5 The ratio ρ_3/ρ_B as a function of time... 96

3.6 Population inversion at one spatial location of low intensity ($x = L/2$). 101

3.7 Average output intensity during the last 1% of the simulation time vs. pumping rate. 102

3.8 Steady-state output intensity $I_{3pa}(\lambda)$ including noise for a dielectric slab laser. 104

3.9 Steady-state output intensity $|E(k)|^2$ including noise for $P_r = 1.10$, above the lasing threshold. 106

3.10 The Lorentz error function $L_{EF}(k)$ asymptotically approaches $A_l s$. 108

3.11 $L_{EF}(k)$ obtained for lasing mode 12 from the spectrum $|E(k)|^2$. 109

3.12 Fit of a Lorentzian curve $L(k)$ to mode 12 constructed from fitting the spectrum $|E(k)|^2$. 111

3.13 Linewidth $\delta\lambda_{12}$ and pumping rate vs. the steady-state modal intensity $\langle I_{12}(k)\rangle$. 112

4.1 Intensity distributions of representative modes in a random system with $\Delta n = 0.25$ and $\Delta n = 0.05$. 115

4.2 Transmission spectra for $\Delta n = 0.25$, $\Delta n = 0.05$, and the gain curve. 117

4.3 The frequencies k and lasing thresholds n_i of lasing modes with linear gain for a random system with index contrast $\Delta n = 0.25$. 120

4.4 The lasing frequencies k and thresholds n_i of modes with linear gain in a weakly scattering random system. 121

4.5 Average steady-state intensity vs. pumping rate for a random structure with $\Delta n = 0.25$. 123

4.6 Original steady-state intensity $|E(k)|^2$ compared to the three-adjacent-point averaged spectrum $I_{3pa}(k)$. 124

4.7 Steady-state intensity spectra $I_{3pa}(k)$ comparisons with and without noise for a random system with dielectric layers of $\Delta n = 0.25$. 126

4.8 Steady-state intensity spectrum iteratively three-point averaged $I_{i3pa}(k)$ for a random system with dielectric layers of $\Delta n = 0.25$ and $P_r = 1.10$. 128

4.9 $\langle I(k) \rangle$ vs. P_r of the random structure with low index contrast. 130

4.10 Steady-state intensity spectra $|E(k)|^2$ *without* noise. 133

4.11 Steady-state intensity spectra $I_{3pa}(k)$ in the ASE region. 135

4.12 Steady-state intensity spectra $I_{3pa}(k)$ for increasing P_r as lasing with resonant feedback finally manifests. 137

4.13 Steady-state intensity spectrum iteratively averaged $I_{i3pa}(k)$ compared to the spectrum without noise for a random system with dielectric layers of $\Delta n = 0.05$ and $P_r = 2.00$. 138

4.14 Steady-state intensity spectra $I_{3pa}(k)$ for large pumping rates P_r with clear lasing action. 139

4.15 Steady-state intensity spectra $I_{3pa}(k)$ comparisons with and without noise for a random system with $\Delta n = 0.05$. 141

4.16 Mode frequencies vs. pumping rate for random structure with index contrast $\Delta n = 0.05$. 142

4.17 Average steady-state intensity and modal intensities vs. pumping rate of the weakly scattering random structure with $\Delta n = 0.05$. 144

4.18 Spectral width of the broad peak $\delta\lambda_B$, linewidths $\delta\lambda_2$ and $\delta\lambda_5$, and corresponding average intensities vs. P_r. 145

4.19 Linewidths $\delta\lambda_5$ and $\delta\lambda_2$ and pumping rate vs. the steady-state modal intensities $\langle I_{5,2}(k)\rangle$ for a random system with $\Delta n = 0.05$. 147

4.20 Steady-state intensity spectra $I_{3pa}(k)$ comparisons with and without noise for random system with spatially nonuniform gain ($l_G/L = 1/3$). 149

4.21 Intensity spectra $|E(k)|^2$ taken from two subsequent time intervals for a random system in the ballistic regime. 152

5.1 Effective potential (wavelet power spectrum) $|W(x)|^2$ of the dielectric function $\epsilon_r(x)$ as a function of position x and wavelength λ. 163

5.2 A mapping of the phase θ of M_{22} for the passive 1D random system with no gain. 164

5.3 Normalized intensity $|\psi(x)|^2$ of a leaky mode - quasi mode 27 of the passive random 1D structure. 165

5.4 The frequencies of quasi modes and lasing modes with linear gain together with the decay rates of quasi modes and the lasing thresholds of lasing modes. 166

5.5 Spatial intensity distributions of quasi modes and lasing modes... 167

5.6 Frequencies and thresholds (k, n_i) of the lasing modes of the 1D random structure with gain. 169

5.7 Normalized intensity of lasing mode 17 with uniform gain $l_G = 24100$ nm and nonuniform gain $l_G = 14284$ nm. 170

5.8 Standing/traveling wave ratio $A_{ST}(x)$ (red solid lines) of lasing mode 17 with uniform gain $l_G = L$ and nonuniform gain $l_G = 14284$ nm. 171

5.9 Decomposition of lasing mode 17 in terms of passive quasi modes. 173

5.10 Real and Imaginary zero lines of M_{22}. 175

5.11 Standing/traveling wave ratio $A_{ST}(x)$ of the new lasing mode and lasing mode 17 for $l_G = 14553$ nm and $l_G = 14523$ nm. 177

5.12 Decomposition at $l_G = 14284$ nm of lasing mode 17, lasing mode 18, and the new lasing mode in terms of the quasi modes of the passive system. 179

5.13 Steady-state output intensity vs. pumping rate P_r from Maxwell-Bloch simulations with different gain spectra. 181

5.14 Emission spectra taken from two Maxwell-Bloch simulations with λ_a equal to λ_{nm} and λ_2. 182

CHAPTER 1

Introduction

1.1. Light Scattering

Light Scattering is a physical process where light interacts with a material. Due to this interaction, the light is forced to deviate from its original trajectory. Light scattering is so crucial to our everyday life that without it we cannot see the world around us. Even so, a reliable and accurate description of light was not assembled until just over 150 years ago. James C. Maxwell formulated the modern laws of electromagnetism which govern the behavior of light [**1**]. These laws, now termed Maxwell's equations, are important because they are able to describe *all* forms of electromagnetic (EM) phenomena. Moreover, they have withstood testing by over a century's worth of intense research [**2**]. Maxwell's original equations were reduced later on to a set of much simpler equations by Heaviside [**3**] and developed into their modern form by Gibbs [**4**].

In this thesis, electric conductivity, magnetic loss, and magnetic current density are not considered and thus, shall be neglected. We also set the magnetic permeability to the free-space permeability $\mu = \mu_0$. Thus, we are left with the following form of Maxwell's equations,

$$\begin{aligned} &\nabla \cdot E = 0 && \nabla \cdot H = 0 \\ &\nabla \times E = -\mu_0 \left(\partial H/\partial t\right) && \nabla \times H = \epsilon_0 \epsilon \left(\partial E/\partial t\right) + J, \end{aligned} \tag{1.1}$$

where E and H are the electric and magnetic fields, respectively, J is the electric current density, ϵ_0 is the permittivity of free space, and ϵ is the dielectric constant. For a time-independent description of EM waves, the electric and magnetic fields may be assumed to evolve as $E = E_0 \exp(-i\omega t)$, $H = H_0 \exp(-i\omega t)$, where ω is the field frequency. Equation 1.1 then reduces to the wave equation, or Helmholtz equation

$$[\nabla^2 + \epsilon k^2]E = 0, \tag{1.2}$$

where $k = \omega/c$ is the field wavevector.

1.1.1. Scattering Cross Section

A solution of Eq. 1.2 has a flux, or current K through a surface S defined by

$$K = \mathrm{Im} \int dS \cdot E^* \nabla E. \tag{1.3}$$

What is usually termed the "differential scattering cross section," is the ratio of output flux through the surface within an element of solid angle $d\Omega$ to the input flux per unit surface [**5**].

$$\sigma(\theta) = \frac{dK_{out}/d\Omega}{dK_{in}/dS}. \tag{1.4}$$

θ is the angle between the deviated trajectory and the original trajectory. Specific values of $\sigma(\theta)$ require the knowledge of the solution E. Nevertheless, we may define a set of useful characteristic length scales when light experiences multiple scattering.

1.1.2. Characteristic Length Scales

When light scatters multiple times, the "scattering mean free path" ℓ_s is simply defined as the average distance light travels between two consecutive scattering events. ℓ_s is dependent on the density of states and the spatial correlation of the dielectric function [**5**]. In our case, scattering is induced by a spatially inhomogeneous dielectric function $\epsilon(r)$, where r is the position variable. We consider a dielectric function where the correlation function

$$\langle \epsilon(r)\epsilon(r') \rangle \neq 0. \tag{1.5}$$

If the correlation range is of the same order of magnitude as the free-space wavelength $\lambda = 2\pi/k$, then scattering becomes anisotropic. Put more simply, within a certain time scale τ_t, scattering occurs in preferred directions. After a time τ_t has passed, memory of the incident direction before $-\tau_t$ is lost. The length scale associated with τ_t is calculated as $\ell_t = v_g \tau_t$, where v_g is the group velocity. The quantity ℓ_t is known as the "transport mean free path." It can be shown that

$$\ell_t = \frac{\ell_s}{1 - \langle \cos\theta \rangle}. \tag{1.6}$$

ℓ_t can be thought of as the average distance a wave travels before its direction is randomized. Due to the term $\langle \cos\theta \rangle$, which can be found through the differential scattering cross section of Eq. 1.4, $\ell_t > \ell_s$, as expected. $\ell_t = \ell_s$ when scattering is isotropic, i.e., when scattering has no preferred direction and there is no memory of previous scattering

events. When scattering does depend on previous events, the light will clearly travel a larger distance before that memory is erased.

If the size of the system L is smaller than or equal to the transport mean free path ($L \leq \ell_t$), the system is in the ballistic regime. In this case, photons travel out of the system before their directions can be randomized. If ℓ_t is much smaller than the system size, but much larger than the field wavelength $\lambda = 2\pi/k$, the system is in the diffusive regime. In this case, photons are forced on a random walk through the system with diffusivity D before exiting. If v is the transport velocity of the photons, the average distance a photon travels before exiting is $\ell_x = vL^2/D$. A third regime exists in which the effective wavelength [**6**] of light in the random medium is approximately $2\pi\ell_s$. In this case, light may be spatially localized, as suggested early on by John [**7, 8**]. The localization length ξ itself may be calculated from the dependence of transmission $\mathcal{T}$ of an ensemble of random systems of different lengths as $\xi^{-1} = -d\left\langle \ln \mathcal{T} \right\rangle / dL$. Note that in the localization regime, $\xi < L$.

Two other length scales that will be of interest in this thesis are the gain length ℓ_g and the amplification length ℓ_p [**9**]. The gain length is simply the average distance a wave travels before its intensity has increased by a factor e^{+1}. After the wave has traveled a distance ℓ_g, it has undergone a random walk. Thus, the straight line distance from the beginning of the random walk to the end of the random walk $\ell_p \leq \ell_g$. Without scattering, $\ell_p = \ell_g$. In a three-dimensional system in the diffusive regime,

$$\ell_p = \sqrt{\frac{\ell_t \ell_g}{3}}. \tag{1.7}$$

The amplification process shall be discussed in the next section.

1.2. Lasing in Multiple Scattering Systems

LASER is an acronym for "light amplification by stimulated emission of radiation," said to be coined by Gordon Gould in 1957. However, concepts which necessarily needed to be in place for the laser to be realized were developed in part by Albert Einstein. He calculated the probability coefficients (now termed "Einstein coefficients") for the molecular absorption and emission of radiation [**10**]. Gordon, Zeiger, and Townes took advantage of these concepts and described a device which could be used as a microwave amplifier in 1955 [**11**]. They called this device a MASER (microwave amplification by stimulated emission of radiation). A few years later, Schawlow and Townes extended their maser techniques to the visible frequency range of radiation [**12**], and called the device an "optical maser." Gould shortened this to laser [**13**].

Conventional lasers consist of a resonant cavity and amplifying material [**14**]. A pumping mechanism excites the amplifying material to provide stimulated emission. The faster the atoms of the amplifying material can be pumped from their ground state to their excited state, the higher the emitted intensity of the laser. Such lasers are usually built to minimize scattering which avoids loss. Loss means a lower emission intensity at the lasing frequency. Scattered photons are not necessarily lost from the cavity, but from the particular lasing mode of the cavity. However, if the scattered photons can be contained inside the laser cavity long enough to make a round trip, light amplification will be enhanced by stimulated emission. This recirculation of light, or feedback, allows amplified output. Light, an EM wave, behaves as any wave in that it may add to another wave constructively or destructively. If photons scatter multiple times and do not return to their initial location after one round trip, it is impossible to form a spatial resonance. This type

of feedback is termed nonresonant feedback. In this case, the wave intensities merely add together giving amplification as $|A_{EM}|^2 + |A_{EM}|^2 = 2|A_{EM}|^2$. However, if scattered photons return to their initial location on a time-reversed path, light experiences constructive interference. This constructive interference results in a larger amplification because amplitudes add together rather than intensities, i.e., $|A_{EM} + A_{EM}|^2 = |2A_{EM}|^2 = 4|A_{EM}|^2$. This type of feedback is termed resonant feedback. The spatial resonance formed in the laser is called a "lasing mode." Multiple modes may exist, as shown later, in a random laser.

1.2.1. Nonresonant Feedback

A laser (although not a random laser) with nonresonant feedback was realized in 1966 [**15, 16**]. A benefit of a laser with nonresonant feedback is that the average frequency of emission is stable. This is so because the average frequency only depends on the transition frequency of the gain atoms and not on the spatial resonances formed by the laser cavity. Because the frequency is independent of the dimensions of the laser system, this makes it possible to develop an optical frequency standard [**17**].

As the pumping rate increases, the spectral width of this peak narrows. The drawback is that the linewidth of the atomic resonance is typically much larger than the linewidth of a lasing mode formed by a spatial resonance of the laser cavity. The frequency dependence of the gain length ℓ_g gives the highest photon generation rate at the peak of the gain spectrum. Due to the independence of the transport mean free path ℓ_t on frequency (at least within the gain spectrum), the loss rate of photons within the gain spectrum is fairly constant. With an increased pumping rate, the generation rate of photons nearest the

atomic transition frequency matches the loss rate first. Outside this frequency region, the generation rate of photons is still less than the loss rate. This allows the photon density around the atomic transition frequency to build up quickly. The increase of photon density near the maximum of the gain spectrum results in a drastic narrowing of the emission linewidth.

Another phenomenon which possesses similar characteristics as mentioned above is amplified spontaneous emission (ASE). A spectrum resulting from ASE also narrows as the pumping rate is increased. However, the net gain available during the process of ASE is less than the loss rate from leakage out of the laser cavity. Lasing with nonresonant feedback occurs with a gain greater than the leakage loss rate.

To find a condition on the system dimensions required for lasing with nonresonant feedback, an examination using the diffusion equation may be undertaken. Though interference is neglected in the diffusion equation, it may be considered as an accurate description since feedback does not depend on interference. As discussed in Sec. 1.1.2, when $L \gg \ell_t \gg \lambda$, the system is in the diffusive regime. In this case, the energy density of photons $W(\vec{r}, t)$ may be described by the diffusion equation. This description ignores the wave nature of light and treats photons as particles. The system under consideration is in the nonsteady-state diffusive regime [**18**] in that the energy density of photons varies in time due to multiple scattering and gain. Thus, we may employ Ficke's second law with the addition of gain. The photon energy density must increase with the rate v/ℓ_g proportional to the current energy density in the presence of uniform and linear gain. The

diffusion coefficient is given by $D = v\ell_t/3$. The diffusion equation is then

$$\frac{\partial W(\vec{r},t)}{\partial t} = D\nabla^2 W(\vec{r},t) + \frac{v}{l_g} W(\vec{r},t). \tag{1.8}$$

Letokhov solved [**19**] the diffusion equation and found the condition on the system volume L^3 necessary to achieve an exponential increase in the photon energy density. The threshold is

$$L^3 = \left(\frac{\ell_t \ell_g}{3}\right)^{3/2}. \tag{1.9}$$

Basically, a photon must travel through the random medium long enough to generate at least one extra photon before exiting the system, i.e., $\ell_x \geq \ell_g$. Quickly examining this inequality also yields Eq. 1.9.

$$\begin{aligned} \ell_x &\geq \ell_g \\ \frac{3L^2}{\ell_t} &\geq \ell_g \\ L &\geq \sqrt{\frac{\ell_t \ell_g}{3}}. \end{aligned} \tag{1.10}$$

This prediction was verified experimentally by Lawandy *et al.* [**20, 21**].

From the discussion of length scales in the previous section, diffusion occurs when $\ell_t \ll L < \xi$. In 1D, however, diffusion cannot occur. Traveling through layers of a spatially varying index of refraction results in a series of reflections and transmissions of the wave. If the reflections are weak enough, the wave may travel through multiple layers before the direction is reversed (in 1D, this means it has been "randomized"). This length

was already defined as the transport mean free path ℓ_t. But because the wave returns on its original path and this same process will occur until the wave intensity is depleted, this length scale is also close to the localization length ξ (see [**22**] for a precise mathematical argument). Thus, since $\xi \approx \ell_t$, the diffusion condition above may not be satisfied and the only regimes available in 1D are the localization regime $\xi < L$ and the ballistic regime $\xi > L$. In this thesis, we shall mostly concentrate on the ballistic regime. Based loosely on Letokhov's argument above, one can say a larger amount of gain is required for lasing to occur in the ballistic regime.

1.2.2. Resonant Feedback

A random laser with resonant feedback was first realized by Cao *et al.* [**23, 24**] and a short time later in various other systems [**25, 26, 27**]. Emission spectra in these cases are characterized by complex fine structures, as opposed to the relatively broad emission spectra obtained from lasing with nonresonant feedback. As discussed earlier, these narrow spectral lines arise from recurrent light scattering [**28**] resulting in the formation of spatial resonances. The emitted light is coherent, with similar characteristics of a conventional laser, but in a medium more easily made (e.g., by grinding a laser crystal [**29**] or even using chicken breast [**30**]). In this thesis, we shall see the formation of such resonances numerically. Complex fine structures are observed to rise out of a broad spectrum background as the pumping rate is increased.

There are two major regimes of interest concerning lasing with resonant feedback: (i) strongly scattering regime, (ii) weakly scattering regime (see [**31**] for a general overview). When there is multiple scattering, strong scattering makes it easier for photons to return

to the same coherence volume ($\sim \lambda^3$) visited before. This provides resonant feedback for lasing since it is extremely likely for photons to return to the beginning of their random walk. However, lasing with resonant feedback may also occur when scattering is weak [**25, 26, 32, 30, 33**].

Due to some confusion [**30**] over what constitutes an optical cavity in a weakly scattering system, Wu *et al.* investigated the matter experimentally and numerically [**33**]. Interference of light, which is typically ignored in the diffusion equation, was found to be significant even in weakly scattering systems. As mentioned earlier, for lasing to occur at all in weakly scattering systems, optical gain needs to be very large. Thus, even though scattering may be unlikely within the spatial gain region, weak feedback can greatly amplify the little light that is scattered. The interference of this scattered light determines the lasing frequency. They showed numerically that lasing may occur between only 2 scatterers. Because amplified spontaneous emission (ASE) may also produce sharp spectral lines [**34**], Wu and Cao showed that ASE spikes and lasing peaks are statistically different and that lasing peaks have a larger threshold [**35, 36**]. This information shall be useful as we investigate the influence of noise on random lasers.

1.2.3. Spatially Nonuniform Gain Distributions

From the previous two sections, we have seen that lasing modes in random media behave quite differently depending on the scattering characteristics of the media. In the strongly scattering regime, lasing modes have a nearly one-to-one correspondence with the localized modes of the passive system [**37, 38**]. Due to small mode volume, different localized modes may be selected for lasing through local pumping of the random medium [**39, 37**].

The nature of lasing modes in weakly scattering open random systems is still under discussion [**40**]. In systems which are diffusive on average, prelocalized modes may serve as lasing modes [**41**]. In general, however, the quasi modes of weakly scattering systems are very leaky. Hence, they exhibit a large amount of spatial and spectral overlap. For inhomogeneous dielectric systems with uniform gain distributions, even linear contributions from gain induced polarization bring about a coupling between quasi modes of the passive system [**42, 43**]. Thus, lasing modes may be modified versions of the corresponding quasi modes. However, Vanneste *et al.* found that when considering uniformly distributed gain, the first lasing mode appears to correspond to a single quasi mode [**44**]. The study was done near the threshold pumping rate and nonlinear effects did not modify the modes significantly. Far above threshold, it was found that lasing modes consist of a collection of constant flux states [**45**]. Mode mixing in this regime is largely determined by nonlinear effects from gain saturation.

Remaining near threshold, pumping a local spatial region, and including absorption outside the pumped region found lasing modes to differ significantly from the quasi modes of the passive system [**46**]. This change is attributed to a reduction of the effective system size. More surprisingly, recent experiments [**30, 33**] and numerical studies [**47**] showed the spatial characteristics of lasing modes change significantly by local pumping even without absorption in the unpumped region. It is unclear how the lasing modes are changed in this case by local pumping. Here, we carry out a detailed study of random lasing modes in a weakly scattering system with a nonuniform spatial distribution of linear gain. Mode competition depends strongly on the gain material properties, e.g., homogeneous vs. inhomogeneous broadening of the gain spectrum. Ignoring gain saturation (usually

responsible for mode competition) and absorption, we find that spatial nonuniformity of linear gain alone can cause mode mixing. We decompose lasing modes in terms of quasi modes and find them to be a superposition of quasi modes close in frequency. The more the gain distribution deviates from being uniform, more quasi modes contribute to a lasing mode.

Furthermore, still considering linear gain and no absorption outside the gain region, we find that some modes stop lasing no matter how high the gain is. We investigate how the lasing modes disappear and find that new lasing modes may appear as well. The new lasing modes typically exist for specific distributions of gain and disappear as the distribution is further altered. They appear at various frequencies for several different gain distributions without including absorption or nonlinearity.

Because of the randomness, it is difficult to intentionally produce lasing modes in random lasers with desirable properties. In a conventional laser, the available lasing modes are typically fixed once the cavity is made. Finer control over lasing properties can be obtained, for example, by carefully placing the gain medium in a cavity to reduce the lasing threshold [**48**] or using specific pumping profiles to select lasing modes with desirable properties [**49, 50, 51, 52**]. However, once the laser cavity is made, it is very difficult to obtain new lasing modes that have no correspondence to the resonant modes of the cold cavity if nonlinearity is negligible. To have more control over random laser properties, the structures themselves may be adjusted by selecting the scatterer size [**53, 54, 55, 56, 57**] and separation [**58, 59**], changing the scattering structure with temperature [**60, 61**] or electric field [**62**], or creating defects [**63**]. For random lasers operating in the localization region, spatially non-overlapping modes may be selected for

lasing through local pumping of the random system [**64**]. In the case of diffusive random lasers, far above the lasing threshold, nonlinear interaction between the light field and the gain medium alters the lasing modes [**45**]. Without gain nonlinearity, local pumping and absorption in the unpumped region can also change the lasing modes significantly [**46**] because the system size is effectively reduced. Recent experiments [**30, 33**] and numerical studies [**47**] show that even without absorption in the unpumped region, the spatial characteristics of lasing modes may vary with local pumping. In this case, the lasing modes still correspond to the quasi modes of the passive system. However, spatial inhomogeneity in the refractive index can introduce a linear coupling of resonant modes mediated by the polarization of gain medium [**43**].

In this thesis, we demonstrate that the new lasing modes do not correspond to the modes of the passive system or any lasing modes in the presence of uniform gain. They can lase independently of other lasing modes when gain saturation is taken into account. Furthermore, the new lasing modes can have highly directional output. These findings may offer an easy and fast way of dramatically changing the random laser properties without modifying the underlying structures.

1.3. Fluctuation and Dissipation

The relation between fluctuation and dissipation in systems coupled to external reservoirs is so fundamental that it spans many areas of science, from laser physics to botany. The fluctuation-dissipation theorem states that the damping of a system is actually determined by the fluctuating forces of the reservoir which also introduces fluctuations into the

system [**65**]. This theorem has its roots in Brownian motion, which provides an instructive and intuitive picture of the relation between fluctuation and dissipation.

1.3.1. Brownian Motion

The biologist Brown noticed a "peculiar character" in the motions of pollen particles immersed in water [**66**]. These particle motions are independent of each other, irregular and never cease, dependent on particle size, fluid viscosity, and reservoir temperature, and independent of particle composition and density [**67**]. These observations, along with Einstein's independently formulated theory [**68**], would eventually lead to the conclusion that when a particle is immersed in a fluid, it is pushed in a random way by the much smaller particles in the reservoir and the velocity of the particle is reduced by a force proportional to its velocity.

As a simple example, we consider Brownian motion in one dimension by following the examination by Haken [**69**]. A force $\mathbf{F}(t)$ pushes a particle according to Newton's second law of motion $\mathbf{F}(t) = m\dot{\mathbf{v}}(t)$, where $\mathbf{v}(t)$ is the particle's velocity, $\dot{\mathbf{v}}(t)$ is the time derivative of the velocity, and we take the particle's mass $m = 1$. $\mathbf{F}(t)$ is composed of both a frictional force $\mathbf{F}_f(t)$ and random pushes forward and backward $\mathbf{F}_r(t)$. It can be expressed as

$$\begin{aligned} \mathbf{F}(t) =& \mathbf{F}_f(t) + \mathbf{F}_r(t) \\ =& -\kappa\mathbf{v}(t) + A_r \sum_j \delta(t - t_j)(\pm 1)_j, \end{aligned} \tag{1.11}$$

where κ is the damping rate, A_r is the strength each random push, and $(\pm 1)_j$ represents the direction of each push j. The random sequence of times t_j are when pushes occur. We

assume that there are an equal number of left pushes as right pushes so that $\langle \mathbf{F}_r(t) \rangle = 0$. The fundamental equation for Brownian motion then reads

$$\dot{\mathbf{v}}(t) = -\kappa \mathbf{v}(t) + \mathbf{F}_r(t). \tag{1.12}$$

For times $t \gg 1/\kappa$, the solution to Eq. 1.12 is

$$\mathbf{v}(t) = \int_0^t \exp[-\kappa(t-\tau)] \mathbf{F}_r(\tau) d\tau. \tag{1.13}$$

Averaging over all pushes yields an average velocity of zero [$\langle \mathbf{v}(t) \rangle = 0$]. Thus, the particle does not move *on average*. However, we are interested in the character of these fluctuations and not just the behavior on average. For example, although $\langle \mathbf{F}_r(t) \rangle = 0$, the correlation function deduced quickly from Eq. 1.11 is $\langle \mathbf{F}_r(t) \mathbf{F}_r(t') \rangle = Q\delta(t-t')$, where $Q \propto A_r^2$ and is essentially the strength of the fluctuations. In other words, the random force $\mathbf{F}_r$ at time t is only correlated with itself at time $t' = t$ and is thus proportional to the square of the strength of each random push. Otherwise, each random push is independent of the others making the correlation zero. Similarly, examining the correlation function of the velocity from Eq. 1.13 gives

$$\langle \mathbf{v}(t) \mathbf{v}(t') \rangle = \int_0^t \int_0^{t'} \exp\{-\kappa[(t-\tau) + (t'-\tau')]\} \langle \mathbf{F}_r(\tau) \mathbf{F}_r(\tau') \rangle \, d\tau' d\tau. \tag{1.14}$$

If use the fact that $\langle \mathbf{F}_r(t) \mathbf{F}_r(t') \rangle = Q\delta(t-t')$ and continue with the assumption that $t + t' \gg 1/\kappa$, then Eq. 1.14 reduces to

$$\langle \mathbf{v}(t) \mathbf{v}(t') \rangle = \frac{Q}{2\kappa} \exp[-\kappa(t-t')]. \tag{1.15}$$

We may relate the energy of the particle $\frac{1}{2}\langle \mathbf{v}^2(t)\rangle$ to the thermal energy of the surrounding reservoir $\frac{1}{2}k_BT$, where k_B is Boltzmann's constant and T is the temperature of the reservoir, and we have assumed thermal equilibrium has been reached. This relation yields $Q/4\kappa = k_BT/2$ or

$$Q = \kappa\,(2k_BT)\,. \tag{1.16}$$

Notice that the strength of the fluctuations Q is directly proportional to the dissipation κ of energy due to the frictional force.

Equation 1.16 is a simple form of the fluctuation-dissipation theorem. As the strength of the dissipation increases, so does the strength of the fluctuations. By this theorem, decay constants, which are typically easier to calculate, allow us to determine the strength of corresponding fluctuations. This will be the basis of much to follow in this thesis.

1.3.2. Fluctuations in Lasers

Melvin Lax was among the first to describe this process in lasers and obtain the Langevin theory of noise sources [**70**]. Equation 1.12, used to describe Brownian motion, is in fact known as a Langevin equation. Paul Langevin, the French physicist, developed the general form of the equation to describe stochastic processes in gases [**71**]. Such equations describe the rate of change of some quantity, in the case of Eq. 1.12 particle velocity, and include some random function which describes some stochastic process.

Each stochastic physical model has its own Langevin equation. For each source of dissipation, there is an accompanying fluctuation. A conventional laser consists of an electromagnetic (EM) field trapped inside a resonant cavity along with some amplifying

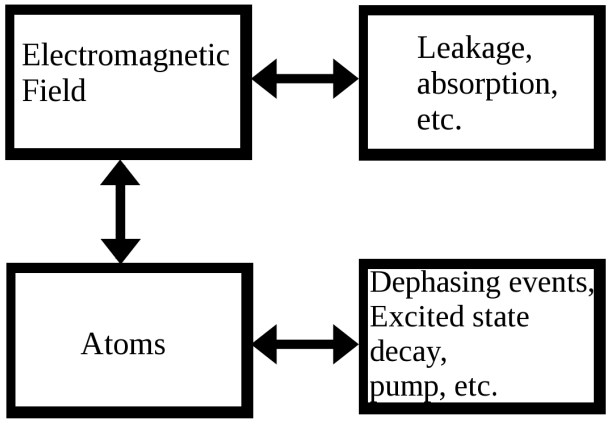

Figure 1.1. Laser systems (left) and the sources of dissipation due to external reservoirs (right). The electromagnetic field couples to both the atoms providing optical gain and external reservoirs through leakage or absorption. The atoms also couple to external reservoirs via dephasing events, spontaneous emission, or through the pumping mechanism.

material [**14**]. Figure 1.1 shows the EM field coupled to the atoms providing optical gain for the laser. Also shown is the coupling of both the EM field and gain atoms to external reservoirs. This coupling induces dissipation and therefore, must induce fluctuations as well.

For an EM field inside a resonant cavity, there are two dissipation mechanisms seen in Fig. 1.1: (i) leakage or output coupling (ii) intracavity absorption. The EM field couples to the outside environment by exiting the resonant cavity. The cavities considered in this thesis are open cavities because light is confined by a leaky dielectric material rather than by perfectly reflecting boundaries. This source of loss (or dissipation) must be accompanied by a source of fluctuation with properties determined by the decay rate out of the cavity. The next section, Sec. 1.3.3, shall discuss this interaction of the EM field with an external reservoir in more detail. The EM field also couples to absorbing material

inside the resonant cavity. In this case, fluctuations accompany local dissipations inside the cavity with the fluctuation properties determined by the local absorption coefficient. These fluctuations have already been taken into account [**72, 73**], and will not be discussed in this thesis.

The atoms inside a resonant cavity also experience dissipation. Figure 1.1 shows three dissipation mechanisms: (i) dephasing events (ii) excited state decay (iii) pumping (from atomic ground state to excited state). Dephasing events include lattice vibrations or atomic collisions which cause the atomic polarization to spontaneously change phase [**74**]. This source of "dissipation" of the polarization must also induce fluctuation to the polarization. Excited state decay includes non-radiative recombination and spontaneous emission. The spontaneous emission of photons (caused by the spontaneous decay of the atomic excited state to the ground state) is partly due to a coupling to vacuum fields and "radiation reaction" [**75**]. Modeling atoms as a dipoles, the radiation reaction is the field generated by the dipole and acting on the dipole. These two mechanisms combine to cause spontaneous emission of photons when the atom is in its excited state. However, when the atom is in its ground state, these two mechanisms cancel each other, thus making "spontaneous absorption" impossible. Therefore, only fluctuations associated with spontaneous decay need to be included. However, atoms may be intentionally pumped from their ground state to their excited state via an external energy source (which may be electrical or optical in nature). This must also induce fluctuation.

Dissipation may usually be taken into account fairly easily since one only needs to append an exponentially decaying term to the evolution equations being considered. In

the absence of strong light confinement, which holds for macroscopic systems, these decaying terms can even be considered independent of the local density of states (LDOS). Hence, they do not have a dependence on spatial location nor frequency. The inclusion of fluctuations, on the other hand, is more complicated. Marcuse solved the rate equations for light intensity and electron population including noise terms [**76**] to illustrate the effect of noise on lasing mode dynamics [**77**]. Gray and Roy extended the formulation by adding noise to the field equation in order to study the laser line shape [**78**]. Starting from a microscopic Hamiltonian, Kira *et al.* developed a semiconductor theory including spontaneous emission to describe semiconductor lasers [**79**]. While considerable progress has been made, these models remain in the modal picture. Knowledge of mode properties is required to characterize the noise, making it difficult to study complex systems in which the mode information is unknown *a priori*. Without invoking the modal picture, Hofmann and Hess obtained the quantum Maxwell-Bloch equations including spatiotemporal fluctuations [**80**]. Although it was useful to study spatial and temporal coherence in diode lasers, this formalism was based on the assumption that the temporal fluctuations of carrier density and photon density were statistically independent, which often broke down above the lasing threshold. A finite-difference time-domain (FDTD) simulation of microcavity lasers including quantum fluctuations was also done recently [**81**]. This simplified model added white Gaussian noise as a source to the electric field. The noise amplitude depended only on the excited state's lifetime. The dephasing process, which is much faster than the excited state's population decay, should induce more noise but was neglected.

The importance of and *usefulness* of noise has been recognized by many. A random laser amplifier operates below the lasing threshold, but amplifies the total power. As shall be shown in this thesis, noise plays a significant role in this fairly complicated and poorly understood regime. Random laser amplifiers can be useful because they operate in the linear regime where nonlinear interactions of light with the gain medium do not yet play a role. Far above the lasing threshold, the random laser operates in the highly nonlinear regime which has drastic consequences for lasing modes [**45**]. Beenakker studied [**82**] thermal noise in a static random laser amplifier and predicted excess noise consisting of amplified spontaneous emission due to a continuous spectrum of overlapping modes (see Sec. 1.2.1). Fedorov and Skipetrov recently showed [**83**] that photon noise [**84**] from a random laser amplifier carries information about dynamic properties of the medium itself. Fluctuating properties of the medium, such as the type of particle motion and velocity may be obtained merely by studying the fluctuations of the number of photocounts. Furthermore, Lodahl *et al.* studied transport [**85**] of quantum noise through random systems. They found [**86**] that photon noise provides information about spatial quantum correlations of light traveling through the random medium. Cao *et al.* found [**87**] that the photon statistics of random lasers to be helpful in distinguishing between lasing with resonant feedback and nonresonant feedback.

The finite-difference time-domain (FDTD) method, which shall be discussed in-depth in Sec. 1.4.1, is the direct time-domain calculation of EM fields without prior knowledge of modes. One goal here is to develop FDTD-based numerical methods to simulate fluctuations in macroscopic systems caused by interactions of atoms and photons with reservoirs. Such noise shall be incorporated in a way compatible with the FDTD method,

that allows one to study the light-matter interaction in complex systems without prior knowledge of modes. The effective modal behavior is an *emergent* property that results from temporal evaluation of the EM fields. These methods open a new approach for the study of quantum mechanical aspects of radiation in macroscopic systems with classical electrodynamics simulations. This approach has the potential to permit rigorous theoretical investigations of noise in the area of quantum optics and of open systems such as chaotic open cavities. The dynamics of such systems are, in particular, very difficult to study using standard frequency domain methods.

1.3.3. Blackbody Radiation

In the previous section, the field inside of an optical cavity was shown to interact with an external reservoir outside the cavity. This external reservoir may be a black body, i.e., a body that absorbs all incident radiation. This black body, however, must remain at thermal equilibrium. Thus, it must emit radiation in addition to absorbing it. An empty cavity that reaches thermal equilibrium then has the same intensity and frequency distribution as the black body [**88**]. This noisy radiation is known as blackbody radiation. Planck first derived the frequency distribution of blackbody radiation by considering a large number of identical resonators with discrete energies [**89**]. We shall derive the form of this frequency distribution in a similar way in Sec. 2.1.

In the modal picture, widely used in quantum optical studies, noise is introduced to the quantum operator of a leaky cavity mode $\hat{a}(t)$. If the fluctuating force $\hat{\Gamma}(t)$ has the same properties as the random pushes of Brownian motion in Sec. 1.3.1, then $\hat{a}(t)$ satisfies

the reservoir-averaged commutation relation [**69**]

$$\left\langle [\hat{a}(t), \hat{a}^{\dagger}(t)] \right\rangle = 1. \tag{1.17}$$

$\hat{a}(t)$ evolves according to the Langevin equation

$$\frac{d\hat{a}(t)}{dt} = \left(-i\omega - \frac{1}{\tau} \right) \hat{a}(t) + \hat{\Gamma}(t), \tag{1.18}$$

where ω is the mode frequency and τ is the mode lifetime. Without the Langevin force $\hat{\Gamma}(t)$ (thermal fluctuations in this case), $[\hat{a}^{\dagger}(t), \hat{a}(t)] = \exp(-2t/\tau)$, which tends to zero. This means the operator $\hat{a}(t)$ eventually becomes a classical quantity and contradicts quantum mechanics.

The amplitude of classical noise accompanying the field decay is proportional to $\sqrt{n_T}$, as discussed later, where n_T is the thermal photon number. At room temperature the number of thermal photons at visible frequencies ($\hbar\omega \sim 1$ eV) is on the order of 10^{-17}. This can be interpreted in a quantum mechanical picture as that most of the time there are no thermal photons at visible frequencies in the system. Although thermal noise is quantitatively insignificant at optical frequencies, its proper treatment constitutes an essential part of the exact quantum-mechanical theory of lasers. Early laser theory introduces the thermal noise via a heatbath made up of loss oscillators or absorbing atoms [**70, 90**]. It accounts for light absorption inside the cavity. For a laser cavity whose loss only comes from the output coupling, the thermal noise is attributed to the thermal radiation that penetrates the cavity through the coupling [**91, 92**]. Thus the amount of thermal noise depends on the mode decay rate τ, which must be known in order to solve the Langevin equation for the field operator (Eq. 1.18). For open complex cavities, e.g., the ones made

of random structures, the required information of modes is unknown *a priori*. Thus, it is desirable to be able to study the noise of a cavity field without prior knowledge of cavity modes. Additional problems with the modal picture are, (i) if the cavity is very leaky, the significant overlap of modes in frequency makes it difficult to distinguish one mode from another; (ii) In the presence of nonlinearity, strictly speaking, the modes do not exist.

As already mentioned, by introducing noise to the electromagnetic (EM) field without invoking the modal picture, thermal noise is added in the time domain without the knowledge of cavity modes. It can be applied to simulations of complex open systems where modes are unknown prior to the FDTD calculations. This approach is especially useful for very leaky cavities where modes overlap strongly in frequency, as the thermal noise related to the cavity leakage is introduced naturally without distinguishing the modes. Therefore, this method may be applied to a whole range of quantum optics problems. Although, in this thesis, the FDTD calculation of thermal noise is performed on 1D systems, the implementation in 2D and 3D systems is straightforward. Note that this approach does not apply to the simulation of zero-point fluctuation which have a different physical origin than thermal noise. However, this numerical method can be used to study the dynamics of EM fields which are excited by arbitrarily correlated noise sources. One potential application is noise radar [**93, 94**]. The propagation, reflection and scattering of ultra-wideband signals utilized by noise radar can be easily simulated using the method developed here.

1.4. Numerical Methods

In this section, the numerical methods used to carry out the study of lasing and electromagnetic (EM) fluctuations in open complex systems are described. First, the finite-difference time-domain (FDTD) method, which is purely a simulation of classical EM fields, is discussed and how the method may be parallelized for faster computations. Auxiliary differential equations used to simulate two-level atoms along with the FDTD method are then presented. Finally, the transfer matrix method, a frequency-domain calculation also used to simulate purely classical EM fields in one dimension, is addressed.

1.4.1. Finite-Difference Time-Domain

The finite-difference time-domain (FDTD) method is a powerful computational electrodynamics modeling technique. First introduced by Yee in 1966 [**95**] and significantly advanced by Taflove [**96**], this method has been developed for decades and become more and more popular with the increase in computer power. The basic idea of this method is to apply the central difference approximation to Maxwell's curl equations, both in space and time. FDTD does not invoke the rotating-wave approximation nor the slowly varying envelope approximation. FDTD thus enables the accurate characterization of complex inhomogeneous structures for which analytical methods may be ill-suited.

As in Eq. 1.1, electric conductivity, magnetic loss, and magnetic current density are not considered and thus, shall be neglected. The magnetic permeability is set to the free-space permeability $\mu = \mu_0$. Ampere's law and Faraday's law can be written in differential

form

$$\begin{aligned} \frac{\partial E}{\partial t} =& \frac{1}{\epsilon}\left[\nabla \times H - J\right] \\ \frac{\partial H}{\partial t} =& -\frac{1}{\mu_0}\left[\nabla \times E\right]. \end{aligned} \tag{1.19}$$

E is the electric field, H is the magnetic field, and ϵ is the electrical permittivity. E and H are vectors in three dimensions and consequently have three components each yielding six coupled scalar equations to solve. The electric current density J may act as a source of energy. To solve the above equations numerically, the spatial and temporal derivatives are replaced by finite differences that are central-difference in nature. The three components of E and H are staggered in space according to the "Yee lattice." This implicitly enforces the two remaining Maxwell equations (Gauss' law relations). Furthermore, E and H are also staggered in time so that the finite-difference equations may be solved by a simple "leapfrog" method. This avoids problems involved with simultaneous equations and matrix inversion [**96**]. The result is a second-order accurate algorithm (according to the size of the discritization steps).

The FDTD algorithm may be clearly and more simply demonstrated in one dimension (1D). Also, we only consider 1D problems in this thesis, so we only write the discretized equations here for 1D. Assuming propagation along the x direction, the numerical spatial grid is discretized into segments of length Δx denoted by i and temporal steps Δt denoted by n. The electric field is aligned along the z direction and the magnetic field aligned along the y direction. When discretized, the magnetic field at spatial grid location i and time step n, for example, is expressed as $H_y|_i^n$. Discretized versions of Ampere's law and

Faraday's law are then written as

$$E_z|_{i-1/2}^{n+1/2} = E_z|_{i-1/2}^{n-1/2} + \frac{\Delta t}{\epsilon_{i-1/2}} \left[\frac{H_y|_i^n - H_y|_{i-1}^n}{\Delta x} - J_{i-1/2}^n \right].$$

$$H_y|_i^{n+1} = H_y|_i^n + \frac{\Delta t}{\mu_0} \left[\frac{E_z|_{i+1/2}^{n+1/2} - E_z|_{i-1/2}^{n+1/2}}{\Delta x} \right]. \tag{1.20}$$

A time step loop is easily implemented which iteratively updates $E_z|_{i-1/2}^{n+1/2}$ and $H_y|_i^{n+1}$ by the leapfrog method. The simulation is usually begun with an excitation current density, e.g., a Gaussian-sinusoidal source J_{source}, added to E_z. The above equations are very general and may be used with nearly any type of dielectric material. A random dielectric structure, for example, may be simulated through an electric permittivity which has values that vary spatially in a random way.

1.4.2. Parallelization

The FDTD algorithm may be parallelized [**97**] through the single-program multiple-data technique, which is particularly well suited to solve this problem via the message passing interface (MPI) [**98**]. There is only one program for all the processors, but each one operates independently of the others. The 1D space is divided into several sub-spaces, each sub-space being associated with one processor. All the processors execute exactly the same FDTD program but each one operates on its own sub-space. Communication is only required at the interfaces of the sub-spaces. For example, if the space is split between two sub-spaces at the location between i and $i + 1/2$, then to calculate $H_y|_i^{n+1}$, the value of $E_z|_{i+1/2}^{n+1/2}$ needs to be passed from the neighboring sub-space. Likewise, the

value of $H_y|_i^n$ would need to be passed to the neighboring sub-space in order to calculate $E_z|_{i+1/2}^{n+1/2}$.

If there are M grid points and P processors, each processor works on M/P grid points and exchanges information only with its left and right neighbor. At each step, the amount of calculation done by each processor is proportional to M/P, while the data each processor exchanges with its neighbor is fixed. The ratio of computation/exchange scales as M/P. However, FDTD only requires the exchange of two variables E and H in 1D, amounting to 16 bytes for double precision variables. Transferring this small amount of data does not require a large bandwidth of the computer network. But there is always some delay, or latency, associated with transferring variables over a network. Latency is usually the limiting factor for these 1D FDTD-MPI calculations.

1.4.3. Maxwell-Bloch Equations

To simulate the nonlinear process of lasing along with classical behavior of light according to Sec. 1.4.1, we incorporate the Bloch equations for two-level atoms (TLAs) [**99**]. The Bloch equations describe the time evolution of the atomic polarization and energy level populations under the influence of applied signals. Figure 1.2 shows a simple diagram illustrating the two-level atom model. An external pumping mechanism excites the atom from the ground state into the excited state. The atom decays from the excited state into the ground state, thereby emitting radiation.

For simple systems isolated from outside influencing factors (e.g., free particle, particle in a box, harmonic oscillator, hydrogen atom), a self-contained Hamiltonian and wavefunction can describe the system as completely as quantum mechanics allows [**100**].

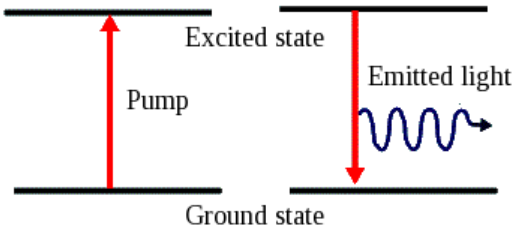

Figure 1.2. Two-level atom diagram. An external pump excites the atom from the ground state into the excited state. The atom decays from the excited state into the ground state, thereby emitting radiation.

When N systems begin coupling to a heat bath or external field, however, a complete description may not be available. This is called a "mixed state". What may be known, instead of every projection of the mixed state onto each eigenstate, is the probability for a system in the ensemble to be in the m-th state u_m. These probabilities are given in terms of the density matrix.

Starting off simply, we examine a wavefunction for one atom

$$\psi_a(r,t) = \sum_m c_m(t) u_m(r), \tag{1.21}$$

with the normalization condition given as $\sum_m c_m^* c_m = 1$. We can now introduce the density matrix as $\rho \equiv |\psi_a\rangle \langle\psi_a|$, which in a simple TLA yields

$$\rho = \begin{pmatrix} c_1 c_1^* & c_1 c_2^* \\ c_2 c_1^* & c_2 c_2^* \end{pmatrix} \tag{1.22}$$

or $\rho_{jk} = \langle j|\psi_a\rangle \langle\psi_a|k\rangle = c_j c_k^*$. The normalization condition now corresponds to

$$\mathrm{Tr}\,\rho = 1, \tag{1.23}$$

which we will use later. Though we started with a wavefunction for one atom (whose projections may or may not be completely known), we can consider the elements of the density matrix to be an ensemble average over N atoms. Working with these probabilities, we will never know the phase relations between $|j\rangle$ and $|k\rangle$, but we will have the benefit of being able to describe the evolution of our system.

To find the evolution of the system in time we examine the time-dependent Schrödinger Equation:

$$i\hbar\frac{\partial\psi_a}{\partial t} = H\psi_a. \tag{1.24}$$

The Hamiltonian is separated into two parts $H = H_0 + H_I$. H_0 corresponds to the stationary Hamiltonian of the atom when no field is present and is given by

$$H_0 = -\frac{1}{2}\hbar\omega_a \begin{pmatrix} 1 & 0 \\ 0 & -1 \end{pmatrix}, \tag{1.25}$$

where $\hbar = 1.05 \times 10^{-34}$ m^{2}kg/s is the reduced Planck's constant and ω_a is the atomic transition frequency between states $|1\rangle$ and $|2\rangle$. The interaction part of the Hamiltonian H_I corresponds to the electric field E_z interacting with a dipole [**101**]. The dipole moment is simply the product of the electronic charge magnitude e and the off-diagonal electron position operator Q

$$\begin{aligned} H_I &= E_z \cdot eQ \\ &= eq_0E_z \begin{pmatrix} 0 & 1 \\ 1 & 0 \end{pmatrix}. \end{aligned} \tag{1.26}$$

Mathematically, the position operator (or equivalently, the dipole operator) is off-diagonal because it has odd parity and the states $|1\rangle$ and $|2\rangle$ have definite parity, i.e., $\langle 1|\,\vec{q}\,|1\rangle = \langle 2|\,\vec{q}\,|2\rangle = 0$. Physically, this is so because if purely in state $|1\rangle$ or $|2\rangle$, the electron position has a uniform probability distribution around the positively charged nucleus of the atom meaning no dipole moment is generated. But if the electron is in a superposition state, there is an unbalance and a dipole moment is created. Note that we assume $\langle j|\,\vec{q}\,|k\rangle = \langle k|\,\vec{q}\,|j\rangle = q_0$ in Eq. 1.26. In other words we simply choose the phases of the states $|1\rangle$ and $|2\rangle$ (without loss of generality [**102**]) so that $Q_{12} = Q_{21} = q_0$.

The total Hamiltonian is now

$$H = \hbar \begin{pmatrix} -\omega_a/2 & \Omega_R \\ \Omega_R & \omega_a/2 \end{pmatrix} \tag{1.27}$$

where $\Omega_R \equiv \gamma E_z/\hbar$ is the Rabi frequency and $\gamma \equiv eq_0$ is the dipole coupling term. The Schrödinger equation can be recast in terms of the density matrix elements which is then known as the Liouville equation.

$$\begin{aligned} \dot{\rho} &= \left|\dot{\psi}_a\right\rangle \langle\psi_a| + |\psi_a\rangle \left\langle\dot{\psi}_a\right| \\ &= \frac{-i}{\hbar} H\,|\psi_a\rangle\,\langle\psi_a| + \frac{i}{\hbar}\,|\psi_a\rangle\,\langle\psi_a|\,H \\ &= \frac{-i}{\hbar}[H,\rho] \end{aligned} \tag{1.28}$$

Using Eq. 1.27 we find

$$\dot{\rho} = -i \begin{pmatrix} \Omega_R(\rho_{21} - \rho_{12}) & -\omega_a\rho_{12} + \Omega_R(\rho_{22} - \rho_{11}) \\ \omega_a\rho_{21} - \Omega_R(\rho_{22} - \rho_{11}) & -\Omega_R(\rho_{21} - \rho_{12}) \end{pmatrix}. \tag{1.29}$$

The elements of ρ correspond to the following: (ρ_{11}) population of the atomic ground state, (ρ_{22}) population of the atomic excited state, (ρ_{12}, ρ_{21}) complex amplitude of the electron's displacement [**103**].

We now introduce the fictitious Bloch vector $\vec{\rho} = \rho_1\hat{e}_1 + \rho_2\hat{e}_2 + \rho_3\hat{e}_3$ via

$$\begin{aligned} \rho_1 \equiv& \rho_{12} + \rho_{21} \\ \rho_2 \equiv& i(\rho_{12} - \rho_{21}) \\ \rho_3 \equiv& \rho_{22} - \rho_{11}. \end{aligned} \tag{1.30}$$

ρ_3 corresponds to the atomic population *inversion* while ρ_1 and ρ_2 correspond to the atomic polarization components.

Note that due to the normalization condition discussed earlier (Eq. 1.23), $\rho_1^2+\rho_2^2+\rho_3^2 = 1$. This is proven below. $\rho_1^2 + \rho_2^2 + \rho_3^2$ can be written as

$$\begin{aligned} &[\rho_{12} + \rho_{21}]^2 + [i(\rho_{12} - \rho_{21})]^2 + [\rho_{22} - \rho_{11}]^2 \\ =&(\rho_{12}^2 + \rho_{21}^2 + 2\rho_{12}\rho_{21}) + (-1)(\rho_{12}^2 + \rho_{21}^2 - 2\rho_{12}\rho_{21}) + \rho_{22}^2 + \rho_{11}^2 - 2\rho_{22}\rho_{11} \\ =&4\rho_{12}\rho_{21} + \rho_{22}^2 + \rho_{11}^2 - 2\rho_{22}\rho_{11}. \end{aligned} \tag{1.31}$$

Now, from our previous normalization condition Eq. 1.23, $(\rho_{11} + \rho_{22})^2 = \rho_{22}^2 + \rho_{11}^2 + 2\rho_{22}\rho_{11} = 1$, giving $\rho_{22}^2 + \rho_{11}^2 - 2\rho_{22}\rho_{11} = 1 - 4\rho_{22}\rho_{11}$ so that

$$\rho_1^2 + \rho_2^2 + \rho_3^2 = 1 + 4\rho_{12}\rho_{21} - 4\rho_{22}\rho_{11} = 1 \tag{1.32}$$

if $\rho_{12}\rho_{21} = \rho_{22}\rho_{11}$, which is true without decoherence. In general, $\rho_{12}\rho_{21} \leq \rho_{22}\rho_{11}$ because the positiveness of $\vec{\rho}$ must be preserved [**104**]. By introducing decoherence (as is done below) Eq. 1.32 will not be strictly true and $\rho_1^2 + \rho_2^2 + \rho_3^2 \leq 1$. We shall use this condition to test our numerical implementation later on.

We can now find the rate equations for the Bloch vector using Eq. 1.29 and the definitions given above.

$$\begin{aligned}
\dot{\rho}_{12} &= -i[-\omega_a\rho_{12} + \Omega_R(\rho_{22} - \rho_{11})] \\
&\rightarrow \frac{1}{2}\dot{\rho}_1 - \frac{i}{2}\dot{\rho}_2 = \frac{1}{2}\omega_a\rho_2 - \frac{i}{2}(-\omega_a\rho_1 + 2\Omega_R\rho_3) \\
\dot{\rho}_3 &= \dot{\rho}_{22} - \dot{\rho}_{11} = -i[-2\Omega_R(\rho_{12} - \rho_{21})] = -2\Omega_R\rho_2
\end{aligned} \tag{1.33}$$

Putting this in matrix form gives

$$\begin{pmatrix} \dot{\rho}_1 \\ \dot{\rho}_2 \\ \dot{\rho}_3 \end{pmatrix} = \begin{pmatrix} 0 & \omega_a & 0 \\ -\omega_a & 0 & 2\Omega_R \\ 0 & -2\Omega_R & 0 \end{pmatrix} \begin{pmatrix} \rho_1 \\ \rho_2 \\ \rho_3 \end{pmatrix}. \tag{1.34}$$

We then add phenomenological decay rates due to decoherence and the excited state's lifetime (which includes spontaneous emission and non-radiative recombination). In the absence of strong light confinement, which holds for macroscopic systems, T_1 and T_2 can be considered independent of the local density of states (LDOS). Hence, they do not have a dependence on spatial location nor frequency. We also include incoherent pumping of atoms from level 1 to level 2. The rate is proportional to the population in level 1, and

can be written as $(P_r/T_1)\rho_{11}$. The final equations read as

$$\begin{aligned}\begin{pmatrix}\dot{\rho}_1\\ \dot{\rho}_2\\ \dot{\rho}_3\end{pmatrix} &= \begin{pmatrix}0 & \omega_a & 0\\ -\omega_a & 0 & 2\Omega_R\\ 0 & -2\Omega_R & 0\end{pmatrix}\begin{pmatrix}\rho_1\\ \rho_2\\ \rho_3\end{pmatrix}\\ &\quad - \begin{pmatrix}1/T_2 & 0 & 0\\ 0 & 1/T_2 & 0\\ 0 & 0 & 1/T_1(1+P_r)\end{pmatrix}\begin{pmatrix}\rho_1\\ \rho_2\\ \rho_3-\rho_3^{(s)}\end{pmatrix},\end{aligned} \tag{1.35}$$

where $\rho_3^{(s)}$ represents the steady-state value of ρ_3 when $E_z = 0$. The polarization is found through the expectation value of the dipole moment operator as $p = -e\,\mathrm{Tr}(\rho Q) = -|\gamma|\rho_1$. The total polarization P_z of N atoms in a volume V is $P_z = (N/V)p = -(N/V)|\gamma|\rho_1$ and enters into Maxwell's equations as

$$\begin{aligned}\frac{\partial E_z}{\partial t} &= \frac{1}{\epsilon}\frac{\partial H_y}{\partial x} - \frac{1}{\epsilon}\frac{\partial P_z}{\partial t}\\ \frac{\partial H_y}{\partial t} &= -\frac{1}{\mu_0}\frac{\partial E_z}{\partial x}.\end{aligned} \tag{1.36}$$

Equations 1.35 and 1.36 comprise the Maxwell-Bloch equations and are commonly used to simulate lasers. The most commonly used method of solving the Maxwell-Bloch equations is the "strongly coupled method." With Δt being the time step, E_z and ρ are both computed at $n\Delta t$, $(n+1)\Delta t$, *etc.*, while H_y is computed at $(n-1/2)\Delta t$, $(n+1/2)\Delta t$, *etc.* This produces equations with coupled terms such as $E_z^{n+1}\rho^{n+1}$ that must be solved by a predictor-corrector scheme (as used in [**99**]) or a fixed-point procedure, both of which

are computationally inefficient. Therefore, we use a weakly coupled method that is easily implemented and efficient for 1D systems.

The weakly coupled method was put forth by Bidégaray [**105**]. The electric field E_z is computed at times $n\Delta t$, $(n+1)\Delta t$, but ρ is calculated at $(n-1/2)\Delta t$, $(n+1/2)\Delta t$, thereby decoupling those discretized equations and creating a simple leap-frog type propagation system for 1D. This is similar to the FDTD method itself (Sec. 1.4.1).

The total number of atoms N are split equally among each grid cell to give $N_s = N/M$, where M is the number of grid cells. Thus, all quantities are defined at each individual grid point. Furthermore, we use ρ_{22} instead of ρ_3 which allows us to forcibly keep the number of atoms constant via the relation $\rho_{11} = N_s - \rho_{22}$. The Maxwell-Bloch equations shall be discretized later in this thesis (Sec. 3.1), when fluctuations are introduced.

As a mathematical aside, some find it useful to analytically precondition the equations as

$$\begin{aligned} \rho_1 \equiv & u_1 e^{-t/T_2} \\ \rho_2 \equiv & u_2 e^{-t/T_2} \\ \rho_{22} \equiv & u_{22} e^{-t/T_1} \end{aligned} \tag{1.37}$$

and solve u_i instead of ρ_i. This works well with higher accuracy for larger grid cells because numerical stiffness [**106**] from time stepping the exponential terms disappears. This preconditioning, however, is not employed in this thesis because it results in terms containing $\exp(t/T_2)$ which diverge numerically when $t \geq 710T_2$ for double precision

calculations. This divergence is not a problem for short time scales, but the simulations we have in mind are orders of magnitude longer.

1.4.4. Transfer Matrix

In an altogether different method, the propagation of electromagnetic fields through 1D layers in the frequency domain may be described by the transfer matrix method. A field E_0 transmitted through an interface with transmissivity t is given by $E = tE_0$. Now, an incoming wave p_0 is both transmitted and reflected from an interface. We denote the reflected wave by q_0 and after reaching the other side of the material (whatever the structure of that material may be) we again have a transmitted wave p_N and reflected wave q_N. This can be represented in matrix form by

$$\begin{pmatrix} p_N \\ q_N \end{pmatrix} = M \begin{pmatrix} p_0 \\ q_0 \end{pmatrix}.$$

Now we are free to impose whatever boundary conditions we like. The conditions for an incoming signal only are $q_0 = p_N = 0$ giving

$$\begin{aligned} 0 &= M_{11} p_0 \\ q_N &= M_{21} p_0. \end{aligned} \tag{1.38}$$

As part of the input vector, q_N may be chosen as zero. Thus, solutions satisfying $M_{11} = 0$ also satisfy the incoming-only boundary conditions (or perfect absorption). For outgoing-only signals (or perfect amplification–lasing), the boundary conditions are $p_0 = q_N = 0$ and the condition $M_{22} = 0$ defines the solutions.

The following formalism is provided by Born and Wolf [**107**]. Using their Fresnel formulae, we apply this transfer matrix to a dielectric slab of length L and index of refraction n. Considering the TE polarization, the reflection and transmission coefficients from layer 0 (air) to layer 1 (dielectric) are

$$r_a = \frac{1-n}{1+n}; t_a = \frac{2}{1+n} \tag{1.39}$$

and from layer 1 to layer 2 (air) are

$$r_b = \frac{n-1}{n+1}; t_b = \frac{2n}{n+1}. \tag{1.40}$$

The first step toward finding the complete transfer matrix is to reproduce the coefficients given by Eq. 1.39, which can cast in matrix form as

$$\begin{pmatrix} t_a \\ 0 \end{pmatrix} = c_0 \begin{pmatrix} 1 \\ r_a \end{pmatrix} \tag{1.41}$$

The solution is the following matrix

$$c_0 = \begin{pmatrix} \frac{1}{t_b} = \frac{n+1}{2n} & \frac{r_b}{t_b} = \frac{n-1}{n+1}\frac{n+1}{2n} \\ \frac{r_b}{t_b} = \frac{n-1}{n+1}\frac{n+1}{2n} & \frac{1}{t_b} = \frac{n+1}{2n} \end{pmatrix} = \frac{1}{2n}\begin{pmatrix} n+1 & n-1 \\ n-1 & n+1 \end{pmatrix}. \tag{1.42}$$

In the next step, we allow the fields to travel through the layer, yielding the next part of the transfer matrix

$$b_1 = \begin{pmatrix} e^{i\tilde{k}_m nL} & 0 \\ 0 & e^{-i\tilde{k}_m nL} \end{pmatrix}, \tag{1.43}$$

where $\tilde{k}_m$ is the complex wavevector of mode number m. The final step in finding the complete transfer matrix for this dielectric slab is to satisfy Eq. 1.40 with the matrix c_1, found in the same way as c_0. Thus, the entire transfer matrix is given by

$$M = c_1 b_1 c_0 = \frac{1}{t_a t_b} \left(\begin{array}{c|c} e^{i\tilde{k}_m nL} + r_a r_b e^{-i\tilde{k}_m nL} & r_a e^{-i\tilde{k}_m nL} + r_b e^{i\tilde{k}_m nL} \\ \hline r_b e^{-i\tilde{k}_m nL} + r_a e^{i\tilde{k}_m nL} & r_a r_b e^{i\tilde{k}_m nL} + e^{-i\tilde{k}_m nL} \end{array} \right). \tag{1.44}$$

To verify this, examine the total transmission given by

$$\begin{aligned} \mathcal{T} &= \frac{M_{11}M_{22} - M_{12}M_{21}}{M_{22}} \\ &= \frac{e^{i\tilde{k}_m nL}}{t_a t_b} \left[\frac{(r_b^2 - 1)(r_a^2 - 1)}{1 + r_a r_b e^{2i\tilde{k}_m nL}} \right]. \end{aligned} \tag{1.45}$$

The same expression can be found analytically [**108**] from

$$\mathcal{T} = \frac{E_+(x = L^+)}{E_+(x = 0^-)}. \tag{1.46}$$

The field is transmitted through the first interface and reaches the second interface as

$$E_1(x = L^-) = t_a E_+(x = 0^-) e^{i\tilde{k}_m nL}. \tag{1.47}$$

It then partially reflects off the second interface (dielectric to air) and again off the first interface (dielectric to air also) and back giving E_2, then again giving E_3 and so forth.

$$\begin{aligned} E_2(x = L^-) &= E_1 \left(r_b^2 e^{2i\tilde{k}_m nL} \right) \\ E_3(x = L^-) &= E_2 \left(r_b^2 e^{2i\tilde{k}_m nL} \right) = E_1 \left(r_b^2 e^{2i\tilde{k}_m nL} \right)^2 \\ E_+(x = L^-) &= E_1 + E_2 + E_3 + \dots \\ &= E_1(1 + \eta + \eta^2 + \dots) = \frac{E_1}{1 - \eta} \\ \mathcal{T} &= \frac{t_b E_+(x = L^-)}{E_+(x = 0^-)} = \frac{t_a t_b e^{i\tilde{k}_m nL}}{1 - r_b^2 e^{2i\tilde{k}_m nL}}, \end{aligned} \tag{1.48}$$

where $\eta \equiv r_b^2 e^{2i\tilde{k}_m nL}$. From Eqs. 1.39 and 1.40, $t = 1 + r$ and as a consequence $t_a^2 t_b^2 = (1 + r_a)^2(1 + r_b)^2$ which is equivalent to $(r_a^2 - 1)(r_b^2 - 1)$ since $r_a = -r_b$. Thus, Eq. 1.48 is equivalent to Eq. 1.45.

1.4.4.1. Solving For Boundary Conditions. For the incoming-only boundary conditions, we set $M_{11} = 0$ and solve for $\tilde{k}_m = k_m + i(k_i)_m$. Note that $k_m = 2\pi/\lambda_m$ is the free space wavenumber of mode m.

$$\begin{aligned} M_{11} &= \frac{1}{t_a t_b} \left[e^{ik_m nL - (k_i)_m nL} + r_a r_b e^{-ik_m nL + (k_i)_m nL} \right] = 0 \\ \mathrm{Re}M_{11} &= \cos(k_m nl) \left(e^{-(k_i)_m nL} + r_a r_b e^{(k_i)_m nL} \right) = 0 \\ \mathrm{Im}M_{11} &= \sin(k_m nL) \left(e^{-(k_i)_m nL} - r_a r_b e^{(k_i)_m nL} \right) = 0 \end{aligned} \tag{1.49}$$

There are two sets of solutions here

$$\begin{aligned} A)\, &\sin(k_m nL) = 0 \\ &e^{-(k_i)_m nL} + r_a r_b e^{(k_i)_m nL} = 0 \\ B)\, &\cos(k_m nL) = 0 \\ &e^{-(k_i)_m nL} - r_a r_b e^{(k_i)_m nL} = 0 \end{aligned} \tag{1.50}$$

For Case A

$$\begin{aligned} k_m =& \frac{\pi}{nL} m \\ (k_i)_m = k_i =& -\frac{\ln(-r_a r_b)}{2nL} \end{aligned} \tag{1.51}$$

However, for Case B

$$\begin{aligned} k_m =& \frac{\pi}{nL}(m + 1/2) \\ (k_i)_m = k_i =& -\frac{\ln(r_a r_b)}{2nL}, \end{aligned} \tag{1.52}$$

which should not exist as a solution since $r_a r_b < 0$ making k_i complex.

For the case of outgoing-only boundary conditions, a similar Case A yields

$$\begin{aligned} k_m =& \frac{\pi}{nL} m \\ (k_i)_m = k_i =& \frac{\ln(-r_a r_b)}{2nL}. \end{aligned} \tag{1.53}$$

For this simple case we already know what the result should be. Transmission reaches a maximum when

$$2nL = m\lambda \tag{1.54}$$

yielding in our specific situation

$$k_m = \frac{\pi}{nL} m; m = \pm 1, \pm 2, \ldots \tag{1.55}$$

which is exactly the same solution as case A.

The field distribution for these boundary conditions inside the cavity can be calculated using $b_1(x)c_0$. The field at any point for incoming-only boundary conditions is

$$E_m(x) = \frac{r_b}{t_b} e^{-i\tilde{k}_m nx} + \frac{1}{t_b} e^{i\tilde{k}_m nx} \tag{1.56}$$

and for outgoing boundary conditions is

$$E_m(x) = \frac{r_b}{t_b} e^{i\tilde{k}_m nx} + \frac{1}{t_b} e^{-i\tilde{k}_m nx}. \tag{1.57}$$

The real and imaginary parts for the incoming-only boundary conditions are

$$\begin{aligned} \mathrm{Re}[E_m(x)] &= \left(\frac{n+1}{2n} e^{-k_i nx} + \frac{n-1}{2n} e^{k_i nx} \right) \cos(k_m nx) \\ \mathrm{Im}[E_m(x)] &= \left(\frac{n+1}{2n} e^{-k_i nx} - \frac{n-1}{2n} e^{k_i nx} \right) \sin(k_m nx) \end{aligned} \tag{1.58}$$

and for outgoing-only boundary conditions are

$$\mathrm{Re}[E_m(x)] = \left(\frac{n-1}{2n}e^{-k_i nx} + \frac{n+1}{2n}e^{k_i nx}\right)\cos(k_m nx)$$

$$\mathrm{Im}[E_m(x)] = \left(\frac{n-1}{2n}e^{-k_i nx} - \frac{n+1}{2n}e^{k_i nx}\right)\sin(k_m nx). \tag{1.59}$$

Note that k_i differs in sign for these two boundary conditions [compare Eqs. 1.51 and 1.53], making the real parts in both cases equal and the imaginary parts conjugates. Thus, the field distribution for outgoing-only boundary conditions is the complex conjugate of the field distribution for incoming-only boundary conditions. The biorthogonal left eigenvector is known to be the complex conjugate of the right eigenvector. Since the solutions satisfying these opposing boundary conditions *should* be biorthogonal, we find proof that they are in the fact that they are complex conjugates.

1.4.4.2. Linear Gain Model. Here, we describe the model used to simulate linear gain in a 1D system. The gain is linear in the sense that it does not depend on the electromagnetic field intensity. A lasing solution $\Psi(x)$ must satisfy the time-independent wave equation [see Eq. 1.2]

$$\left[\frac{d^2}{dx^2} + \epsilon(x,\omega)k^2\right]\Psi(x) = 0, \tag{1.60}$$

with a complex frequency-dependent dielectric function

$$\epsilon(x,\omega) = \epsilon_r(x) + \chi_g(x,\omega), \tag{1.61}$$

where $\epsilon_r(x) = n^2(x)$ is the dielectric function of the non-resonant background material. The frequency dependence of $\epsilon_r(x)$ is negligible. $\chi_g(x,\omega)$, corresponding to the susceptibility of the resonant material, is given by

$$\chi_g(x,\omega) = \frac{A_e N(x)}{\omega_a^2 - \omega^2 - i\omega\Delta\omega_a}, \tag{1.62}$$

where A_e is a material-dependent constant, $N(x)$ is the spatially dependent density of atoms, ω_a is the atomic transition frequency, and $\Delta\omega_a$ is the spectral linewidth of the atomic resonance. Equation (1.62) may be simplified by assuming the frequencies of interest ω are within a few linewidths of the atomic frequency ω_a, i.e., $\omega^2 - \omega_a^2 = (\omega + \omega_a)(\omega - \omega_a) \approx 2\omega_a(\omega - \omega_a)$. Equation (1.62) then reduces to

$$\chi_g(x,\omega) \approx \frac{iA_e N(x)}{\omega_a \Delta\omega_a[1 + 2i(\omega - \omega_a)/\Delta\omega_a]}. \tag{1.63}$$

The frequency-dependent index of refraction is

$$\begin{aligned} \tilde{n}(x,\omega) =& \sqrt{\epsilon(x,\omega)} = \sqrt{\epsilon_r(x) + \chi_g(x,\omega)} \\ =& n_r(x,\omega) + i n_i(x,\omega), \end{aligned} \tag{1.64}$$

which may then be implemented in the transfer matrix method. At this point, let us note that only 2 steps are needed to convert this classical electron oscillator model to real atomic transitions [**14**]. First, the radiative decay rate $\gamma_\parallel$ may be substituted in to Eq. (1.63) in place of a few constants. Second, and more importantly, real quantum transitions induce a response proportional to the population difference density $\Delta N(x)$.

Thus, $N(x)$ should be replaced by $\Delta N(x)$, the difference in population between the lower and upper energy levels. $\Delta N(x)$ is equivalent to $-\rho_3(x)$ in Sec. 1.4.3.

Linear gain independent of ω is obtained by working in the limit $\omega - \omega_a \ll \Delta\omega_a$, yielding

$$\chi_g(x) \approx i\frac{A_e \Delta N(x)}{\omega_a \Delta\omega_a}, \tag{1.65}$$

a purely imaginary susceptibility. We can make the definition $\chi_g(x) \equiv i\epsilon_i(x)$, where $\epsilon_i(x)$ is the imaginary part of $\epsilon(x)$. Note that $\epsilon(x)$ may include absorption [$\epsilon_i > 0$] or gain [$\epsilon_i < 0$]. We shall only consider gain here. The complex frequency-*independent* dielectric function now yields a frequency-independent index of refraction $\tilde{n}(x) = n_r(x) + in_i(x)$ which may be expressed explicitly as

$$\begin{aligned} n_r(x) =& \frac{n(x)}{\sqrt{2}}\left[\sqrt{1+\frac{\epsilon_i^2(x)}{n^4(x)}}+1\right]^{1/2} \\ n_i(x) =& \frac{-n(x)}{\sqrt{2}}\left[\sqrt{1+\frac{\epsilon_i^2(x)}{n^4(x)}}-1\right]^{1/2}. \end{aligned} \tag{1.66}$$

Furthermore, throughout this thesis, we assume n_i to be a spatially independent parameter. Thus, by solving for $n_r(x)$ in terms of $n(x)$ and n_i, the index of refraction we use in the transfer matrix method is given by

$$\begin{aligned} \tilde{n}(x) =& n_r(x) + in_i \\ =& \sqrt{n^2(x) + n_i^2} + in_i. \end{aligned} \tag{1.67}$$

1.5. Overview of this Thesis

This thesis is organized as follows. Chapter 2 discusses the simulation of thermal electromagnetic field fluctuations. Section 2.1 outlines the numerical model used in the simulation and discusses possible numerical difficulties and problems. Section 2.2 presents the results of including blackbody radiation in vacuum. Section 2.3 presents results of noise penetrating a 1D cavity. The transition from the Markovian regime to the non-Markovian regime is studied. Section 2.4 consists of a discussion and interpretation of the results. An analytical expression is found which offers further insights to the amount of noise inside an open cavity.

Chapter 3 discusses the simulation of atomic fluctuations. Section 3.1 describes the numerical model developed to include noise in the Maxwell-Bloch equations. In Section 3.2, atomic superfluorescence is simulated and the results are compared to experimental data and quantum-mechanical calculations. Section 3.3 discusses lasing behavior in a dielectric slab laser under the influence of atomic fluctuations.

Chapter 4 discusses the effects of noise on random lasers. Section 4.1 describes the generation of random structures, the characteristics of the particular structures studied, and numerical issues associated with the simulation of noise in random structures. In Section 4.2, an analysis using linear gain provides a solid basis of understanding. These results are compared to those using the Maxwell-Bloch equations both with and without noise in Sec. 4.3. Section 4.4 presents a summary of all results in this chapter.

Chapter 5 concentrates on the effects of spatially nonuniform gain in random lasers. In Section 5.1, additional numerical methods used to study the lasing modes of 1D random dielectric structures are described. A scheme for decomposing the lasing modes in terms

of quasi modes is presented. A method to separate traveling wave and standing wave components from the total electric field is introduced. Results of simulations of passive random systems and random lasers with uniform gain are discussed in Section 5.2. Modal behavior with reduction of the spatial gain region is studied in Section 5.3. Mode mixing results are presented in Section 5.4 and the disappearance and appearance of lasing modes is discussed in Section 5.5.

Conclusions based on the data in this thesis are made in Chapter 6.

CHAPTER 2

Thermal Electromagnetic Field Fluctuations

The finite-difference time-domain (FDTD) method [**96**] has been extensively used in solving Maxwell's equations for dynamic electromagnetic (EM) fields. The absorbing boundary condition based on the perfectly matched layer (PML) [**109**] allows the simulation of open systems, e.g. leaky optical cavities, in any dimension. The incorporation of auxiliary differential equations, such as the rate equations for atomic populations [**110, 111**], the Maxwell-Bloch equations for the density of states of atoms [**99, 112, 113**], and the multi-subband semiconductor Bloch equations [**114, 115**], has led to comprehensive studies of light-matter interactions. Although the FDTD method has become a powerful tool in computational electrodynamics, it is applied mostly to classical or semi-classical problems. The light field in an open cavity experiences quantum fluctuation because of its coupling to external reservoirs. In this chapter, we model the quantum noise for the cavity field as a classical noise and incorporate it into the FDTD algorithm.

The output coupling is not a local loss and thus, fluctuations cannot be added to the local EM field (i.e., at each grid point). The question is how to introduce thermal noise related to cavity leakage without knowing the leakage rate. In FDTD simulations, light escaping from an open system is absorbed by the absorbing boundary layer (ABL) which acts as the external reservoir. Since it absorbs all impinging fields, the ABL can be modeled as a black body (see Sec. 1.3.3). To remain in thermal equilibrium, the black body must radiate into the system. The blackbody radiation from the ABL propagates

into the cavity and acts as noise to the cavity field. The amount of noise penetrating the cavity depends on the cavity openness or output coupling. Our model is validated through the calculation of field noise in a one-dimensional (1D) dielectric cavity. In a good cavity where the mode lifetime τ is much longer than the coherence time of thermal radiation τ_c, we find that the average amount of thermal noise in one cavity mode agrees with the solution of the Langevin equation under the Markovian approximation. In addition to recovering the standard results, our simulations with various values of τ and τ_c illustrate the transition from the Markovian regime to the non-Markovian regime, and demonstrate that the buildup of the intracavity noise field depends on the ratio of τ_c to τ. This result is explained qualitatively by the interference effect.

2.1. Noise Model

Our numerical model is based on the key insight that the ABL normally used to bound FDTD computational grids is in effect a black body which ideally absorbs all incident radiation. To stay in thermal equilibrium with temperature T, the black body must radiate into the system. To simulate the blackbody radiation, we surround the grid with a series of noise sources next to the grid/ABL interface. These soft sources radiate EM waves into the grid having spectral properties consistent with blackbody radiation. The 1D grid is discretized with a spatial step Δx and time step Δt. As shown in the inset of Fig. 2.1, two point sources are placed at the extremities of the grid. Each source generates an electric field E_s at every time step t_j. Examples of the noise source of electric field $E_s(t_j)$ are shown in Fig. 2.1. A Fourier transform of the temporal correlation function of the electric field, $\langle E_s(t_1)E_s(t_2)\rangle$, gives the noise spectrum $D(\omega, T)$. If $E_s(t_j)$ is

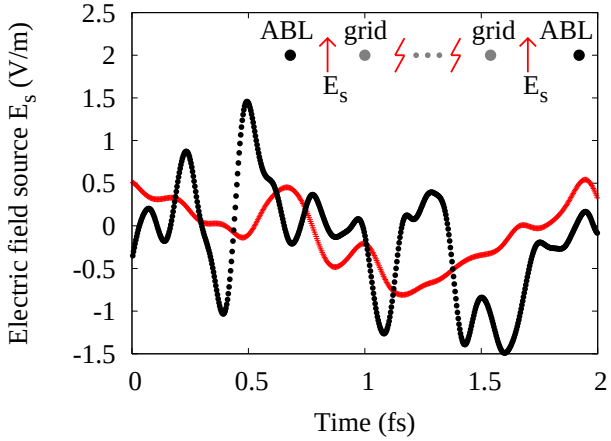

Figure 2.1. Thermal noise source electric field $E_s(t_j)$ generated for $T = 30,000$ K (red crosses) and $T = 50,000$ K (black dots). The noise correlation time $\tau_c \approx 0.337$ fs for $T = 30,000$ K and $\tau_c \approx 0.203$ fs for $T = 50,000$ K. $\Delta x = 1$ nm, $M = 2^{21}$ and $\tau_{sim} = 7$ ps. The inset is a schematic showing the noise sources placed next to the grid/ABL interface [**116**].

uncorrelated in time, i.e., $\langle E_s(t_1)E_s(t_2)\rangle \propto \delta(t_2 - t_1)$, $D(\omega, T)$ is the white-noise spectrum. This is incorrect as $D(\omega, T)$ should be equal to the energy density per unit frequency of blackbody radiation [**14**].

To find the energy density of blackbody radiation in 1D, we need to find the grand potential Λ of a Bose-Einstein ideal gas with an affinity of zero (due to the fact that photons are not a conserved particle species) [**88**]. Consider photons of frequency ω in a 1D space of length L. The density of states in 1D is $(L/\pi c)d\omega$ [**117**], where c is the speed of light in vacuum. The grand potential is expressed as

$$\Lambda = -\frac{L}{\pi c}\int \log[1 - \exp(-\beta\hbar\omega)]d\omega, \tag{2.1}$$

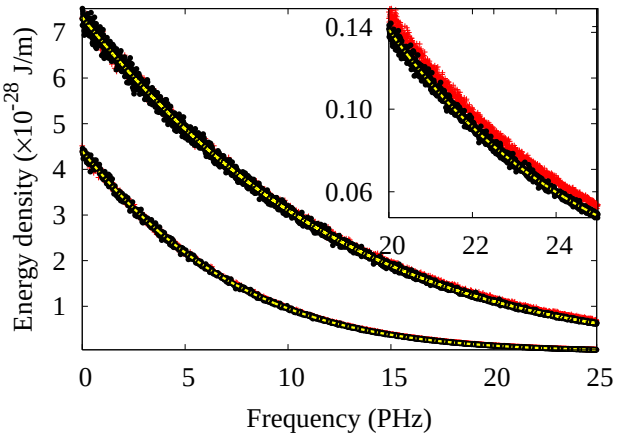

Figure 2.2. FDTD-calculated energy density of blackbody radiation propagating in 1D vacuum versus frequency ω for temperatures $T = 30,000$ K (lower) and $T = 50,000$ K (upper). The inset shows the energy density for temperature $T = 30,000$ K at higher frequencies. The data are obtained by averaging over 2000 calculations with the resolutions $\Delta x = 10$ nm (red crosses) and $\Delta x = 1$ nm (black dots). The source spectra $D(\omega, T)$ are also plotted as solid lines on top of the numerical spectra.

where $\beta = 1/k_B T$. The radiation energy can be found as $U_e = -\partial\Lambda/\partial\beta$ giving the energy density of radiation

$$\begin{aligned} \frac{U_e}{L} &= \frac{\hbar}{\pi c}\int \frac{\omega \exp(-\beta\hbar\omega)}{1-\exp(-\beta\hbar\omega)} d\omega \\ &= \frac{\hbar}{\pi c}\int \frac{\omega}{\exp(\beta\hbar\omega)-1} d\omega. \end{aligned} \tag{2.2}$$

Thus, the energy density of radiation *per unit frequency* is

$$D(\omega, T) = \frac{\hbar}{\pi c}\left[\frac{\omega}{\exp(\hbar\omega/k_B T)-1}\right]. \tag{2.3}$$

$D(\omega, T)$ for two different temperatures is plotted in Fig. 2.2. For computational convenience, we extend the range of ω from $(0, \infty)$ to $(-\infty, \infty)$. Since the electric field in

the FDTD simulation is a real number, $D(-\omega, T)$ must be equal to $D(\omega, T)$ for $\omega > 0$. Therefore, $D(\omega, T) = D(|\omega|, T)$. We normalize $D(\omega, T)$ as

$$D_n(|\omega|, T) = \frac{6\hbar^2}{\pi k_B^2 T^2} \left(\frac{|\omega|}{\exp(\hbar|\omega|/k_B T) - 1} \right) \tag{2.4}$$

so that $\int_{-\infty}^{\infty} D_n(|\omega|, T) d\omega = 2\pi$.

The temporal correlation function for the source electric field is given by

$$\langle E_s(t_1) E_s(t_2) \rangle = \frac{\delta^2}{2\pi} \int_{-\infty}^{\infty} d\omega D_n(|\omega|, T) e^{i\omega(t_2 - t_1)}, \tag{2.5}$$

where δ is the rms amplitude of the noise field whose value is to be determined later. For the thermal noise, the field correlation function is given specifically by

$$\langle E_s(t_1) E_s(t_2) \rangle = \frac{3\delta^2}{\pi^2} \left[\zeta(2, 1 - i(t_2 - t_1) k_B T/\hbar) + \zeta(2, 1 + i(t_2 - t_1) k_B T/\hbar) \right], \tag{2.6}$$

where the ζ-function is given as

$$\zeta(s, a) = \sum_{j=0}^{\infty} (j + a)^{-s}. \tag{2.7}$$

The temporal correlation function of thermal radiation is plotted in Fig. 2.3.

We employ a quick and straightforward way of generating random numbers for $E_s(t_j)$ so that Eq. 2.5 is satisfied. Freilikher *et al.* have developed such a method in the context of creating random surfaces with specific height correlations [**118**]. The end result takes advantage of the fast Fourier transform (FFT) which we use to generate the source electric

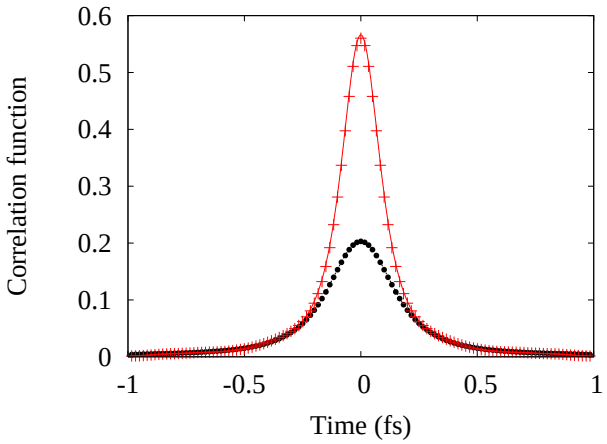

Figure 2.3. Temporal correlation function, $\langle E_s(t_1)E_s(t_2)\rangle$ vs. $t_2 - t_1$, for the noise electric field at $T = 30,000$ K (black circles) and $T = 50,000$ K (red crosses). The noise correlation times are $\tau_c \approx 0.337$ fs for $T = 30,000$ K and $\tau_c \approx 0.203$ fs for $T = 50,000$ K. $\Delta x = 1$ nm, $M = 2^{21}$, and $\tau_{sim} = 7$ ps. The lines represent $\langle E_s(t_1)E_s(t_2)\rangle$ given by the analytical expression in Eq. 2.6 for $T = 30,000$ K (black) and $T = 50,000$ K (red). Every 5th data point is taken from the numerical data in order to better show the agreement with the analytical solution.

field:

$$E_s(t_j) = \frac{\delta}{\sqrt{\tau_{sim}}} \sum_{l=-M}^{M-1} (M_l + iN_l) D_n^{1/2}(|\omega_l|, T) e^{i\omega_l t_j}, \tag{2.8}$$

where $2M$ is the total number of time steps, $\tau_{sim} = 2M\Delta t$ is the total simulation time and $\omega_l = 2\pi l/\tau_{sim}$. M_l and N_l are independent Gaussian random numbers with zero mean and a variance of one. Their symmetry properties are $M_l = M_{-l}$ and $N_l = -N_{-l}$. These Gaussian random numbers can be generated by the Marsaglia and Bray modification of the Box-Müller Transformation [**119**], a very fast and reliable method assuming the uniformly distributed random number generator is quick and robust.

The electric field sources generate both electric and magnetic fields, which propagate into the grid. $E_z(x, \omega)$ and $H_y(x, \omega)$ are obtained by the discrete Fourier transform (DFT)

of $E_z(x,t)$ and $H_y(x,t)$. Since both $E_z(x,t)$ and $H_y(x,t)$ are real numbers, $E_z(x,\omega) = E_z(x,-\omega)$ and $H_y(x,\omega) = H_y(x,-\omega)$. The EM energy density at frequency ω shall include $E_z(x,\omega)$, $E_z(x,-\omega)$, $H_y(x,\omega)$ and $H_y(x,-\omega)$. If the grid is vacuum, the steady-state energy density at every position x should be equal to the blackbody radiation density. The rms amplitude δ of the source field E_s is determined by

$$\frac{1}{2}\epsilon_0|E_z(x,|\omega|)|^2 + \frac{1}{2}\mu_0|H_y(x,|\omega|)|^2 = \frac{\hbar}{\pi c}\frac{|\omega|}{e^{\hbar|\omega|/k_BT}-1}. \tag{2.9}$$

When setting the parameters in the FDTD simulation, we must taken into consideration the characteristics of thermal noise. The temporal correlation time or coherence time τ_c of thermal noise is defined as the full width at half maximum (FWHM) of the temporal field correlation function. If the time step Δt is close to τ_c, E_s exhibits a sudden jump at each time step. The 1D FDTD algorithm cannot accurately propagate such step-like pulses (with sharp rising edge) if the Courant factor $S \equiv c\Delta t/\Delta x$ is set at a typical value $S < 1$. The pulse shape is distorted with fringes corresponding to both retarded propagation and superluminal response [**96**]. This occurs because the higher frequencies from the step discontinuity are being inadequately sampled and because of numerical dispersion arising from the method of obtaining the spatial derivatives for E and H. To avoid such problems, we use $S = 1$ which eliminates the numerical dispersion artifact [**96**]. Furthermore, we set $\Delta t \ll \tau_c$ which provides a dense temporal sampling relative to the correlation/coherence time of the thermal noise.

To obtain an accurate noise spectrum with the DFT, both the frequency and temporal resolutions must be chosen carefully. The two problems affecting the reliability of the DFT are aliasing and leakage due to the use of a finite simulation time [**106**]. The solution to

these problems is to increase the number of time steps $2M$ and decrease the time step value Δt. This takes the DFT closer to a perfect analytical Fourier transform, but run-time and memory limitations must be considered as well. Taking advantage of the FFT algorithm significantly reduces both noise generation time and spectral analysis time.

Although the thermal noise spectrum can be very broad, only noise within a certain frequency range is relevant to a specific problem. Let ω_{min} and ω_{max} denote the lower and upper limits of the frequency range of interest, and $\Delta\omega$ the frequency resolution needed within this range. To guarantee the accuracy of the noise simulation in $\omega_{min} < \omega < \omega_{max}$, the total running time τ_{sim} must exceed $2\pi/\omega_{min}$ and $2\pi/\Delta\omega$. The time step Δt has an additional requirement, $\Delta t < \pi/\omega_{max}$.

2.2. Thermal Noise in Vacuum

We first test the noise sources in a 1D FDTD system composed entirely of vacuum. Two sets of independent noise signals $E_s(t_j)$ are generated via Eq. 2.8. One set is added as a soft source one grid cell away from the left absorbing boundary; the other one cell from the right absorbing boundary. Both have equal rms amplitude δ so that the average EM flux to the left equals that to the right at any position x in the grid. Since the system is one dimensional, the EM flux at any distance away from the source has the same magnitude. The value of δ shall be adjusted so that Eq. 2.9 is satisfied. For the EM energy density radiated by one source to equal $D(|\omega|, T)$, we set δ to

$$\delta = \sqrt{\frac{2}{\epsilon_0}\frac{1}{6\hbar c}}k_B T. \tag{2.10}$$

After the noise fields in the grid reach steady state, the noise spectrum at any grid point is obtained by a DFT. We verify that the spectrum of EM energy density at any point in the grid is identical to that at the source. This means there is no distortion of the noise spectrum by the propagation of noise fields in vacuum. The two point sources at the grid/ABL interface radiate into both the grid and ABL. Since the two sources are uncorrelated with each other, their energy densities, instead of their field amplitudes, add in the grid. Thus no further modification of δ from that given by Eq. 2.10 is needed to satisfy Eq. 2.9. It is numerically confirmed that δ does not depend on the total length of the system.

Examples of the noise source of electric field $E_s(t_j)$ at $T = 30,000$ K and $T = 50,000$ K are shown in Fig. 2.1. $\Delta x = 1$ nm, and $\Delta t \ll \tau_c$. The frequency range of interest is set as $\omega_{min} = 2 \times 10^{15}$ Hz, $\omega_{max} = 2.5 \times 10^{16}$ Hz, and the frequency resolution $\Delta\omega = 1 \times 10^{12}$ Hz. From the condition $\Delta t < \pi/\omega_{max}$, Δx shall be less than 37 nm. Figure 2.2 compares the FDTD calculated energy density to that of thermal radiation density $D(\omega, T)$. Using $\Delta x = 10$ nm creates a slight discrepancy at high frequencies; e. g. at $\omega \leq 1 \times 10^{16}$ Hz the mean error $\gtrsim 2.5\%$. To reduce the error to below 2.5% at $\omega_{max} = 2.5 \times 10^{16}$ Hz, we refine the resolution. Using $\Delta x = 4$ nm changes the error at ω_{max} to 1.6%. If the total time step $2M = 2^{21}$ is fixed, the decrease of Δt leads to a reduction of $\tau_{sim} = 2M\Delta t$, which increases $2\pi/\tau_{sim}$ to 2×10^{11} Hz. We must check that $2\pi/\tau_{sim} < \omega_{min}$ and $2\pi/\tau_{sim} < \Delta\omega$ are still satisfied. With $\Delta x = 1$ nm, the error at 2.5×10^{16} Hz is further reduced to $< 0.1\%$. $2\pi/\tau_{sim}$ increases to 9×10^{11} Hz, which is still below the set values of ω_{min} and $\Delta\omega$. Therefore, using the value of δ in Eq. 2.10 and carefully choosing the numerical

resolutions yield the blackbody spectrum at every point in the grid within the frequency range of interest.

Figure 2.3 compares the FDTD calculated temporal correlation function of the electric field to that of Eq. 2.6 at $T = 30,000$ K and $50,000$ K. With increasing temperature, the coherence time τ_c reduces quickly. The quantitative dependence of τ_c on T is found to be $\tau_c \approx 1.32\hbar/k_B T$. This $1/T$ dependence does not change for a dimensionality higher than one; only the prefactor changes [**120**]. As the correlation time τ_c decreases, the time step Δt shall be reduced to maintain the temporal resolution of the correlation function. The subsequent reduction of total running time $\tau_{sim} = 2M\Delta t$ does not affect the numerical accuracy, as long as the total number of time steps $2M$ is fixed. A decrease of $2M$ would result in an increased mean-square error in the correlation function due to less sampling. As shown in Fig. 2.3, the good agreement of the FDTD calculated temporal correlation function to that of blackbody radiation given by Eq. 2.3 confirms that introducing noise sources with the characteristics of blackbody radiation at the FDTD absorbing boundary effectively simulates thermal noise in vacuum.

2.3. Thermal Noise in an Open Cavity

Next we calculate the thermal noise in a dielectric slab of length L and refractive index $n > 1$. This slab constitutes an open cavity in that the electromagnetic field leaks from both surfaces of the slab into the exterior region. A schematic of the 1D open cavity is shown in the inset of Fig. 2.4(b). The cavity mode frequency is $\omega_m = m\pi c/nL$, where m is an integer. The frequency spacing of adjacent modes is $d\omega = \omega_m - \omega_{m-1} = \pi c/nL$, which is independent of m. Ignoring intracavity absorption, the decay of cavity photons

is caused only by their escape from the cavity. All the cavity modes have the same decay time $\tau = 1/k_i c$, where from Eq. 1.53 $k_i = -\ln(r^2)/2nL$, and $r = (1-n)/(1+n)$ is the reflection coefficient at the boundary of the dielectric slab. The mode linewidth is $\delta\omega = 2/\tau$. We simulate only good cavities whose modes are well separated in frequency, namely, $\delta\omega < d\omega$. Since $\delta\omega \propto 1/L$, the ratio $\delta\omega/d\omega$ is independent of L, and is only a function of n.

The Langevin equation for the annihilation operator $\hat{a}_m(t)$ of photons in the m-th cavity mode (see Eq. 1.18) is

$$\frac{d\hat{a}_m(t)}{dt} = \left(-i\omega_m - \frac{1}{\tau}\right)\hat{a}_m(t) + \hat{\Gamma}_m(t), \tag{2.11}$$

where $\hat{\Gamma}_m(t)$ is the Langevin force. If the noise correlation time $\tau_c \ll \tau$, $\hat{\Gamma}_m(t)$ can be considered δ-correlated in time. The Markovian approximation gives $\left\langle \hat{\Gamma}_m^\dagger(t)\hat{\Gamma}_m(t')\right\rangle = D_F\delta(t-t')$. According to the fluctuation-dissipation theorem, $D_F = (1/\tau)n_T(\omega_m)$, where

$$n_T(\omega_m) = \frac{1}{\exp(\hbar\omega_m/k_BT) - 1} \tag{2.12}$$

is the number of thermal photons in a vacuum mode of frequency ω_m at temperature T [**90**].

From Eq. 2.11, the average photon number in one cavity mode $\langle\hat{n}_m(t)\rangle \equiv \left\langle\hat{a}_m^\dagger(t)\hat{a}_m(t)\right\rangle$ satisfies

$$\frac{d}{dt}\langle\hat{n}_m(t)\rangle = -\frac{2}{\tau}\langle\hat{n}_m(t)\rangle + \frac{2}{\tau}n_T(\omega_m). \tag{2.13}$$

At steady state, $\langle \hat{n}_m \rangle = n_T(\omega_m)$ in each cavity mode. The number of thermal photons is determined by the Bose-Einstein distribution $n_T(\omega_m)$. $\langle \hat{n}_m \rangle$ is independent of the cavity mode decay rate because the amount of thermal fluctuation entering the cavity increases by the same amount as the intracavity energy decay rate.

2.3.1. Markovian Regime

In our FDTD simulations, we verify that when $\tau \gg \tau_c$ the number of thermal photons in one cavity mode is equal to $n_T(\omega_m)$. Since there is neither a driving field (e.g., a pumping field) nor excited atoms in the cavity, the EM energy stored in one cavity mode comes entirely from the thermal radiation of the ABL which is coupled into that particular mode. The steady-state number of photons in the m-th cavity mode is obtained from the FDTD calculation of intracavity EM energy within the frequency range $\omega_{m-1/2} < \omega < \omega_{m+1/2}$, where $\omega_{m\pm1/2} = (m \pm 1/2)\pi c/nL$.

$$n_m \equiv \langle \hat{n}_m \rangle = \frac{1}{\hbar\omega_m} \int_{\omega_{m-1/2}}^{\omega_{m+1/2}} d\omega \int_0^L dx \left(\frac{1}{2}\epsilon |E_z(x,\omega)|^2 + \frac{1}{2}\mu_0 |H_y(x,\omega)|^2 \right) \tag{2.14}$$

In our simulation, the temperature of the thermal sources at the ABL is $T = 30,000$ K. The coherence time of thermal radiation is $\tau_c = 0.337$ fs. The refractive index of the dielectric slab is $n = 6$, and the length is $L = 2400$ nm. The cavity lifetime $\tau = 143$ fs, is much longer than τ_c. The reason to choose a relatively large value of n is to have $\delta\omega < d\omega$ so that the cavity modes are separated in frequency. Care must be taken in setting the grid resolution because the intracavity wavelength is reduced to λ/n. To maintain the spatial resolution, Δx is decreased to meet $\Delta x \ll \lambda/n$. In our FDTD simulation, $\Delta x = 1$ nm and $2M = 2^{21}$. After the intracavity EM field reaches the steady state, we calculate

the average thermal energy density inside the cavity

$$U(\omega) = \frac{1}{L}\int_0^L dx \left(\frac{1}{2}\epsilon|E_z(x,\omega)|^2 + \frac{1}{2}\mu_0|H_y(x,\omega)|^2\right). \tag{2.15}$$

Figure 2.4(a) shows the intracavity noise spectrum $U(\omega)$, which features peaks at the cavity resonant frequencies ω_m. Because $n > 1$, EM energy is also stored in the dielectric slab at frequencies away from cavity resonances. For example, $U(\omega = \omega_{m\pm1/2})$ is higher than that in vacuum by a factor of $2n^2/(n^2+1)$. Thus the entire noise spectrum lies on top of the vacuum blackbody radiation spectrum, as confirmed in Fig. 2.4. The number of thermal photons in a cavity mode is calculated via Eq. 2.14 and plotted in Fig. 2.5. The modal photon number n_m is equal to $n_T(\omega_m)$ with a mean error less than 0.1%. This result agrees with the steady-state solution of Eq. 2.14. It confirms that our numerical model of thermal noise in an open cavity is consistent with the prediction of quantum mechanical theory. Note that the modal photon numbers in Fig. 2.5 are time averaged values. Their values being much less than unity can be interpreted in a quantum mechanical picture as that most of the time there is no photon in the cavity mode.

2.3.2. Non-Markovian Regime

The above calculation is done in the Markovian regime. Next we move to the non-Markovian regime by reducing τ. The refractive index is kept at $n = 6$, while the cavity length L is reduced. This is a simple way of increasing the mode linewidth $\delta\omega$ while keeping the modes separated in frequency, i.e., keeping $\delta\omega/d\omega$ constant. If τ is decreased to less than τ_c, Δt shall be reduced to keep $\Delta t \ll \tau$. Meanwhile, the increase of the mode linewidth and mode spacing allows low frequency resolution, namely, an increase of $\Delta\omega$.

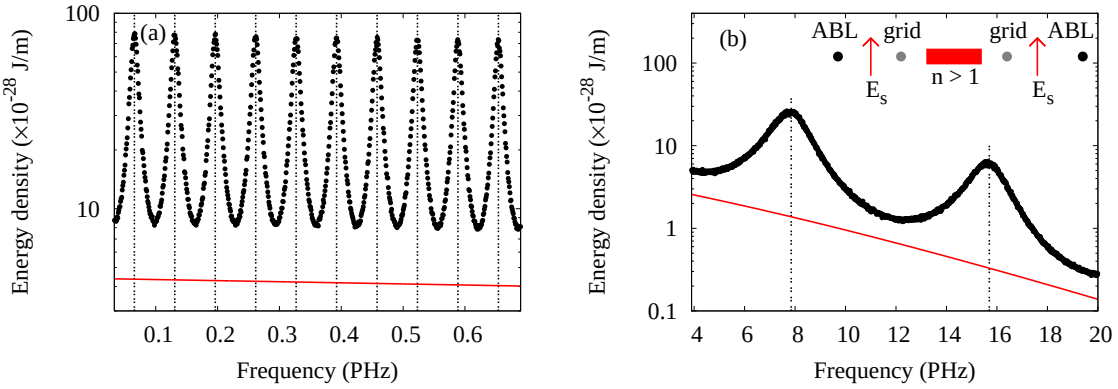

Figure 2.4. Spatially-averaged EM energy density $U(\omega)$, calculated by the FDTD method, versus frequency ω in a dielectric slab cavity with refractive index $n = 6$ and length $L = 2400$ nm (a) and $L = 20$ nm (b). The vertical black dashed lines mark the frequencies of cavity modes ω_m. The spectrum of impinging blackbody radiation $D(\omega, T)$ is also plotted (red solid line). In (a) the cavity decay time $\tau = 143$ ps, much longer than τ_c. In (b), $\tau = 1.19$ fs, comparable to τ_c.

For example, at $L = 20$ nm, we set $\Delta x = 0.1$ nm, $\Delta\omega = 9 \times 10^{12}$ Hz and $2M = 2^{21}$. Figure 2.4(b) shows the intracavity noise spectrum $U(\omega)$ in this regime, which also features peaks at the cavity resonant frequency ω_m. Figure 2.5 shows the FDTD-calculated value of n_m as L decreases gradually from 2400 nm to 20 nm. When τ approaches τ_c, n_m is no longer independent of τ, but starts increasing from $n_T(\omega_m)$. This means the number of thermal photons that are captured by a cavity mode increases with the decrease of τ. As the coherence time of thermal radiation impinging onto the cavity approaches the cavity photon lifetime, the constructive interference of the thermal field is improved inside the cavity, leading to a larger buildup of intracavity energy.

We also investigate a different situation where τ is fixed and τ_c is varied. By reducing the temperature T, the coherence time of thermal radiation τ_c is increased. Meanwhile, the energy density of thermal radiation is decreased. As shown in Fig. 2.6, the number of

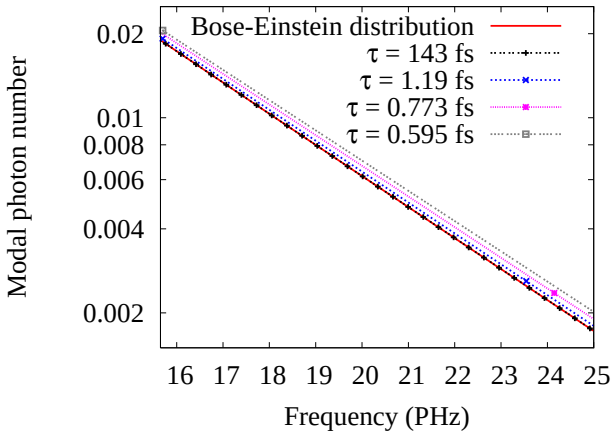

Figure 2.5. The number of thermal photons in individual cavity modes n_m, calculated via the FDTD method, for a slab cavity with $n = 6$. The cavity length L is varied to change τ. The impinging blackbody radiation has $T = 30,000$ K and $\tau_c = 0.337$ fs. The values of τ_c/τ are 0.0024, 0.29, 0.43, and 0.56. Lines are drawn to connect the data points at the mode frequencies $\omega_m = \pi cm/nL$ to illustrate its frequency dependence. For $\tau_c \ll \tau$ (only every 5th mode for $\tau = 143$ fs is shown to improve the visibility), the photon number n_m coincides with the Bose-Einstein distribution n_T. When $\tau_c \sim \tau$, n_m deviates from n_T.

thermal photons n_m in a cavity mode is reduced. This can be easily understood as there are fewer thermal photons incident onto the cavity at lower T. Nevertheless, n_m is larger than $n_T(\omega_m)$ at the same T. This is because the longer coherence time of the thermal field results in better constructive interference inside the cavity.

2.4. Analytical Examination and Discussion

To gain a better understanding of our FDTD simulation results in the non-Markovian regime, we analytically examine the effect of noise correlation time τ_c on the amount of thermal noise inside an open cavity.

The transfer matrix formalism is used to examine energy buildup in a slab with index of refraction n and length L. The specific boundary conditions of an incoming or outgoing

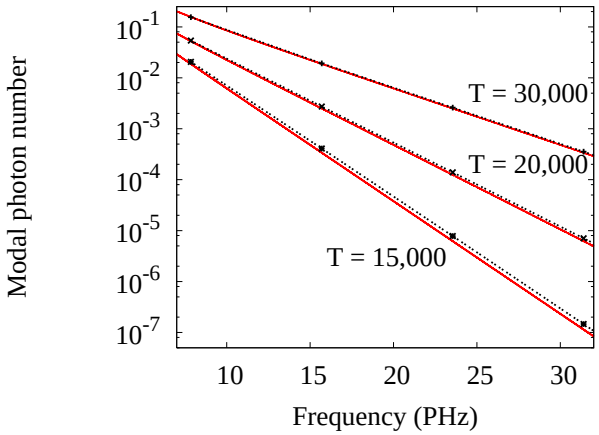

Figure 2.6. The number of thermal photons in individual cavity modes n_m, calculated via the FDTD method, for a dielectric slab cavity with $n = 6$ and $L = 20$ nm. The cavity decay time $\tau = 1.19$ fs. The temperature of blackbody radiation is varied to change τ_c. The values of τ_c/τ are 0.29 ($T = 30,000$ K), 0.43 ($T = 20,000$ K), and 0.56 ($T = 15,000$ K). Black dashed lines are drawn to connect the data points at the mode frequencies $\omega_m = \pi cm/nL$ to illustrate its frequency dependence. For comparison, the Bose-Einstein distribution $n_T(\omega)$ is also plotted (red solid lines) for the same temperatures.

wave will not be considered because off-resonant frequencies will be examined as well. First, the electric field inside the cavity must be calculated. This is done by operating Eqs. 1.42 and 1.43 on an input wave vector

$$b_1(x)c_0 \begin{pmatrix} 1 \\ r \end{pmatrix} = \frac{1}{t_b} \begin{pmatrix} e^{i\tilde{k}_m nx} + rr_b e^{i\tilde{k}_m nx} \\ r_b e^{i\tilde{k}_m nx} + re^{i\tilde{k}_m nx} \end{pmatrix}. \tag{2.16}$$

Using $\tilde{k}_m = \pi m/nL$, the reflectivity r can be calculated via Eq. 1.44 as

$$r = \frac{-M_{21}}{M_{22}} = \frac{-(r_b e^{-i\pi m} + r_a e^{i\pi m})}{r_b r_a e^{i\pi m} + e^{-i\pi m}} \tag{2.17}$$

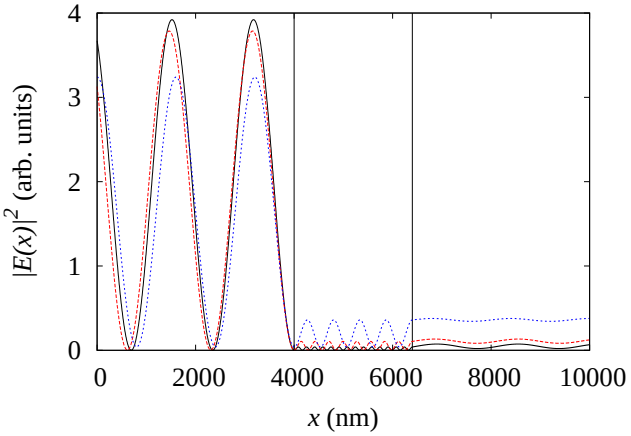

Figure 2.7. Intensity distributions of off-resonant modes for $n = 3$ and $m = 4.5$ (blue), $n = 6$ and $m = 8.5$ (red), $n = 10$ and $m = 14.5$ (black) in a dielectric slab of length $L = 2400$ nm. Larger n values give a higher reflected field amplitude and a smaller amplitude inside the cavity. Nonetheless, the energy of off-resonant modes increases as n increases. Vertical lines mark the cavity boundaries.

Now, from Eq. 2.16, the electric field is given as

$$E_z(x) = \frac{1}{t_b}(1 + rr_b)e^{i\pi mx/L} + \frac{1}{t_b}(r_b + r)e^{-i\pi mx/L}. \tag{2.18}$$

$|E_z(x)|^2$ is plotted in Fig. 2.7 for a slab of length $L = 2.4$ μm for various m and n values. Intensity distributions for off-resonant frequencies ($m = j/2$ where j is any positive integer) are shown for $n = 3$ ($\lambda = 3199$ nm), $n = 6$ ($\lambda = 3387$ nm), and $n = 10$ ($\lambda = 3309$ nm). We see what we would expect, a decrease in amplitude inside the cavity and a higher reflected amplitude for larger n. The on-resonance intensity distributions were observed with maximum amplitudes of one both inside and outside the cavity. Both cases agree almost perfectly with FDTD calculations.

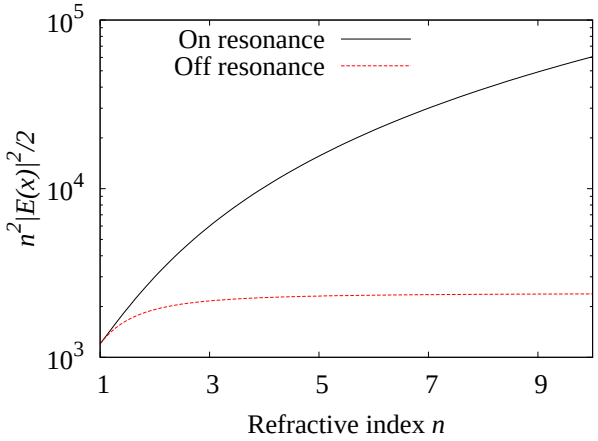

Figure 2.8. Energy inside of a dielectric slab as a function of index of refraction. Energy at on resonance frequencies (black) equal energy at off resonance frequencies (red) for $n = 1$. But even energy at off resonance frequencies will build up inside the slab.

The intracavity energy as a function of index can now be calculated from Eq. 2.18

$$W(n) = \frac{1}{2}n^2 \int_0^L |E_z(x,n)|^2 dx. \tag{2.19}$$

This results in

$$W(n) = \frac{n^2 L[2m(1+n^2)\pi + (n^2-1)\sin(2m\pi)]}{m\pi[1+6n^2+n^4-(n^2-1)^2\cos(2m\pi)]}. \tag{2.20}$$

When m is a positive integer (on resonance), the energy scales as $W(n) = L(n^2+1)/4$ while it scales as $W(n) = n^2L/(n^2+1)$ when off resonance. Plots for both of these cases are shown in Fig. 2.8. At $n = 1$, of course, the two different cases agree.

The *energy* inside a cavity at an off resonant frequency for large n would increase from the $n = 1$ case. It is noted, however, that the field amplitude itself decreases as a function of n. In other words, $\frac{1}{2}\int_0^L |E_z(x,n)|^2 dx = L/(n^2+1)$, when off resonance.

With FDTD, the ratio of the intracavity EM energy at frequency ω to the energy density of the thermal source outside the cavity is

$$W(\omega) \equiv \frac{\int_0^L dx \left[\frac{1}{2}\epsilon|E_z(x,\omega)|^2 + \frac{1}{2}\mu_0|H_y(x,\omega)|^2\right]}{D(\omega,T)}. \tag{2.21}$$

This is obtained analytically from the transfer matrix method by rewriting Eq. 2.20

$$W(\omega) = \frac{2nc}{\omega}\left[\frac{2\omega nL(1+n^2)/c + (n^2-1)\sin(2\omega nL/c)}{1+6n^2+n^4-(n^2-1)^2\cos(2\omega nL/c)}\right]. \tag{2.22}$$

It can be used to calculate the ratio $B_m(\tau_c,\tau) \equiv n_m/n_T(\omega_m)$, as

$$n_m = \left[\int_{\omega_{m-1/2}}^{\omega_{m+1/2}} d\omega\, W(\omega) D(\omega,T)\right]/\hbar\omega_m. \tag{2.23}$$

In the Markovian regime $\tau_c \ll \tau$ and $D(\omega,T)$ is nearly constant over the frequency interval of one cavity mode so

$$\begin{aligned} B_m(\tau_c,\tau) &= \frac{D(\omega_m,T)}{\hbar\omega_m n_T(\omega_m)} \int_{\omega_{m-1/2}}^{\omega_{m+1/2}} d\omega\, W(\omega) \\ &= \frac{1}{\pi c}\int_{\omega_{m-1/2}}^{\omega_{m+1/2}} d\omega\, W(\omega). \end{aligned} \tag{2.24}$$

We input the same parameters as the FDTD simulation: $n = 6$, $L = 2400$ nm, and $\tau = 143$ fs. As τ_c approaches zero, the integration of $W(\omega)$ from $\omega_{m-1/2}$ to $\omega_{m+1/2}$ gives a value close to πc. Thus, as shown in the inset of Fig. 2.9, $B_m(\tau_c,\tau) \approx 1$ for $\tau_c/\tau \ll 1$. The deviation of $B_m(\tau_c,\tau)$ from one is greater for smaller m. One possible reason is that the condition $\delta\omega \ll \omega_m$ no longer holds for small m and there is a large uncertainty in defining

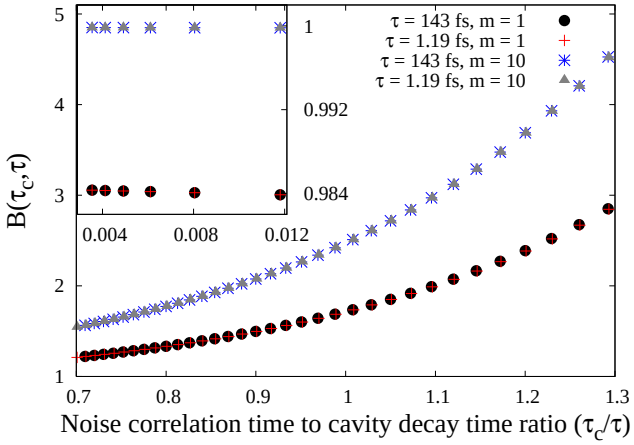

Figure 2.9. $B_m(\tau_c, \tau) \equiv n_m/n_T(\omega_m)$ vs. the ratio of noise correlation time to cavity decay time τ_c/τ. $B_m(\tau_c, \tau)$ depends only on the ratio τ_c/τ and not on τ_c nor τ individually. This plot was generated by fixing τ and varying τ_c. Cavity modes of higher m have a larger value of $B_m(\tau_c, \tau)$ whether in the regime $\tau_c \sim \tau$ (main panel) or $\tau_c \ll \tau$ (inset).

the frequency of a cavity mode whose linewidth is comparable to its center frequency. In other words, the calculation of n_m using Eq. 2.23 becomes questionable.

In the non-Markovian regime $\tau_c \gtrsim \tau$, $D(\omega, T)$ is not constant over the frequency range of a cavity mode anymore, thus it cannot be taken out of the integral in Eq. 2.23. The behavior of $B_m(\tau_c, \tau)$ in this regime is shown in the main panel of Fig. 2.9. As τ_c approaches τ, $B_m(\tau_c, \tau)$ no longer stays near one but increases with τ_c/τ. This result is consistent with that of the FDTD simulation presented in the previous section. On the one hand, if τ is fixed and τ_c is increased by decreasing the temperature T, the absolute number of thermal photons in a cavity mode n_m decreases, but its ratio to the number of thermal photons in a vacuum mode $n_T(\omega_m)$ increases. On the other hand, if τ_c is fixed and τ is decreased by shortening the cavity length L, both n_m and $n_m/n_T(\omega_m)$ increase. The departure of n_m from $n_T(\omega_m)$ is a direct consequence of the breakdown of the Markovian

approximation. When the coherence time of thermal radiation is comparable to the cavity decay time, the Langevin force $\hat{\Gamma}_m(t)$ in Eq. 2.11 is no longer δ-correlated in time, and Eq. 2.13 is invalid.

CHAPTER 3

Atomic State Population and Polarization Fluctuations

As discussed earlier, FDTD has been extensively used in solving Maxwell's equations for dynamic electromagnetic (EM) fields. Although the FDTD method has become a powerful tool in computational electrodynamics, it has been applied mostly to classical or semiclassical problems without noise. We have learned, however, that noise plays an important role in light-matter interaction.

Our goal is to develop a FDTD-based numerical method to simulate fluctuations in macroscopic systems caused by interactions of atoms and photons with reservoirs (see Fig. 1.1). Such interactions induce temporal decay of photon number, atomic polarization and excited state's population, which can be described phenomenologically by decay constants. The fluctuation-dissipation theorem demands temporal fluctuations or noise to accompany these decays. In Ch. 2, we included noise caused by the interaction of the light field with external reservoir in an open system. In this chapter, we develop a numerical model to simulate noise caused by the interaction of atoms with reservoirs such as lattice vibrations and atomic collisions. As an example, we apply the method to a numerical simulation of superfluorescence in a macroscopic system where the dominant noise is from the atoms rather than the light field. We then study the effects of noise on lasing in a dielectric slab.

3.1. Noise Model

Modeling quantum behavior computationally can be challenging considering quantum operators do not commute. However, some progress can be made by fixing the operator ordering and uniquely mapping the operators to c-number functions. One example is the Wigner function [**121**]. Wigner developed a probability distribution for the simultaneous values of position and momentum, with the admitted shortcoming that the distribution is not positive everywhere. Thus, it cannot be interpreted as a true probability distribution. It is indeed a challenge to find a simple expression for the probability of a configuration precisely because the probability of momentum and position may not be given simultaneously. Glauber and Sudarshan developed the P representation which uses coherent states as a basis set for the density matrix [**122, 123**]. Making use of the coherent states does not require the explicit introduction of coordinate or momentum variables [**124**]. Similar to the Wigner function, operators are replaced with c-numbers and fairly accurate results are obtained when behavior is nearly classical. Results diverge, however, when behavior becomes nonclassical.

Drummond and Gardiner introduced the positive P representation which allowed P to be interpreted as a genuine probability density even when considering nonclassical behavior [**125**]. This allows any state of light to be expressed using the coherent states as a basis set. Using this and representing the operator evolution using Fokker-Planck equations, Drummond and Raymer were able to obtain c-number equations without ambiguity [**126**]. Starting from the quantum Langevin equation within the Markovian approximation, they derived a set of stochastic c-number differential equations describing light propagation and atom-light interaction in the many-atom limit. The noise sources in these equations

are from both the damping and the nonlinearity in the Hamiltonian. The latter represents the nonclassical component of noise, giving rise to nonclassical statistical behavior. Since our primary interests lie with classical behavior of macroscopic systems, such as lasing, we neglect the nonclassical noise in this thesis.

The amplitude of classical noise accompanying the field decay (as discussed in Ch. 2) is proportional to $\sqrt{n_T}$, where n_T is the thermal photon number. At room temperature the number of thermal photons at visible frequencies ($\hbar\omega \sim 1$ eV) is on the order of 10^{-17}. This can be interpreted in a quantum mechanical picture as that most of the time there are no thermal photons at visible frequencies in the system. Thus, the noise related to field decay is neglected in this chapter. At higher temperatures or longer wavelengths, this noise becomes significant and it can be incorporated into the FDTD algorithm following the approach we developed in Ch. 2.

The classical noise related to the pumping and decay of the atomic density matrix can be expressed as

$$\begin{aligned} \Gamma_{12} &= (\xi_1 + i\xi_2)\sqrt{\gamma_p \rho_{22}} \\ \Gamma_{21} &= (\xi_1 - i\xi_2)\sqrt{\gamma_p \rho_{22}} \\ \Gamma_{22} &= \xi_3 \sqrt{\rho_{22}/T_1 + P_r \rho_{11}/T_1}. \end{aligned} \tag{3.1}$$

These noise terms are associated with ρ_{12}, ρ_{21}, and ρ_{22} respectively. $\gamma_p = 1/T_2 - 1/2T_1$ is the pure dephasing rate in which atomic populations are conserved [**127**]. The ξ_j terms are real, Gaussian, random variables with zero mean and the following correlation relation

$$\langle \xi_j(t)\xi_k(t')\rangle = \delta_{jk}\delta(t-t'), \tag{3.2}$$

where $j, k = 1, 2, 3$. The noise terms Γ_{12} and Γ_{21} represent fluctuations corresponding to decoherence by dephasing, while Γ_{22} is the fluctuation corresponding to relaxation of and pumping to the excited state's population. Only the linear term for pump noise is included here, a common first order approximation [**90**]. Furthermore, because we assume $T_2 \ll T_1$, pump fluctuations are neglected in Γ_{12} and Γ_{21} since they are orders of magnitude smaller than noise due to dephasing. According to Eq. 1.30, the noise terms for the Bloch vector are reduced to real variables as

$$\begin{aligned} \Gamma_1 &= 2\xi_1\sqrt{\gamma_p \rho_{22}} \\ \Gamma_2 &= -2\xi_2\sqrt{\gamma_p \rho_{22}} \\ \Gamma_3 &= 2\xi_3\sqrt{\rho_{22}/T_1 + P_r\rho_{11}/T_1}. \end{aligned} \tag{3.3}$$

They can be added directly to Eq. 1.35.

In a 1D system, the total number of atoms N are split equally among M grid cells, giving the number of atoms per cell $N_s = N/M$. All quantities are defined at each individual grid cell, e.g., the term $\rho_3(x)$ is the *number* of inverted atoms in one cell at position x. The number of atoms in each cell is assumed to be constant assuring $\dot{\rho}_{11} + \dot{\rho}_{22} = 0$. We forcibly keep N_s constant via the relation $\rho_{11} = N_s - \rho_{22}$ and only calculate the excited state's population $\rho_{22}(t)$. The final stochastic equations to be solved

are

$$
\begin{aligned}
\frac{d\rho_1(x,t)}{dt} &= \omega_a \rho_2(x,t) - \frac{1}{T_2}\rho_1(x,t) + \Gamma_1(x,t) \\
\frac{d\rho_2(x,t)}{dt} &= -\omega_a \rho_1(x,t) + \frac{2|\gamma|}{\hbar} E_z(x,t)\left[2\rho_{22}(x,t) - N_s\right] - \frac{1}{T_2}\rho_2(x,t) + \Gamma_2(x,t) \\
\frac{d\rho_{22}(x,t)}{dt} &= -\frac{|\gamma|}{\hbar} E_z(x,t)\rho_2(x,t) - \frac{1}{T_1}\rho_{22}(x,t) + \frac{P_r}{T_1}[N_s - \rho_{22}(x,t)] + \Gamma_{22}(x,t).
\end{aligned} \tag{3.4}
$$

In the above equation, the steady-state value of ρ_3 in Eq. 1.35 is substituted by $\rho_3^{(s)} = N_s(P_r - 1)/(P_r + 1)$, an expression obtained by setting the time derivatives in Eq. 1.35 to zero. ρ_{11} in the expression of Γ_{22} in Eq. 3.1 can be replaced by $N_s - \rho_{22}$.

As previously mentioned, we use a weakly coupled method that is easily implemented and efficient for 1D systems. The noise terms in Eq. 3.4 are present throughout the entirety of the simulation and thus, should be incorporated efficiently. After discretization, the ξ_i terms are correlated according to $\langle \xi_j(x_u, t_m)\xi_k(x_v, t_n)\rangle = (1/\Delta t)\delta_{jk}\delta_{uv}\delta_{mn}$, and can be generated quickly with the Marsaglia and Bray modification of the Box-Müller Transformation [**119**]. Because the noise terms contain $\sqrt{\rho_{22}}$, as seen in Eqs. 3.1 and 3.3, we are not able to use the weakly coupled scheme to solve for ρ_1, ρ_2 and ρ_{22} as precisely as possible. Instead, the approximation of using the previous time step value $\sqrt{\rho_{22}^{n-1/2}}$ is employed. It is valid as long as the atomic population is varying slowly. For the simulation of superfluorescence in Sec. 3.2, the *maximum* change of ρ_{22} over one time step Δt is only 0.0007%.

The discretized equations with noise at each grid point are

$$E_z^{n+1}=E_z^n+\frac{\Delta t}{\epsilon}\frac{dH_y}{dx}-\Delta tA\rho_1^{n+1/2}+\Delta tB\rho_2^{n+1/2} \tag{3.5a}$$

$$H_y^{n+1/2}=H_y^{n-1/2}-\frac{\Delta t}{\mu_0}\frac{dE_z}{dx} \tag{3.5b}$$

$$\rho_1^{n+1/2}=\rho_1^{n-1/2}+\frac{1}{2}\Delta t\omega_a\left(\rho_2^{n+1/2}+\rho_2^{n-1/2}\right)-\frac{1}{2}\frac{\Delta t}{T_2}\left(\rho_1^{n+1/2}+\rho_1^{n-1/2}\right)+\Delta t\Gamma_1 \tag{3.5c}$$

$$\rho_2^{n+1/2}=\rho_2^{n-1/2}-\frac{1}{2}\Delta t\omega_a\left(\rho_1^{n+1/2}+\rho_1^{n-1/2}\right)-\frac{1}{2}\frac{\Delta t}{T_2}\left(\rho_2^{n+1/2}+\rho_2^{n-1/2}\right)+\frac{2\Delta t|\gamma|}{\hbar}E_z^n\left(\rho_{22}^{n+1/2}+\rho_{22}^{n-1/2}-N_s\right)+\Delta t\Gamma_2 \tag{3.5d}$$

$$\rho_{22}^{n+1/2}=\rho_{22}^{n-1/2}-\frac{1}{2}\frac{\Delta t|\gamma|}{\hbar}E_z^n\left(\rho_2^{n+1/2}+\rho_2^{n-1/2}\right)-\frac{1}{2}\frac{\Delta t}{T_1}\left(1+P_r\right)\left(\rho_{22}^{n+1/2}+\rho_{22}^{n-1/2}\right)+\Delta tP_rN_s/T_1+\Delta t\Gamma_{22}, \tag{3.5e}$$

where we have defined

$$\begin{aligned} A &\equiv\frac{|\gamma|}{V_s\epsilon T_2} \\ B &\equiv\frac{|\gamma|\omega_a}{V_s\epsilon}. \end{aligned} \tag{3.6}$$

Equation 3.5 is solved to obtain the time-stepped equations for E_z, H_y, ρ_1, ρ_2, and ρ_{22}. This is easy to do if we put Eq. 3.5 in matrix form.

$$\left(\begin{array}{c|c|c|c} (1+\Delta t/2T_2) & -\Delta t\omega_a/2 & 0 & -F \\ \hline \Delta t\omega_a/2 & (1+\Delta t/2T_2) & (-2\Delta t\gamma/\hbar)E^n & -G \\ \hline 0 & (\Delta t\gamma/2\hbar)E^n & (1+\Delta t/2T_1+\Delta tP_r/2T_1) & -L \end{array}\right)\left(\begin{array}{c} \rho_1^{n+1/2} \\ \rho_2^{n+1/2} \\ \rho_{22}^{n+1/2} \\ 1 \end{array}\right)=0, \tag{3.7}$$

where we have defined

$$
\begin{aligned}
F \equiv & (1-\Delta t/2T_2)\rho_1^{n-1/2} + (\Delta t\omega_a/2)\rho_2^{n-1/2} + \Delta t\Gamma_1 \\
G \equiv & (1-\Delta t/2T_2)\rho_2^{n-1/2} - (\Delta t\omega_a/2)\rho_1^{n-1/2} + (2\Delta t\gamma/\hbar)E^n\rho_{22}^{n-1/2} \\
& - (2\Delta t N_s\gamma/\hbar)E^n + \Delta t\Gamma_2 \\
L \equiv & (1-\Delta t/2T_1 - \Delta t P_r/2T_1)\rho_{22}^{n-1/2} - (\Delta t\gamma/2\hbar)E^n\rho_2^{n-1/2} + \Delta t P_r N_s/T_1 + \Delta t\Gamma_{22}.
\end{aligned} \tag{3.8}
$$

Taking the reduced row-echelon form of the matrix on the left side in Eq. 3.7 gives the final solutions for E_z^n, $H_y^{n+1/2}$, $\rho_1^{n+1/2}$, $\rho_2^{n+1/2}$, and $\rho_{22}^{n+1/2}$.

These equations without noise ($\Gamma_i = 0$) and no pumping rate ($P_r = 0$) are verified by reproducing self-induced transparency (SIT) effects [**99**]. Figure 3.1 shows how the normalized population inversion ρ_3 is changed by adjusting the amplitude of an incoming electric field pulse. The π pulse completely excites the two-level atom medium as it travels through the system. The entire system is initially in the ground state ($\rho_3 = -1$). After the pulse has passed through the entire system, the entire system is in the excited state ($\rho_3 = +1$). Examining one grid cell in time would reveal the Bloch vector $\vec{\rho}$ flipping completely from $\vec{\rho} = -1\hat{e}_3$, to $\vec{\rho} = 1\hat{e}_3$. The 2π pulse locally excites the two-level atom medium as it travels through the system. Where the electric field amplitude is largest, the population inversion is completely excited ($\rho_3 = 1$). Examining one grid cell in time would reveal the Bloch vector $\vec{\rho}$ flipping completely from $\vec{\rho} = -1\hat{e}_3$, to $\vec{\rho} = 1\hat{e}_3$, then back again to $\vec{\rho} = -1\hat{e}_3$. The 4π pulse locally excites, de-excites, excites, and de-excites the two-level atom medium as it travels through the system. Examining one grid cell in

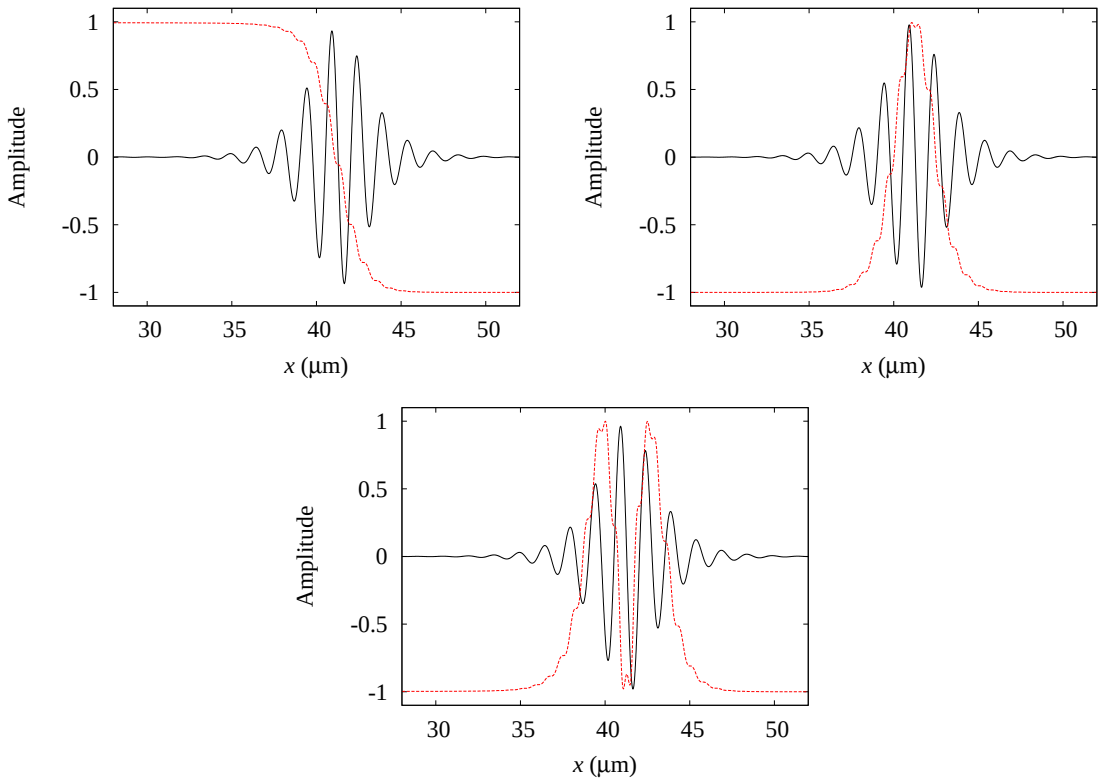

Figure 3.1. Self-Induced Transparency results showing the electric field pulse (black) and population inversion (red). The field pulse is traveling from left to right. The incoming field pulse amplitude is adjusted to correspond to a (top-left) π-pulse, (top-right) 2π-pulse, and (bottom) 4π-pulse. Excellent agreement is seen with results from Ziolkowski *et al.*. Note that the population inversion here is normalized by N_s.

time would reveal the Bloch vector flipping completely from $\vec{\rho} = -1\hat{e}_3$, to $\vec{\rho} = 1\hat{e}_3$, to $\vec{\rho} = -1\hat{e}_3$, to $\vec{\rho} = 1\hat{e}_3$, then back again to $\vec{\rho} = -1\hat{e}_3$.

3.2. Superfluorescence

We apply the Maxwell-Bloch equations with noise to a FDTD simulation of superfluorescence (SF) and compare the results to previous data obtained experimentally [**128**] and theoretically [**129**]. Figure 3.2 shows a diagram of the system studied here. SF is the

cooperative radiation of an initially inverted but incoherent two-level medium resulting from spontaneous buildup of a macroscopic coherent dipole. This is an interesting and suitable case to study with our method because both spatial propagation of light and noise are important. Noise caused by collisional dephasing can seriously disturb SF and change the emission character to amplified spontaneous emission (ASE). We simulate the transition from SF to ASE with increasing dephasing rate, corresponding to the experiment by Malcuit *et al.* on super-oxide ions in potassium chloride ($KCl:O_2^-$) [**128**].

Experimentally the ions inside a cylinder of diameter $d = 80$ μm and length $L = 7$ mm were excited by a short pulse. The total number of excited ions is $N = 3 \times 10^9$. The emission wavelength is $\lambda = 629$ nm. The Fresnel number for the excitation cylinder is $F = A_c/\lambda L \sim 1$, where A_c is the area of the cylinder cross-section. $T_1 = 76$ ns, and T_2 was varied via temperature change. The "cooperative lifetime" or the duration of SF pulse

$$\tau_r = \frac{8\pi A_c T_1}{3\lambda^2 N} \tag{3.9}$$

is 2.7 ps. The estimated delay time for the SF peak after the excitation pulse

$$\tau_d = \tau_r \left[\frac{1}{4}\ln(2\pi N)\right]^2 \tag{3.10}$$

is 94 ps.

Since $F \sim 1$, the EM modes propagating non-parallel to the cylinder axis are not supported [**130**]. Those modes propagating along the cylinder axis do not have a strong radial dependence, nor are there significant diffraction losses. Thus the system, shown in Fig. 3.2, can be considered as 1D in our FDTD simulation. The grid resolution is

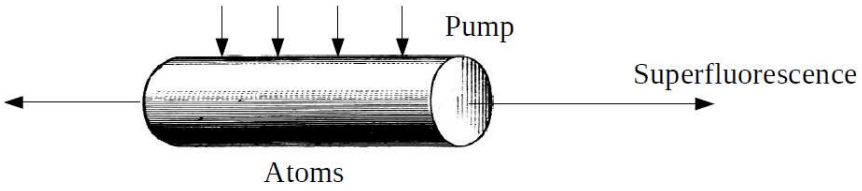

Figure 3.2. Diagram of the system model used to study superfluorescence. Though the simulation is carried out in one dimension, the gain atoms are considered to be in a three-dimensional cylinder of length $L = 7$ mm and diameter $d = 80$ μm. A pump excites the atoms and if the amount of atomic decoherence is small enough, then a superfluorescence pulse is emitted from the system.

$\Delta x = 70$ nm and the area of the cylinder is $A_c = \pi d^2/4$, thus providing the value of V_s in Eq. 3.6. The total running time is $\tau_{sim} = 3$ ns. The Courant number S is set to 0.999999. The magic time step, $S = 1$, was seen to cause an instability in some cases. Setting $S = 1 - 10^{-6}$ preserves the accuracy to an acceptable degree while eliminating the instability at $S = 1$. There is some numerical dispersion and reflection from the absorbing boundary layer, but the error is of the order 10^{-6}. Ignoring non-radiative recombination, the atomic dipole coupling term

$$|\gamma| = \sqrt{\frac{3\lambda^3 \hbar \epsilon_0}{8\pi^2 T_1}} \tag{3.11}$$

is 1.1×10^{-29} C·m.

The simulation is started with the initial condition of all the atoms being excited ($\rho_{22} = N_s$). However, because the atomic population and polarization operators do not commute, the uncertainty principle demands a nonvanishing variance in the initial values of the Bloch vector [**130**]. This results in a tipping angle θ of the initial Bloch vector away from the top of Bloch sphere ($\rho_1 = 0, \rho_2 = 0, \rho_3 = N_s$). The value of θ is given by a

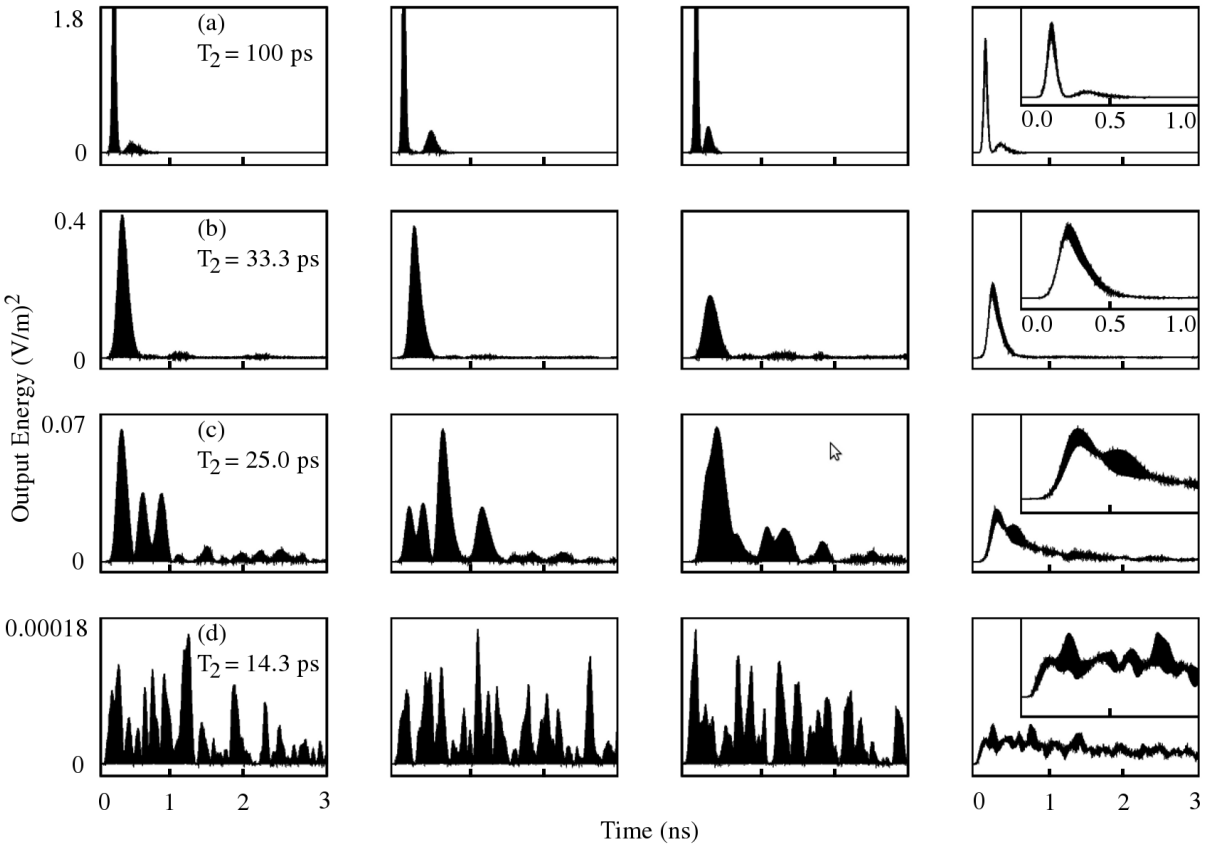

Figure 3.3. Numerical results of the output EM energy (normalized by $\epsilon_0/2$ here) from initially-inverted two-level atoms, obtained by FDTD solution of the Maxwell-Bloch equations with noise. The left three columns show the output energy for three random realizations. The last column on the right shows the output energy averaged over 30 random realizations. All insets in the last column magnify the temporal range $0 < t < 1$ ns. Dephasing time $T_2 = 100$ ps (first row), 33.3 ps (second row), 25.0 ps (third row), and 14.3 ps (fourth row) [**131**].

Gaussian random variable centered at zero with a standard deviation $\theta_T = 2/\sqrt{N_s}$. Since there is no incoherent pumping at $t > 0$, P_r is set to 0.

Figure 3.3 shows the output EM energy at a spatial grid point outside the system for four different values of the dephasing time T_2. When $T_2 = 100$ ps $> \tau_d$, the cooperative

emission characteristic of SF is clearly seen in Fig. 3.3(a). The number of atoms that emit cooperatively is estimated to be

$$N_c = \frac{8\pi c T_1 A_c}{3\lambda^2 L} = 3.5 \times 10^8 \tag{3.12}$$

and is known as the Arecchi-Courtens cooperation number. Since $N_c < N = 3 \times 10^9$, the SF oscillates in time, with the maximal emission intensity at $t \sim 170$ ps. This behavior agrees well with the previous result in [**129**]. For $T_2 = 33.3$ ps $< \tau_d$, there is enough dephasing to disturb the cooperative emission. The emitted pulse broadens and the time delay increases, as shown in Fig. 3.3(b). For $T_2 = 25$ ps, a further damping of superfluorescence is seen in Fig. 3.3(c). As T_2 decreases more, the pulse continues to broaden but the time delay begins to decrease. When T_2 reaches the critical value $\sqrt{\tau_r \tau_d}$ = 15.9 ps, the amount of dephasing is sufficient to prevent the occurrence of cooperative emission. No macroscopic dipole moment can build up and the atoms simply respond to the instantaneous value of the radiation field. Hence, SF is replaced by ASE. Figure 3.3(d) plots the ASE pulse for $T_2 = 14.3$ ps. The time delay is almost immeasurably small and the emission intensity is very noisy. Figure 3.4 compares the delay times taken from our FDTD simulations to previous results obtained experimentally [**128**] and by full quantum-mechanical theory of SF [**129**]. The excellent agreement validates our FDTD-based numerical method. We emphasize that inclusion of the noise terms in Eq. 3.4 is essential to obtain the correct variation of τ_d with T_2. As found in [**128**], the previous approach of modeling the initial fluctuations as random tipping angles of the Bloch vector and ignoring the noise at later times brings about good agreement with experiment only

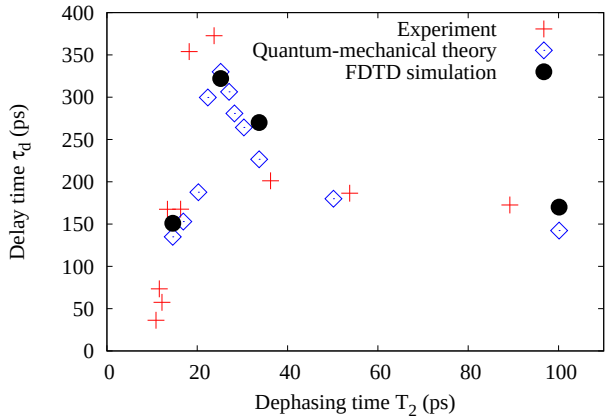

Figure 3.4. Comparison of delay times of emission pulse obtained by our numerical simulation (black solid circles) with previous experimental data (red crosses) and quantum-mechanical calculation results (blue open diamonds). Numerical delay times are obtained from the emission pulses averaged over 30 realizations.

when T_2 is large making the amplitude of the noise terms in Eq. 3.4 small. As the dephasing rate increases, fluctuations can no longer be modeled simply as an initial noise.

We have also studied the decoherence process. As calculated in Sec. 1.4.3, the amplitude of the Bloch vector $\rho_B \equiv |\vec{\rho}| = \sqrt{\rho_1^2 + \rho_2^2 + \rho_3^2} = \sqrt{N_s^2 + 4\rho_{12}\rho_{21} - 4\rho_{22}\rho_{11}}$. In the absence of decoherence, $\rho_{12}\rho_{21} = \rho_{22}\rho_{11}$, and $\rho_B = N_s$. The presence of decoherence decreases the off-diagonal terms of the density matrix, thus $\rho_{12}\rho_{21} < \rho_{22}\rho_{11}$ and $\rho_B < N_s$ [**104**]. We estimate the degree of decoherence through the ratio ρ_3/ρ_B, which is plotted in Fig. 3.5 for four different values of T_2. Each curve is obtained by spatial average of ρ_3 and ρ_B over the entire excitation region and then ensemble-average over 30 realizations.

When the dephasing time is large ($T_2 > \tau_d$), a macroscopic dipole moment is spontaneously formed. The enhanced radiative decay rate results in quick depletion of the population inversion ρ_3. Despite $T_2 \ll T_1$, the decay of ρ_1 and ρ_2 by dephasing is overshadowed by the decay of ρ_3 by SF, leading to a rapid drop of ρ_3/ρ_B in time. This behavior

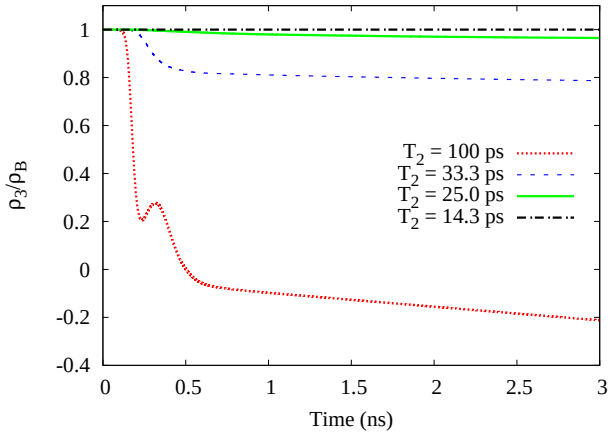

Figure 3.5. The ratio ρ_3/ρ_B as a function of time for $T_2 = 100$ ps (red dotted line), 33.3 ps (blue dashed line), 25.0 ps (green solid line), and 14.3 ps (black dash-dotted line).

is shown by the red dotted line in Fig. 3.5. The non-monotonic decay is caused by SF oscillations as can be seen in Fig. 3.3(a). The oscillatory SF is a result of the number of atoms being greater than the Arecchi-Courtens cooperation number ($N > N_c$). The intensity oscillation leads to an oscillation of population inversion which is 90 degrees out of phase. The local maximum of ρ_3 at $t = 320$ ps (red dotted curve in Fig. 3.5) occurs just before the second peak of intensity at $t = 370$ ps [Fig. 3.3(a)]. As T_2 is reduced, the increased amount of decoherence frustrates the buildup of a macroscopic dipole moment and reduces the radiative decay rate. Consequently, the depletion of population inversion is slowed down. It leads to a slower decay of ρ_3/ρ_B and the disappearance of damped oscillations. Finally when the dephasing time is small enough ($T_2 < \sqrt{\tau_r \tau_d}$), the system stays in a decoherent state, and ρ_3/ρ_B remains close to one for a very long time.

3.3. Lasing Behavior in a Dielectric Slab

We now apply the Maxwell-Bloch equations with noise to a simulation of lasing in a 1D laser made up of a dielectric slab with spatially uniform index of refraction $n = 3$ and length $L = 1$ μm. In this section, incoherent pumping is included ($P_r > 0$) requiring the inclusion of all noise terms from Eqs. 3.1 and 3.3.

At this point it is important to distinguish between a laser amplifier and a laser oscillator [**14**]. Let us examine a system without noise first. If a gain medium is present but the cavity loss is greater than the gain, the output will be amplified but lasing oscillation will not take place. This is a laser amplifier. Lasing oscillation occurs when the net gain is greater than the leakage loss due to the openness of the cavity. When the pumping rate P_r is above a threshold value, the electromagnetic fields build up inside the system until a steady state is reached. When lasing oscillation occurs, the gain completely compensates for leakage loss and the linewidth collapses to zero [**132**]. Definitions of the lasing threshold are varied, so the lasing threshold is defined here as the pumping rate at which lasing oscillation occurs. Introducing noise complicates the matter somewhat and makes the threshold "fuzzy" [**133**].

Population inversion ($\rho_3 > 0$) amplifies spontaneous emission. However, spontaneously emitted photons deplete gain for lasing modes [**103**]. Though the condition necessary (threshold pumping rate) to achieve lasing oscillation without noise may be satisfied, the same may not be true of the same system with noise. Spontaneous emission stimulates emission of photons with the same properties as the spontaneously emitted photons. This reduces the population inversion, providing less gain for cavity modes, thereby increasing the threshold pumping rate for lasing oscillation. Nevertheless, a narrowing of modal

linewidths is seen even below the threshold for lasing oscillation. The largest width of a peak is determined by the cold cavity decay rate. Any amount of amplification decreases the width from this value. In other words, photons at modal frequencies have a longer lifetime than photons off-resonance so more photons are generated via amplification around modal frequencies. A laser amplifier operates in this regime, below the threshold for lasing oscillation, and amplifies the power. As discussed in Sec. 1.2.1, this amplified spontaneous emission (ASE) also causes narrowing of the spectrum around the atomic transition frequency, but is still much more broad than the free spectral range of cavity modes. Both forms of spectral narrowing shall be observed in this section and discussed more in-depth in the next chapter.

Studying lasing behavior in a dielectric slab is a good prelude to studying behavior in random lasers. The quasi mode frequencies and decay rates of the modes of dielectric slabs are known very precisely (see Sec. 1.4.4). The ratio of quasi mode decay rates to frequency spacing $g = k_i/dk$ (independent of frequency in the dielectric slab) is known as the Thouless number [**134**]. From Eq. 1.53, an expression for g is obtained as

$$g = \frac{-1}{2\pi} \ln \left[\frac{(n-1)^2}{(n+1)^2} \right], \tag{3.13}$$

For $n = 3$ (and $L = 1$ μm), $g = 0.2$, meaning the quasi modes are very well separated. Thus, clear and non-overlapping lasing peaks should be discernible from the calculated lasing spectra.

Table 3.1 shows the parameters of interest and defines the variables used in this section. Note that the free spectral range and gain width may also be expressed in terms of wavelength and are denoted by $d\lambda$ and $\Delta\lambda_a$, respectively. The gain width here will be

Physical Quantity	Quantitative Value
Optical period	$T_\lambda \approx 1.7$ fs (430 nm $< \lambda <$ 600 nm)
Quasi mode wavelengths	$\lambda_{m'} = 2nL/m'$
Lasing mode wavelengths	λ_m
Excitation pulse center wavelength	λ_0
Excitation pulse spectral width	$\delta\lambda_0$
Excited state lifetime	$T_1 = 1.0$ ps
Dephasing time	$T_2 = 6.4$ fs
Gain center	$\lambda_a = \lambda_{m'=12}$
Gain spectral width	$\Delta\omega_a = 1/T_1 + 2/T_2$
Atomic density	$N/V = 9.4 \times 10^{23}$
Cavity lifetime	$\tau = 14$ fs
Free spectral range	$dk = \pi/nL$
Spatial grid step	$\Delta x = 1.0$ nm
Temporal step	$\Delta t = 1.7$ as

Table 3.1. Variables and parameters of the light, gain material, cavity, and FDTD grid settings used for the simulation of the dielectric slab ($n = 3$, $L = 1$ μm).

$\Delta\lambda_a = d\lambda \approx 45$ nm. The excitation pulse is only applicable to simulations without noise when some arbitrary input energy is required to initialize the system. In these cases, the pulse width is equal to the gain spectrum width, $\delta\lambda_0 = \Delta\lambda_a$. Though a time step $\Delta t = 1.67$ as ($S = 1/2$) is used to accurately propagate the sharp noise impulses in the numerical grid, data is only output every 8 time steps (decimation by 8 gives a temporal spacing of 13.4 as) to reduce the size of data files. High temporal resolution is not needed in calculating *characteristics* of the evolution of the system. The effect of this on calculations of the spectral properties is negligible since Δt merely determines the maximum frequency ω_{max} as discussed in Ch. 2. Here, even $8\Delta t \ll \pi/\omega_{max}$. Spectra and the evolution of modes in time (using a spectrogram) for decimated data and original data were compared. The differences were less than 1%.

An issue concerning the simulation of fluctuations arises when the population inversion is either very large (ρ_3 near +1) or very small (ρ_3 near -1). We find that if systems are initialized with all atoms in their ground state ($\rho_3 = -1$), the fluctuations associated with the pumping rate P_r are at their largest because ρ_{11} is at its largest value. Such large fluctuations cannot be simulated accurately and the population inversion drops below -1, which is physically impossible. It corresponds to a negative excited state population. To avoid this issue, we initialize all systems at the transparency point, where the excited state population of atoms is equal to that of the ground state ($\rho_3 = 0$). Similarly, when ρ_3 approaches +1, the fluctuations associated with radiative decay are at their largest because ρ_{22} is at its largest value. This causes the inversion to rise about +1, also physically impossible. It corresponds to a negative ground state population. This error occurs in spatial regions of low EM field intensity, where the ground state population is smallest. This numerical issue may be avoided by simply increasing the atomic density. Physically, there is a threshold for the atomic density, below which lasing cannot occur [**90**]. In other words, without enough atoms to provide gain, the losses are too great for lasing to occur. For a volume V, the threshold N_{LC} is given by

$$\frac{N_{LC}}{V} = \left(\frac{2n^3}{c\lambda_a^2}\right)\frac{T_1\Delta\omega_a}{\tau}, \tag{3.14}$$

where τ is the cavity mode lifetime. This threshold is only an approximation; the actual threshold N_{LC} is usually higher (from experience, 2-4 times as high). If the atomic density is set at this threshold density, the ground state population is nearly zero in spatial regions of low field intensity. Thus, fluctuations associated with radiative decay easily force the ground state population to become negative. Though pumping and decay

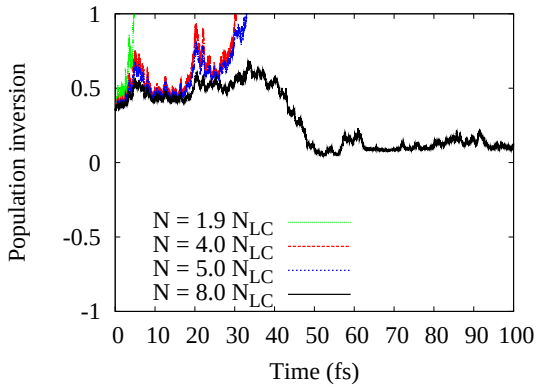

Figure 3.6. Population inversion at one spatial location of low intensity ($x = L/2$). The atomic population is increased as $N = 1.9N_{LC}$ (green line), to $N = 4N_{LC}$ (red line), $N = 5N_{LC}$ (blue line), $N = 8N_{LC}$ (black line). With volume fixed, the atomic density increases with N. For $N < 8N_{LC}$, the population inversion rises above $+1$ meaning the ground state population is negative. For $N = 8N_{LC}$, the depletion of the ground state is restricted, thereby not allowing it to become negative. Simulations here were initialized at their steady-state values to decrease the runtime.

rates are proportional to the instantaneous populations, increasing the atomic density provides a buffer in that the absolute number of pumped and decaying atoms increases. This restricts the depletion of the ground state as evidenced by Fig. 3.6, which shows the temporal behavior of the population inversion at a spatial location of low intensity. Because of the increase in the absolute number of atoms, the populations are prevented from becoming negative. In this figure, the system was initialized to the steady-state population inversion $\rho_3^{(s)}$, found by setting the rate equations to zero and disregarding the stimulated emission term.

Figure 3.6 presents results from a small pumping rate and a very short simulation time. To obtain a population density which forces positiveness of populations for a large range of pumping rates, we set the pumping rate to a large value ($P_r = 100$), and changing N until negative populations are no longer an issue even for long simulation times (~ 100

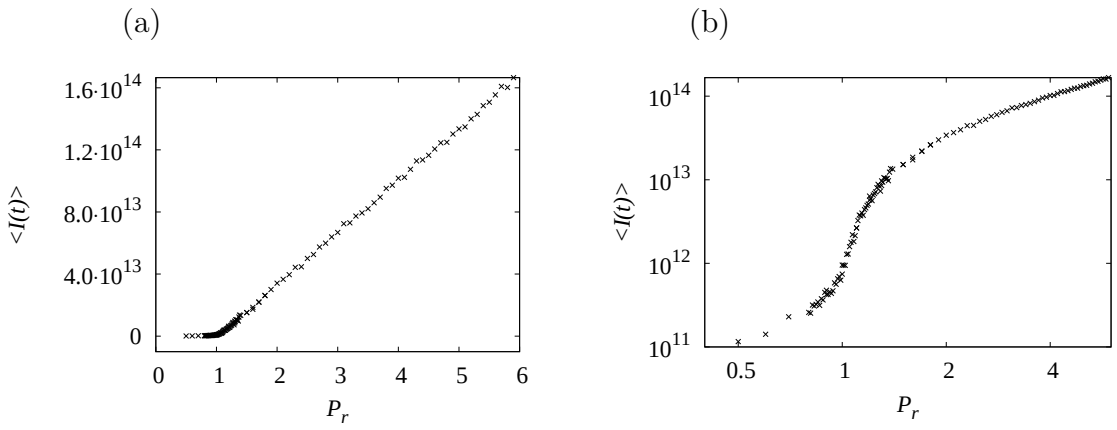

Figure 3.7. Average output intensity $\langle I(t)\rangle$ taken from the last 1% of the simulation time vs. pumping rate P_r with $\lambda_a = 500$ nm (wavelength of quasi mode $m' = 12$). As the pumping rate is increased from 0, the system will reach the transparency point at $P_r = 1$. (a) Above a threshold pumping rate just greater than 1, the gain increases linearly with the pumping rate. Fitting a straight line to this curve gives an estimated threshold pumping rate of $P_r = 1.03$. (b) $\langle I(t)\rangle$ vs. P_r plotted on a log scale. The vertical line A marks the threshold pumping rate found in (a) $P_r = 1.03$. The vertical line B marks $P_r = 3.00$.

ps). $N = 60N_{LC}$ meets this criterion, thereby allowing an investigation of a large range of pumping rates without being concerned with numerical error.

3.3.1. Intensity and Spectral Behavior

The average output intensity in the steady-state regime, averaged over time $\langle I(t)\rangle$ is now examined as the pumping rate P_r is increased. The result is shown in Fig. 3.7, where the atomic transition wavelength is centered on quasi mode 12 ($\lambda_{m'=12} = 500$ nm). Only results from simulations including noise are shown.

As P_r increases from zero, the system reaches the transparency point at $P_r = 1$. This is where the excited state population of atoms is equal to that of the ground state

population; with noise the spatial average is taken ($\langle \rho_3(x) \rangle = 0$). Increasing P_r further, the lasing threshold is reached and intensity increases linearly, as shown in Fig. 3.7(a). This linear increase is characteristic of lasing oscillation which efficiently converts input energy into laser output. Some define a lasing threshold by fitting a straight line to this linear region and marking the intercept with the P_r axis as the lasing threshold. In this case, the intercept is $P_r \approx 1.03$. However, a log-log plot [Fig. 3.7(b)] shows the fuzziness of the lasing threshold. At $P_r = 1.03$, marked by the vertical line A in Fig. 3.7(b), $\langle I(t) \rangle$ is increasing with a super-linear rate meaning lasing oscillation has not yet begun.

The emission spectra reveal more information. First, we shall follow the procedure by Wu and Cao [**36**] to remove the influence of obvious ASE spikes. Single spontaneously emitted photons may travel through the gain medium and become amplified. Each photon is emitted with a single frequency, but many photons are emitted over a large range of frequencies determined by the gain medium. Thus, the spectral width of spikes due to these photons is determined by the spectral resolution, which in this case is the integration time used for the Fourier transformation. This produces many spikes over the entire spectrum. One way of differentiating between ASE spikes and lasing peaks is to smooth the spectrum using three-adjacent-point averaging (3pa) at each discrete data point λ_q via

$$I_{3pa}(\lambda_q) = \frac{1}{3} \sum_{j=q-1}^{q+1} |E(\lambda_j)|^2. \tag{3.15}$$

Although the large ASE spikes are reduced somewhat with this method, their influence is not completely removed. For small pumping rates, the modal peaks are orders of

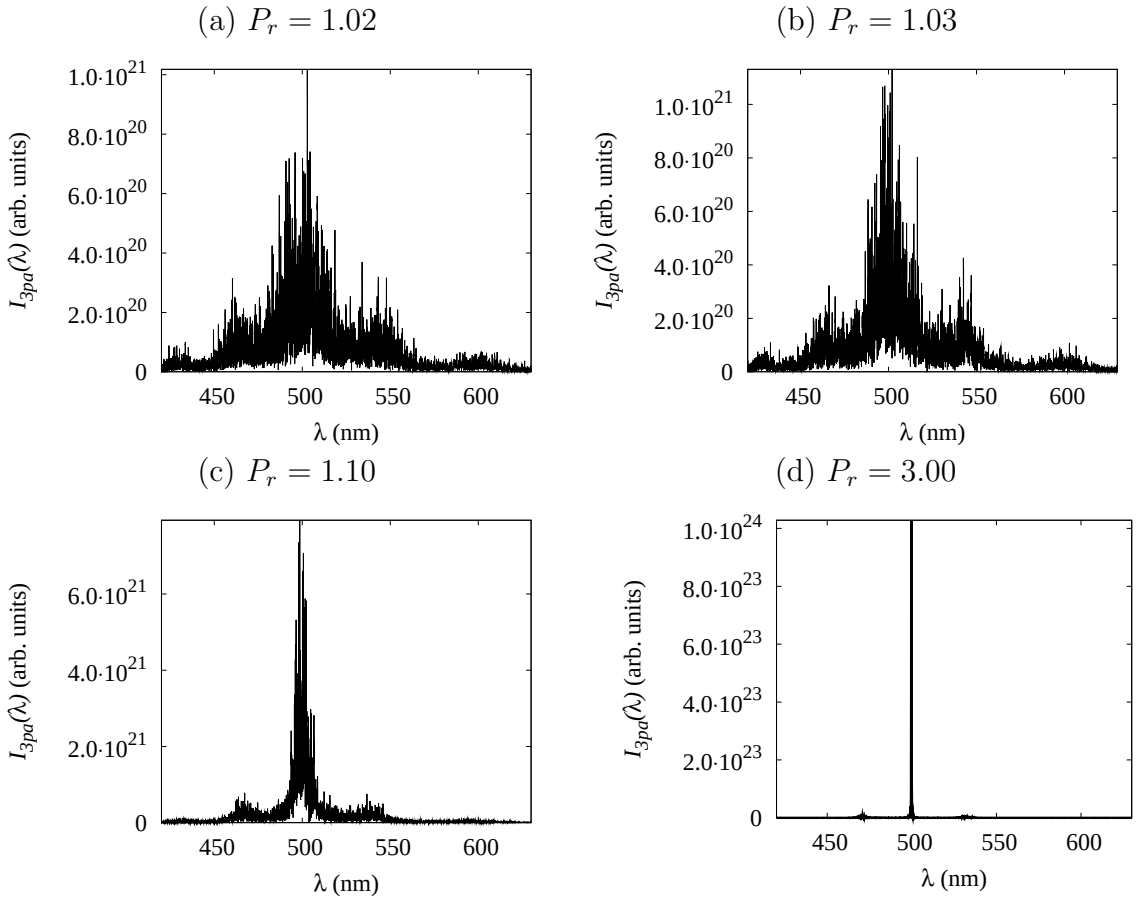

Figure 3.8. Steady-state output intensity $I_{3pa}(\lambda)$ of a dielectric slab laser including noise for (a) $P_r = 1.02$, (b) $P_r = 1.03$, (c) $P_r = 1.10$, and (d) $P_r = 3.00$. Data was smoothed via Eq. 3.15.

magnitude more broad than the ASE spikes. Thus, the sharp delta-function spikes for $P_r \leq 1.10$ (Fig. 3.8) should not be interpreted as lasing peaks.

Figures 3.8(a) and (b) show the spectra for pump rates $P_r = 1.02$ and $P_r = 1.03$, respectively. The spectra were calculated using a Fourier transformation [**135**] over the temporal range 0.33 ps – 3.3 ps. For $P_r = 1.02$ [Fig. 3.8(a)], there is a broad peak at the wavelength $\lambda \approx \lambda_{m'=12} = 500$ nm. Due to gain, the spectral width of this peak is slightly smaller than the atomic linewidth (and the free spectral range) $\Delta\lambda_a = d\lambda$. Behavior

here is clearly due to ASE since $\langle \rho_3(x) \rangle > 0$. For $P_r = 1.03$ [Fig. 3.8(b)], a narrower peak emerges from the background with a linewidth smaller than the spacing between neighboring quasi modes. Nevertheless, Fig. 3.7(b) reveals lasing oscillation has not yet begun for this pumping rate. The same can be said of Fig. 3.8(c), where $P_r = 1.10$. Side peaks are also seen clearly in Figs. 3.8(a-c). These correspond to spontaneous emission into other cavity modes, following the discussion at the beginning of this section.

As the pumping rate increases to $P_r = 3.00$ [Fig. 3.8(d)], the linewidth reduces beyond the spectral resolution and the peak is represented by a single data point. Due to its correspondence with quasi mode $m' = 12$, we name this lasing mode $m = 12$ with $\lambda_{m=12} \approx \lambda_{m'=12} = 500$ nm. This pumping rate is marked in Fig. 3.7(b) as vertical line B, where the $\langle I(t) \rangle$ curve begins to return to a linear increase with P_r. With λ_a centered on quasi mode 12 and a gain spectral width equal to the free spectral range, this laser operates in the single-mode regime. As shall be shown in the next chapter, however, noise can prohibit single-mode lasing when modes are not as well separated.

3.3.2. Linewidth

We now examine the mode linewidth as the pumping rate increases. For very large pumping rates ($P_r > 3.00$), where lasing oscillation has clearly manifested, it is difficult to obtain mode linewidths due to the computational burden of long simulation times (required for adequate spectral resolution). Thus, we focus on the behavior of the linewidth in the ASE region approaching the lasing oscillation region.

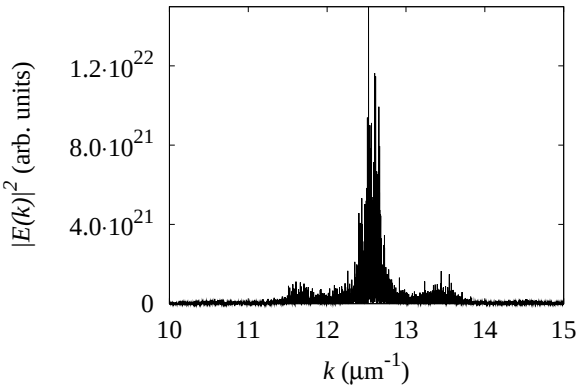

Figure 3.9. Steady-state output intensity $|E(k)|^2$ including noise for $P_r = 1.10$, above the lasing threshold. For this pumping rate, the lasing peak is dramatically narrower than smaller pumping rates. Data is plotted in frequency space to illustrate the symmetry of the spectrum.

Not including noise results in a lasing peak in the emission spectrum with a delta function having zero linewidth. The 'width' of the peak is only determined by the integration time used for the Fourier transformation. However, spontaneous emission forces the phase of the mode operator to undergo a sort of Brownian motion [**132**] and broaden the delta function into a Lorentzian. Knowing the functional form of the curve, we are able to determine the linewidth of modes.

We study mode 12 shown in Fig. 3.8. As the pumping rate increases, the linewidth of this mode clearly reduces. Though for smaller pumping rates this is not due to lasing action, ASE dramatically reduces linewidths as well (see discussion in Sec. 1.2.1). The spectrum at an intermediate pumping rate $P_r = 1.10$ [Fig. 3.9] is chosen as a representative spectrum on which to test the following linewidth calculation method. Note that data is now plotted in terms of frequency k. Due to the symmetry in k, finding the linewidth is simpler than when considering λ.

There are two issues here in objectively obtaining the linewidth of the modes: the noisiness of the spectrum and the background. Fitting a Lorentzian curve to noisy data may be possible after smoothing the data and using a high-pass filter to remove the background. However, methods of smoothing and filtering can be extremely subjective. Instead, we use a "Lorentz error function" (not to be confused with the Lorentzian error function). An error function is similar to a cumulative distribution function, but integrated from 0 to k rather than ∞ to k. If the Lorentzian function $L(k)$ is centered at k_0 rather than 0, then

$$L(k) = \left(\frac{2A_l}{\pi}\right) \frac{s^2}{(k-k_0)^2 + s^2}, \tag{3.16}$$

where A_l is the amplitude and s is the HWHM. The Lorentz error function is

$$L_{EF}(k) \equiv \int_{k_0}^{k} L(k')dk' = \left(\frac{2A_l s}{\pi}\right) \tan^{-1}\left(\frac{k-k_0}{s}\right). \tag{3.17}$$

Integrations are limited to the spectral range of the modes. To determine this range, we find the minimum of $|E(k)|^2$ between neighboring modes. In this slab case, modes are so well separated that the spectral range of quasi modes may be used. For example, the frequency integration range for lasing mode 12 is given by $k_{m'=11.5} < k < k_{m'=12.5}$.

It is straightforward to measure the linewidth $\delta k = 2s$ of the Lorentzian curve by examining $L_{EF}(k)$ because the noisiness associated with the spectrum itself is gone. Figure 3.10 shows how this is done and Fig. 3.11 shows an example of $L_{EF}(k)$ resulting from integration of the data in Fig. 3.9. We see that

$$\lim_{k\to\infty} \left(\frac{2A_l s}{\pi}\right) \tan^{-1}\left(\frac{k-k_0}{s}\right) = A_l s \tag{3.18}$$

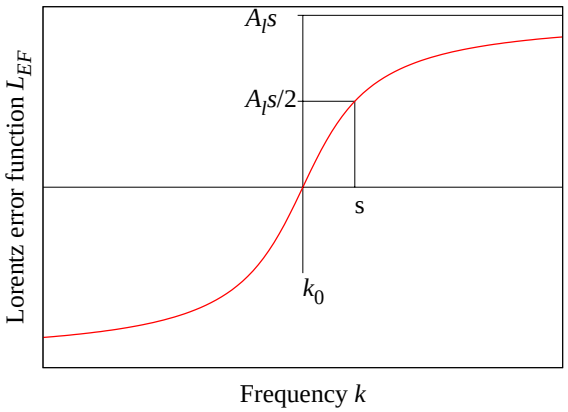

Figure 3.10. The Lorentz error function $L_{EF}(k)$ asymptotically approaches $A_l s$. At the half max $A_l s/2$, $L_{EF}(k)$ has reached the half width s.

and $L_{EF}(k_0 \pm s) = \pm A_l s/2$. Thus, we may measure s after obtaining L_{EF} from the integral in Eq. 3.17. The background itself is still large, but this may be incorporated into the error function if the background is relatively flat. A constant term $+C$ need only be added to Eq. 3.16 thereby changing Eq. 3.17 to

$$L_{EF}(k) = \left(\frac{2A_l s}{\pi}\right) \tan^{-1}\left(\frac{k - k_0}{s}\right) + C(k - k_0). \tag{3.19}$$

A straightforward measurement of the half width at half max s is found to give a reasonable estimate of the linewidth. However, choosing the point $A_l s/2$ at which to measure s is fairly subjective. Moreover, the measurements of s on either side of k_0 are typically different due to the background not being completely flat. The non-flat background of the spectrum makes it difficult to predict how its error function will behave. This makes these measurements unreliable.

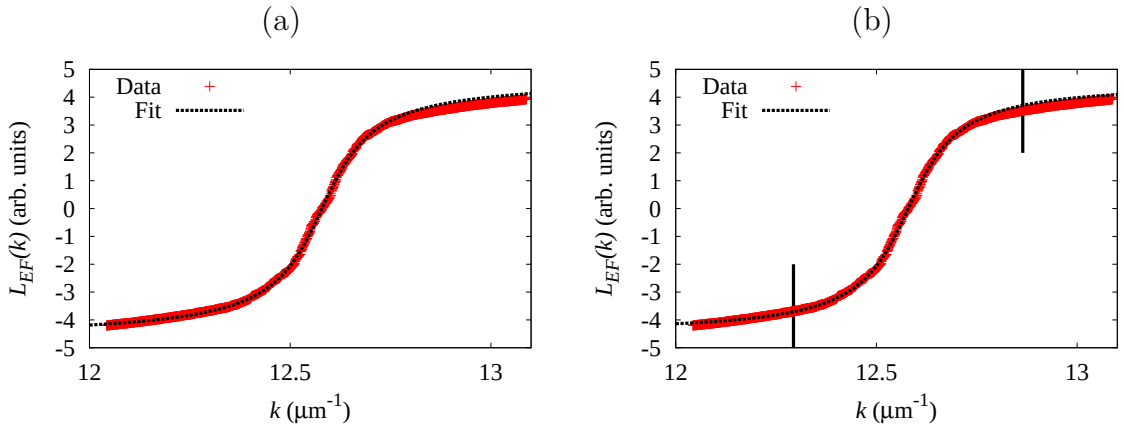

Figure 3.11. (a) $L_{EF}(k)$ obtained for mode 12 from the spectrum Fig. 3.9. The fitting equation was Eq. 3.17. The data, and thus the fit, is asymmetric due to the background resulting in some fitting error. The width found was $s = 0.0952 \times 10^{-2}\ \mu\text{m}^{-1} \Rightarrow \delta\lambda \approx 7.53$ nm. (b) The fitted region was limited to $k_0 \pm 3s$, using s calculated in (a). Vertical black lines mark the fitting region. The fitting equation was Eq. 3.19. The width found was $s = 0.0955 \times 10^{-2}\ \mu\text{m}^{-1} \Rightarrow \delta\lambda \approx 7.56$ nm.

Therefore, we use the software Fityk [**136**] to fit the data obtained by the integral in Eq. 3.17. The function of merit is chi-square:

$$\chi^2(a) = \sum_{i=1}^{N} \left[\frac{y_i - y(x_i;a)}{\sigma_i}\right]^2 = \sum_{i=1}^{N} w_i \left[y_i - y(x_i;a)\right]^2 \tag{3.20}$$

Weights are based on standard deviations, $w_i = 1/\sigma_i^2$ and squares of residuals are minimized. The global minimum of χ^2 is searched for. Fityk implements the Levenberg-Marquardt optimization method. It is well known and described in many standard textbooks (e.g., [**137**]). There are three fitting parameters in Eq. 3.16: A_l, s, and k_0. Initialization of the center frequency k_0 may be done objectively through a maximum finding routine after the data has been smoothed with iterative three-adjacent-point averaging (i3pa). With $I^{(0)}_{3pa}(k_q)$ defined by Eq. 3.15, the smoothed function $I_{i3pa}(k_q)$ at each discrete

wavenumber k_q is explicitly calculated as

$$I_{i3pa}(k_q) = \sum_{u=1}^{M_s/3} \sum_{j=q-1}^{q+1} I_{3pa}^{(u-1)}(k_j), \tag{3.21}$$

where M_s is the total number of data points in the spectrum and the sum over i is done recursively. The number of iterations $M_s/3$ was determined by trial and error. Careful examination of the original spectra help determine a valid frequency range so that the smoothing procedure does not destroy other lasing peaks that might be within. Note that the smoothed spectrum $I_{i3pa}(k)$ is *only* used to find the initial value of k_0 (though it may be adjusted slightly during fitting). Information concerning linewidth is effectively destroyed by this smoothing. No matter the initial values of the fitting parameters, we have found that the Levenberg-Marquardt method always manages to converge to a single solution here (though it will take longer if the initial values are further from the solution, of course).

The results of fitting the analytical form of $L_{EF}(k)$ to the integrated data are shown in Fig. 3.11(a). The integration in this case was performed over the spectral region $k_{m'=11.5} < k < k_{m'=12.5}$. The linewidth in terms of wavelength is found by

$$\delta\lambda = \frac{4\pi s}{k_0^2}. \tag{3.22}$$

The data is fit extremely well, with the fit yielding a linewidth of $\delta\lambda_{12} \approx 7.53$ nm. As the linewidth becomes increasingly narrow, background data from spectral regions far away from k_0 make it more difficult to find an accurate fit. Thus, we take the linewidth from the calculation above and consider a smaller spectral region, e.g., $\pm 3s$. This range

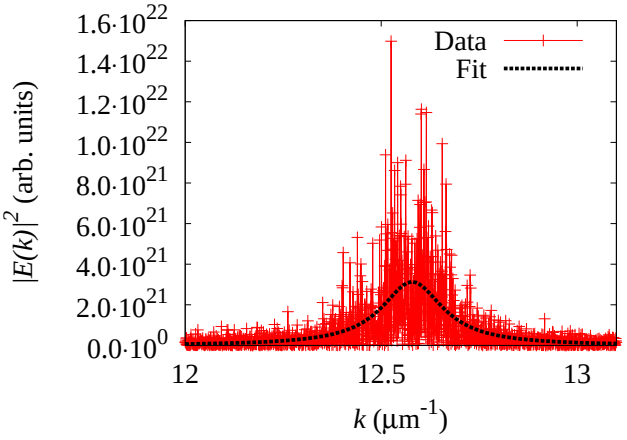

Figure 3.12. Lorentzian curve $L(k)$ (black dashed line) constructed from fitting the spectrum $|E(k)|^2$ (red crosses). Fit was obtained from Eq. 3.19 [see Fig. 3.11(b)]. The linewidth is approximately 0.19 μm^{-1} (7.6 nm).

was found by trial and error to give the most consistent results. Within this range, the background is flatter, so we employ Eq. 3.19 with the added constant term to fit the data. The result is shown in Fig. 3.11(b). When limiting the fit to a smaller range, the areas of high curvature are fit much better, but the regions further away from the center frequency are fit poorly. Comparing the result from Figs. 3.11(a) and (b), we see there is not much difference ($\approx 0.4\%$ difference). However, this procedure proves useful for larger pumping rates where linewidths are smaller.

To see the results of the fitting more explicitly, Fig. 3.12 plots the Lorentzian function of Eq. 3.16 using the parameters from the fit in Fig. 3.11(b). Since the Lorentz error function is essentially an average of the noisy spectrum, the resulting Lorentzian curve from the fit appears as an average of the spectrum.

We now use this method to examine the linewidth as the pumping rate increases. Because we already know the qualitative behavior of the linewidth with respect to P_r,

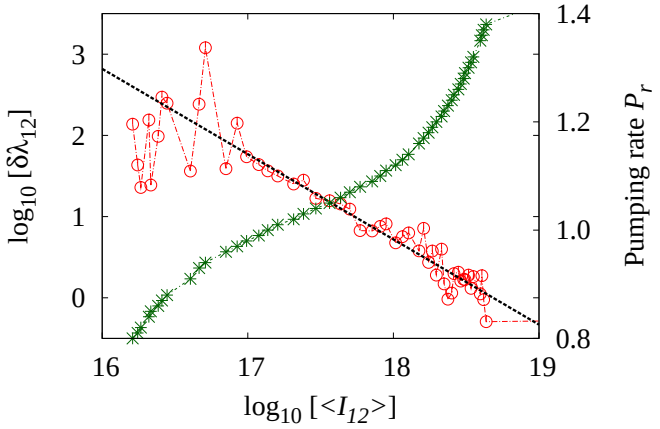

Figure 3.13. Linewidth $\delta\lambda_{12}$ of lasing mode 12 (red circles) and pumping rate (green asterisks) vs. the steady-state modal intensity $\langle I_{12}(k)\rangle$. The slope of the linear fit (black line) to the linewidth curve is $-1.05 \pm 4.54\%$, meaning $\delta\lambda_{12} \propto \langle I_{12}(k)\rangle^{-1}$, the linewidth trend predicted by Schawlow and Townes.

the linewidth is instead compared with the steady-state intensity of the mode itself $\langle I_{12}\rangle$. Schawlow and Townes predicted [**12**] how the linewidth should behave with respect to modal power, which is equivalent to intensity in our case. Ignoring the coefficients, they found $\delta\lambda \propto \langle I\rangle^{-1}$. Figure 3.13 reveals the data and a linear fit of $\log_{10}[\delta\lambda_{12}]$ to $\log_{10}[\langle I_{12}\rangle]$. The slope is approximately -1 meaning $\delta\lambda \propto \langle I\rangle^{-1}$. The range of fitting was determined by the threshold pumping rate and the pumping rate at which the linewidth is no longer calculable due to limitations on the spectral resolution. Note that this region may be extended by simply extending the simulation runtime, but the data presented is enough to witness the Schawlow-Townes linewidth behavior.

CHAPTER 4

Effects of Noise on Random Lasers

A FDTD-based numerical method to simulate fluctuations in macroscopic systems without prior knowledge of cavity modes is most useful when studying open complex systems. For example, it can be difficult to study random systems where information about the modes of a random system is not readily available. In higher dimensional (> 1) random lasers, when the localization length is larger than the system size, discrete lasing peaks are still observed. These peaks cannot correspond to spatially localized modes, so their origin has been the subject of much debate. Additionally, if the cavity is very leaky, the significant spectral overlap of quasi modes of the cold cavity makes it difficult to distinguish one mode from another. If lasing oscillation occurs in this type of system, it may be difficult to determine the lasing characteristics. For example, lasing with nonresonant feedback produces a continuous spectrum resulting in emission statistics which differ greatly from the statistics of ordinary lasers [**138, 139, 140, 141**]. But is the continuity of the spectrum due to intrinsic spectral overlap of lasing modes or is it that experimental observations have a finite spectral resolution which cannot detect the sharp closely spaced lasing peaks? Furthermore, it can be difficult to distinguish true lasing oscillation due to nonresonant feedback from amplified spontaneous emission (ASE). In this chapter, we employ the numerical model developed in the previous chapter to simulate noise in random lasers. A random laser with overlapping modes is simulated which takes advantage of the benefits provided by this method. Without noise, the transition to lasing

oscillation is clear and easily defined. With noise, there can be a significant transition region from amplified spontaneous emission to lasing oscillation. It will be shown that a lasing threshold is not so easily defined in this case. Numerical investigation into these poorly understood regimes of operation in weakly scattering random lasers, ASE and lasing with nonresonant feedback, is initiated here. It is hoped that future studies with this method will provide clues toward answering the above questions and clarifying the mechanisms responsible for lasing in such systems.

As in the previous chapter, the dominant noise is from the atoms rather than the light field. The amplitude of classical noise accompanying the field decay (as discussed in Ch. 2) is proportional to $\sqrt{n_T}$, where n_T is the thermal photon number. At room temperature the number of thermal photons at visible frequencies ($\hbar\omega \sim 1$ eV) is on the order of 10^{-17}. This can be interpreted in a quantum mechanical picture as that most of the time there are no thermal photons at visible frequencies in the system. Thus, the noise related to field decay is neglected in this chapter. At higher temperatures or longer wavelengths, this noise becomes significant and it can be incorporated into the FDTD algorithm following the approach we developed in Ch. 2.

First, information concerning the three different random systems studied here and certain numerical issues is presented in Sec. 4.1. An analysis of these systems using the linear gain model (see Sec. 1.4.4.2) in Sec. 4.2 provides a solid basis of understanding. These results are compared to those using the Maxwell-Bloch equations both with and without noise in Sec. 4.3. Section 4.4 presents a summary of all results in this chapter.

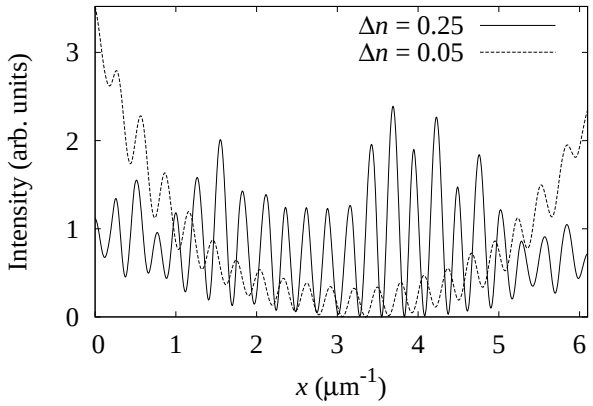

Figure 4.1. Intensity distributions of representative modes in a random system with $\Delta n = 0.25$, $\lambda = 10.8\ \mu\text{m}^{-1}$ (solid line) and $\Delta n = 0.05$, $\lambda = 10.6\ \mu\text{m}^{-1}$ (dashed line). With $\Delta n = 0.25$, modes are typically more concentrated within the random system while for $\Delta n = 0.05$, modes are concentrated on the outer boundaries of the system.

4.1. Random System

The 1D random system considered in this chapter is composed of $N = 41$ layers. Dielectric layers with index of refraction $n_1 > 1$ alternate with air gaps ($n_2 = 1$) resulting in a spatially modulated index of refraction $n(x)$. The scattering strength may be varied by adjusting the index contrast $\Delta n = n_1/n_2 - 1$. The system is randomized by specifying different thicknesses for each of the layers as $d_{1,2} = \langle d_{1,2} \rangle (1 + \eta\zeta)$ where $\langle d_1 \rangle$and $\langle d_2 \rangle$ are the average thicknesses of the layers, $0 < \eta < 1$ represents the degree of randomness, and ζ is a random number in (-1,1). The average thicknesses are $\langle d_1 \rangle = 100$ nm and $\langle d_2 \rangle = 200$ nm giving a total average length of $\langle L \rangle = 6100$ nm. The grid origin is set at $x = 0$ and the length of the random structure L is normalized to $\langle L \rangle$. The degree of randomness is set to $\eta = 0.9$ and the index of refraction outside the random media is $n_0 = 1$.

Three regimes shall be studied in this chapter by adjusting the refractive index n_1 and the spatial gain region. In the first regime, the indices of refraction of the dielectric layers are $n_1 = 1.25$ and the air gaps $n_2 = 1$. This yields a localization length $\xi \gtrsim L$. Though not in the localization regime, modal intensity distributions, shown in Fig. 4.1, are more concentrated inside the system than in the ballistic case where intensity distributions are concentrated on the outer boundaries of the system. As will be shown, the changes due to noise are less significant in this regime than in the ballistic regime. In the second regime, the indices of refraction of the dielectric layers are $n_1 = 1.05$ and the air gaps $n_2 = 1$. This is an example of a random 1D weakly scattering system. The parameters yield a localization length $\xi \gg L$, putting the system in the ballistic regime. As indicated by experiments and preliminary numerical investigations, discrete lasing peaks seem to manifest themselves more clearly with partial pumping. This notion shall be tested with noise included. Thus, the third system studied is a random laser in the ballistic regime with partial pumping.

The Thouless number g is used again to reveal the amount of overlap of quasi modes of this random system. Because the quasi mode decay rates and frequency spacing between different modes are no longer independent of frequency, we calculate the ratio of the average quasi mode decay rate to the average frequency spacing $g = \langle k_i \rangle \,/\, \langle dk \rangle$. Figure 4.2 shows the transmission spectrum $\mathcal{T}(k)$ for both cases of index contrast. With higher index contrast $g = 0.5$, meaning mode spacing is twice the average mode width. For lower index contrast, $g = 1.0$, meaning the quasi modes are no longer separated, but neither are they significantly overlapping. In 1D, the decay rate and frequency spacing reduce at the same rate with increasing L. Thus, the Thouless number is mostly dependent on

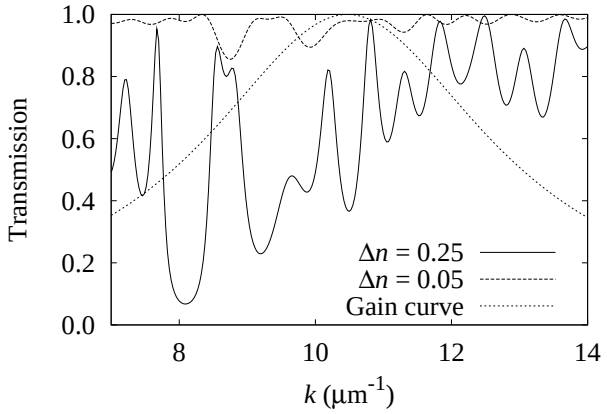

Figure 4.2. Transmission spectrum $\mathcal{T}(k)$ for $\Delta n = 0.25$ (solid line), $\Delta n = 0.05$ (dashed line), and the gain curve (dotted line) for the Maxwell-Bloch simulations. The Thouless number is $g = 0.53$ for $\Delta n = 0.25$ and $g = 1.00$ for $\Delta n = 0.05$. The gain curve spans roughly ten modes in each case.

the index of refraction and can be approximated using the expression obtained for the dielectric slab (Eq. 3.13)

$$g \approx \frac{-1}{2\pi} \ln \left[\frac{(n_{eff} - 1)^2}{(n_{eff} + 1)^2} \right], \tag{4.1}$$

where n_{eff} is the effective index of refraction for the random system. Even for an incredibly small index contrast $\Delta n = 10^{-4}$, the Thouless number is only 3. However, we would like to avoid such a small index contrast since it may present numerical problems and does not increase the Thouless number greatly. Nevertheless, a large amount of information may be obtained for $g = 1$. Modes are clearly overlapping to a greater extent than in the dielectric slab case where $g = 0.2$.

Table 4.1 shows the parameters of interest and defines the variables used in this section. Note that the free spectral range and gain width may also be expressed in terms of wavelength and are denoted by $d\lambda$ and $\Delta\lambda_a$, respectively. The gain width here is $\Delta\lambda_a =$

Physical Quantity	Quantitative Value
Optical period	$T_\lambda \approx 2$ fs (400 nm $< \lambda <$ 1200 nm)
Quasi mode wavelengths	$\lambda_{m'}$
Lasing mode wavelengths	λ_m
Excitation wavelength	λ_0
Excitation spectral width	$\delta\lambda_0$
Excited state lifetime	$T_1 = 1.0$ ps
Dephasing time	$T_2 = 1.3$ fs
Gain center	$\lambda_a = 600$ nm
Gain spectral width	$\Delta\omega_a = 1/T_1 + 2/T_2$
Atomic density	$N/V = 4.3 \times 10^{23}$
Spatial grid step	$\Delta x = 1.0$ nm
Temporal step	$\Delta t = 1.7$ as

Table 4.1. Variables and parameters of the light, gain material, cavity, and FDTD grid settings used for the simulation of the random system ($L = 6.1$ μm).

$10(d\lambda) \approx 267$ nm, shown in terms of the wavenumber k in Fig. 4.2. The excitation pulse is only applicable to simulations without noise when some arbitrary input energy is required to initialize the system. In these cases, $\delta\lambda_0 = \Delta\lambda_a$. Though a time step $\Delta t = 1.67$ as is used to accurately propagate the sharp noise impulses in the numerical grid, data is only output every 8 time steps (decimation by 8 gives a temporal spacing of 13.3 as) to reduce the size of data files.

The random laser exhibits the same numerical issue as the dielectric slab laser as shown in Fig. 3.6. To obtain a population density which retains positiveness of populations for a large range of pumping rates, we set the pumping rate to a large value ($P_r = 100$), and changing N until negative populations are no longer an issue even for long simulation times (~ 100 ps). $N = 60N_{LC}$ still meets this criterion, thereby allowing an investigation of a large range of pumping rates without being concerned with numerical error.

Furthermore, the random laser exhibits a numerical issue not present in the dielectric slab case. With the dielectric layers of index $n_1 > 1$ separated by air gaps $n_2 = 1$, adding noise with high frequency components couples them to high frequency modes resonating between two dielectric layers. These modes have a wavelength $\lambda < 200$ nm, much smaller than the atomic transition wavelength $\lambda_a = 600$ nm. Being so far from the maximum of the gain spectrum, they should not lase in a physical situation. These high frequency contributions are ignored completely by only considering EM fields within the wavelength range $400 < \lambda < 1200$ nm. In frequency-space, this range is centered around $k_a = 2\pi/\lambda_a = 10.5\ \mu\text{m}^{-1}$, and thus, provides an accurate view of EM behavior in the random laser.

4.2. Analysis with Linear Gain

Using the method developed in Sec. 1.4.4, the lasing modes with linear gain are now calculated in the three regimes mentioned earlier: high index contrast, low index contrast, low index contrast with partial pumping. The benefit of this method is that the lasing thresholds may be estimated quickly and easily, at least relative to one another. This method considers gain to be independent of frequency. The results in this section are discussed in relation to the Maxwell-Bloch simulations in the sections following, where the properties of the gain medium are given in Table 4.1. As shall be shown, the lasing thresholds of the individual modes in the presence of frequency-independent linear gain plays a large role in determining lasing behavior in the presence of gain saturation and spontaneous emission. However, due to the frequency independence of the linear gain model used here, the lasing modes do not experience frequency pulling. Thus, the lasing

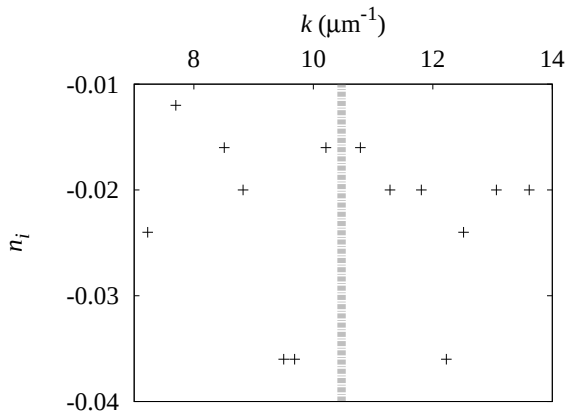

Figure 4.3. The frequencies k and lasing thresholds n_i of lasing modes (marked with crosses) with linear gain for a random system with index contrast $\Delta n = 0.25$. The vertical dashed gray line marks the gain center frequency k_a for the Maxwell-Bloch simulations in the sections following. In this case, the modes nearest k_a have small thresholds (small $|n_i|$) which are well separated from the thresholds of neighboring modes.

modes studied in this section have slightly different frequencies than the modes studied in the sections following.

Figure 4.3 reveals the lasing frequencies and thresholds of the random system with index contrast $\Delta n = 0.25$. The crosses denote frequency k and threshold (imaginary part of the index of refraction n_i) values required to satisfy outgoing-only boundary conditions. In this case, due to the high index contrast, lasing thresholds are well separated. Note that the modes nearest the gain center k_a (for the Maxwell-Bloch simulations), marked with a vertical gray line in the figure, have small thresholds (small $|n_i|$) which are well separated from the thresholds of neighboring modes. It will be shown that these two modes serve as the two dominant modes when gain saturation and noise are taken into account. The higher frequency mode at $k = 10.8\ \mu\text{m}^{-1}$ has a smaller threshold than the

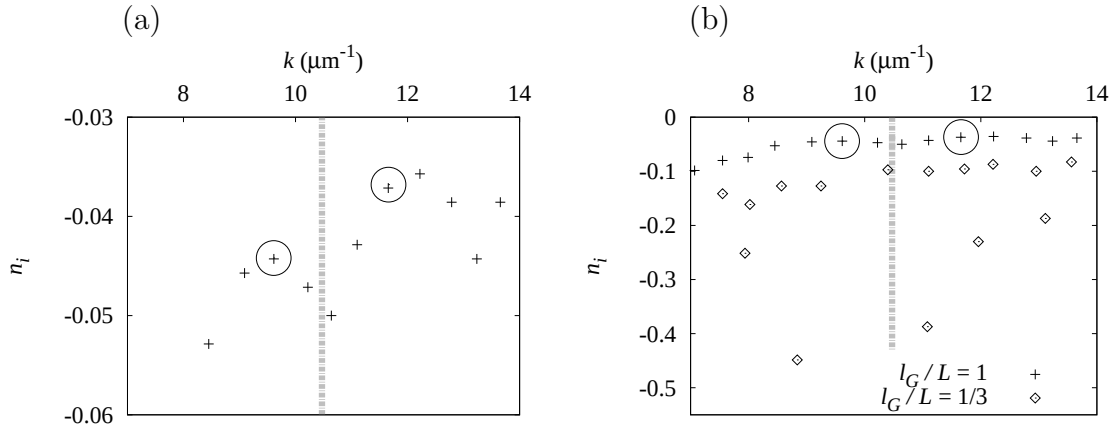

Figure 4.4. The lasing frequencies k and thresholds n_i of modes with linear gain in a weakly scattering random system with uniform gain (crosses) and nonuniform gain (open diamonds). The vertical dashed gray line marks the Maxwell-Bloch gain center frequency k_a. (a) Lasing modes with uniform gain only. The two strongest modes with uniform gain found by the Maxwell-Bloch simulations in the following section are circled. The circled modes have lower values of $|n_i|$ than the modes nearest k_a. (b) Uniform gain and nonuniform gain results are compared. With $l_G/L = 1/3$, the number of lasing modes does not reduce, but some lasing modes have much larger thresholds which effectively increases the frequency spacing of modes with small thresholds.

lower frequency mode at $k = 10.2\ \mu\text{m}^{-1}$. Two modes at $k \approx 8\ \mu\text{m}^{-1}$ also have small lasing thresholds, as expected from the transmission spectrum $\mathcal{T}(k)$ in Fig. 4.2.

Figure 4.4 compares lasing frequencies and thresholds with uniform and nonuniform gain distributions in the system with low index contrast. All lasing modes in this regime have larger thresholds than modes in the system with high index contrast, as expected. For uniformly distributed linear gain in Fig. 4.4(a), the lasing modes nearest the gain center have larger thresholds than their neighboring modes. When gain saturation is taken into account, the modes with the largest amplitudes correspond to the circled modes, not the modes closest to the gain center.

For a nonuniform distribution of linear gain ($l_G/L = 1/3$) [Fig. 4.4(b)], the lasing thresholds increase dramatically. It was suggested [**47**] that it is easier to obtain discrete peaks with partial pumping because there are fewer lasing modes when a system is locally pumped. This previous numerical study neglected the influence of gain on the real part of the index of refraction n_r. When the gain $|n_i|$ approaches the index contrast Δn, it has a large effect on the system. These effects shall be studied more in-depth the next chapter. For now, it is enough to note that the number of lasing modes does not reduce. Instead, the lasing thresholds of the available lasing modes become increasingly separated. Consequently, the lasing frequencies also become increasingly separated. This makes it is easier to obtain discrete lasing peaks with partial pumping.

4.3. From Amplified Spontaneous Emission to Lasing Oscillation

4.3.1. High Index Contrast

We begin by studying the case with a higher index contrast $\Delta n = 0.25$ by employing the Maxwell-Bloch equations with noise terms included. The localization length ξ of the system is calculated following the method in Sec. 1.1.2 which gives $\langle \xi \rangle \approx 20$ μm over the wavelength range 500 nm $\leq \lambda \leq$ 750 nm. With $\xi \gtrsim L$, the system is closer to the localization regime than the low index contrast case. Figure 4.1 shows a representative intensity distribution of a mode in this system. It is more concentrated inside the system than the intensity distribution in the low index contrast case.

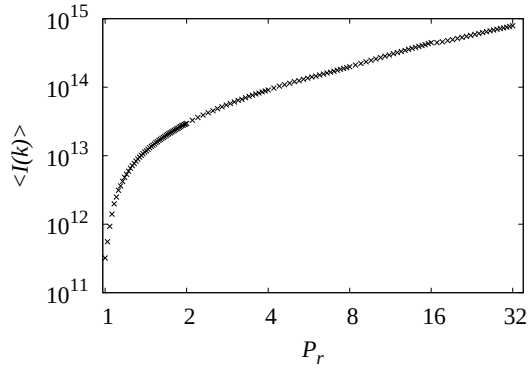

Figure 4.5. Average steady-state intensity $\langle I(k)\rangle$ vs. pumping rate P_r for a random structure with $\Delta n = 0.25$, $\lambda_a = 600$ nm, and $\Delta\lambda_a = 10(\Delta\lambda) = 267$ nm. The laser transitions from the ASE regime to lasing action.

Figure 4.5 shows the steady-state intensity vs. pumping rate. To avoid numerical problems mentioned earlier, $\langle I\rangle$ is found by a spectral integration

$$\langle I(k)\rangle = \int_{k_l}^{k_u} |E(k')|^2 dk', \tag{4.2}$$

where $k_l = 2\pi/1.2$ μm^{-1} and $k_u = 2\pi/0.4$ μm^{-1}. The system transitions from the ASE regime to lasing oscillation within this range of pumping rates. Similar to behavior in the dielectric slab laser [Fig. 3.7], it is unclear where to define the lasing threshold.

Output intensity is observed to reach a fairly steady state at least by a simulation time of $t = 16.6$ ps no matter the pumping rate. Spectra are obtained from the range 16.6 ps – 33.2 ps. For every case, the electric field is sampled at the grid point at the edge of the random system. This point determines the output intensity and is identical in character to results from sampling the field completely outside the system and before the absorbing boundary. The three-adjacent-point averaging procedure is used to help remove the influence of obvious ASE spikes so they are not mistaken for lasing peaks. All

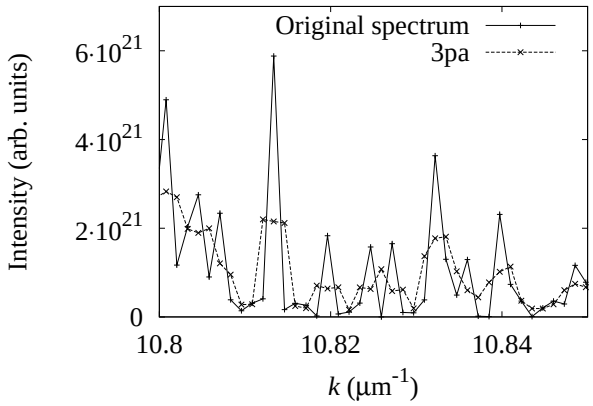

Figure 4.6. Original steady-state intensity $|E(k)|^2$ compared to the three-adjacent-point averaged spectrum $I_{3pa}(k)$. Large spikes determined only by the integration time of the Fourier transformation are significantly reduced. However, the influence of the spikes is not completely removed.

spectra shown here and henceforth are smoothed at each discrete wavenumber k_q via Eq. 3.15. Lasing peaks are wider than these spikes except for very large pumping rates where lasing action dominates ASE anyways. Thus, this smoothing does not affect lasing peaks. Figure 4.6 shows the results of this smoothing. Although the large spikes are reduced somewhat, their influence is not completely removed. Quantities other than the emission spectrum are needed to help differentiate between ASE and lasing action.

In literature, the definition of the lasing threshold varies greatly [**142, 143, 144, 145, 146, 147**]. The ASE regime itself exhibits "laser-like" qualities, such as spectral narrowing. The "fuzziness" [**133**] of the lasing threshold is well known for large values of β, where β is the spontaneous emission coefficient. This parameter essentially indicates how much spontaneous emission is coupled into the lasing modes. Eventually, for $\beta = 1$, the so-called "thresholdless" laser [**148**] manifests itself and $\langle I \rangle$ vs. P_r becomes a straight line. Smaller values of β push the spontaneous emission regime (small P_r values where

spontaneous emission is not yet being amplified) toward zero. In this case, the P_r intercept of a straight-line fit to $\langle I \rangle$ vs. P_r in the LO region gives an accurate lasing threshold. The lasers studied here are operating far from the thresholdless regime, but the threshold fuzziness remains.

The Fano-Mandel parameter [**149**], essentially the intensity variance, was found to serve as a reliable indicator of the lasing threshold [**150**]. For most practical applications, it defines a finite value for the threshold [**151, 152**]. A direct calculation of the temporal variance for the random laser is complicated by the numerical problem of unphysical high frequency components altering the output signal. For this thesis, the transition from ASE to lasing oscillation is examined and the determination of precise lasing thresholds is left for future work.

Figure 4.7 shows the steady-state spectra for increasing pumping rates with and without noise. Initially, for $P_r = 1.00$ in Fig. 4.7(a), there is no lasing for the case without noise. With noise, there is a broad background peak centered around $k_a = 10.5$ μm^{-1}. The width of the broad peak is roughly 4–5 μm^{-1}. The atomic linewidth is $\Delta k_a = 4.7$ μm^{-1} meaning the properties of the broad peak are determined by the gain medium.Two narrow peaks at $k \approx 8$ μm^{-1} are forming to the left and to the right of a gap. Comparing with the transmission spectrum $\mathcal{T}(k)$ from Fig. 4.2, this gap corresponds to the transmission dip. Comparing to Fig. 4.3, the narrow peaks correspond directly to lasing modes with linear gain. Due to the small Thouless number $g = 0.5$, modes are already well separated. But particular modes may be even narrower and much farther apart than the average mode linewidth. Thus, these peaks appear in the emission spectrum in Fig. 4.7(a).

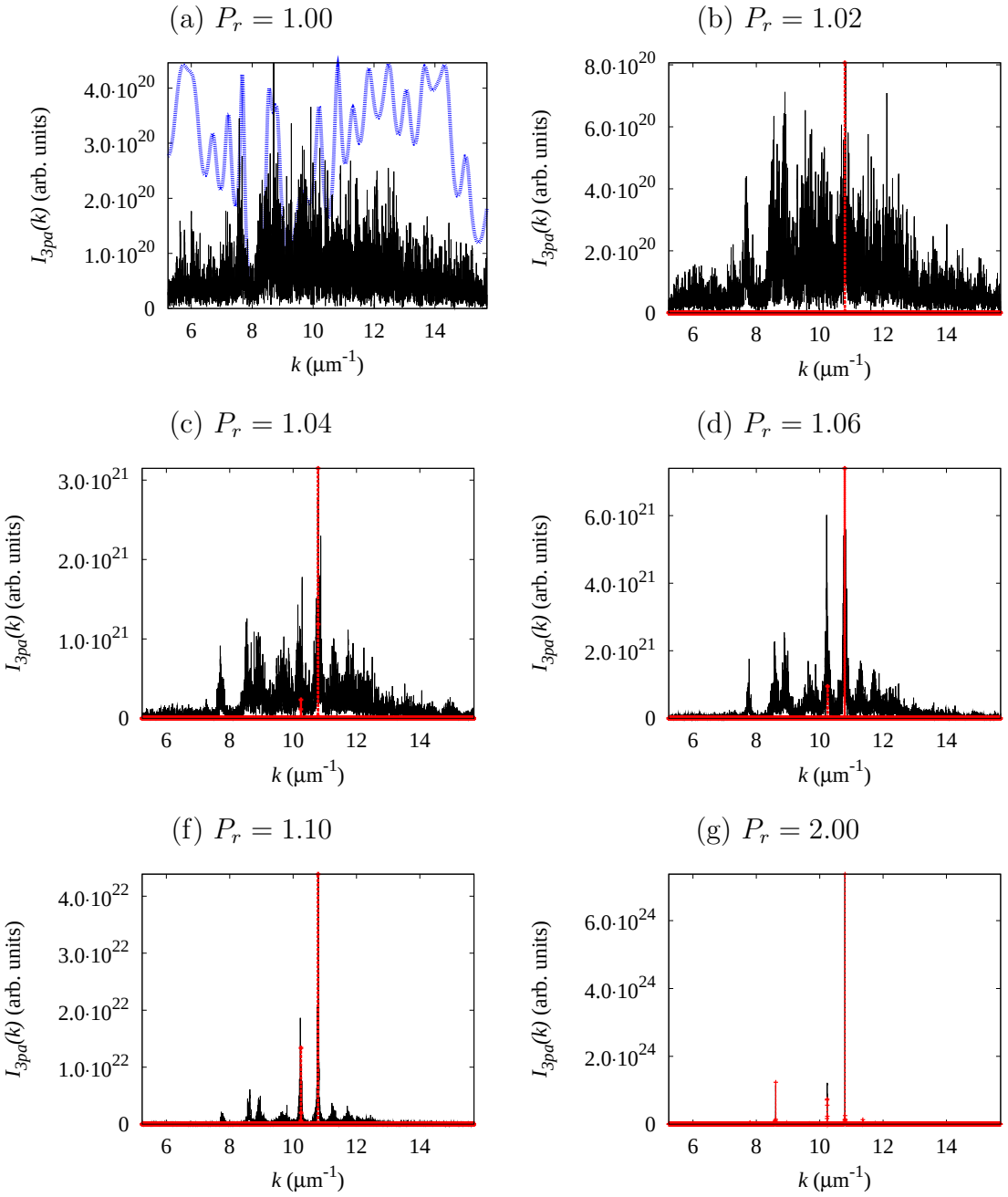

Figure 4.7. Steady-state intensity spectra $I_{3pa}(k)$ comparisons with noise (solid black lines) and without noise (dashed red lines and crosses) for a random system with dielectric layers of $\Delta n = 0.25$. $k_a = 10.5\ \mu\text{m}^{-1}$. (a) No clear lasing peaks, but a broad peak centered around k_a compared with $\mathcal{T}(k)$ (blue dotted line). (b) The broad peak narrows for the case with noise and a single mode begins lasing for the case without noise. (c-g) The spectra for the case with noise slowly starts to resemble the case without noise. (g) A third mode is excited for $P_r = 2.00$.

With only a slight increase of the pumping rate to $P_r = 1.02$ [Fig. 4.7(b)], the broad peak narrows around k_a. Without noise, a single lasing peak appears. This lasing peak corresponds to the mode nearest k_a with the smallest threshold in Fig. 4.3. This peak is a delta function with its "linewidth" merely determined by the integration time of the Fourier transformation. By carefully adjusting P_r, one may force the laser without noise into single-mode operation. However, by including noise, there is not single-mode lasing, as shown below. There is a peak for $P_r = 1.02$ with noise at the same frequency as the case without noise. Based on the study of the dielectric slab laser, peaks may form with linewidths narrowed by ASE. There are clearly other similar peaks at different frequencies for this pumping rate and for larger pumping rates.

For $P_r \geq 1.04$, at least two sharper peaks appear for the case with noise at $k = 10.2$ μm^{-1} and $k = 10.8$ μm^{-1}. These correspond to the two modes nearest k_a in Fig. 4.3. They are at the same frequencies as the lasing peaks without noise. For $P_r = 1.04$ [Fig. 4.7(c)], there are other sharp peaks, e.g., at $k \approx 8$ μm^{-1}, but it is unclear if they are due to lasing action. This trend continues in Fig. 4.7(d) and (f), but the two central peaks begin to dominate the others. For $P_r = 2.00$ [Fig. 4.7(g)], where the total intensity is just beginning to increase linearly with P_r [Fig. 4.5], there are three narrow peaks. The third peak at $k = 8.6$ μm^{-1} corresponds to the low threshold mode at $k = 8.5$ μm^{-1} with linear gain in Fig. 4.3. The spectrum here greatly resembles the case without noise with only small differences in amplitude.

Going back to the transition region between ASE and lasing oscillation, the spectrum for $P_r = 1.10$, smoothed via iterative 3pa (Eq. 3.21), is shown in Fig. 4.8. The two central peaks are preserved even after the intense averaging procedure. The small ripples

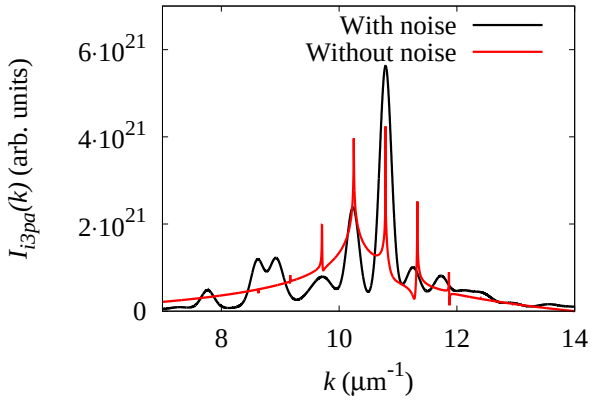

Figure 4.8. Steady-state intensity spectrum iteratively smoothed $I_{i3pa}(k)$ (black line) for a random system with dielectric layers of $\Delta n = 0.25$ and $P_r = 1.10$. The spectrum without noise (red dashed line) is also shown plotted on a log scale to reveal the smaller peaks. Smoothing allows two lasing peaks to become visible at $k = 10.2\ \mu\text{m}^{-1}$ and $k = 10.8\ \mu\text{m}^{-1}$. Data with noise has been smoothed via Eq. 3.21.

neighboring the two central peaks coincide with peaks in the spectrum without noise. The averaging procedure has broadened the peaks. There are also peaks that survived the averaging procedure that do not appear in the spectrum without noise. A peak at $k \lesssim 8\ \mu\text{m}^{-1}$ and two peaks (which may be overlapping) at $k \approx 9\ \mu\text{m}^{-1}$ are clear. These peaks correspond well with the three modes at similar frequencies in Fig. 4.3. It appears that a significant effect of noise for small pumping rates is to excite more modes than would be excited without noise. For higher pumping rates, the spectrum seems to become more similar to the spectrum without noise. It follows that the extra peaks for small pumping rates may only be due to ASE. This shall be studied more thoroughly in the ballistic regime in the next section, where the transition from ASE to clear lasing action occurs over a larger range of pumping rates.

4.3.2. Low Index Contrast

As an example of a random 1D system in the ballistic regime, the indices of refraction of the dielectric layers are $n_1 = 1.05$ and the air gaps $n_2 = 1$. The localization length ξ is calculated following the method in Sec. 1.1.2 and is nearly constant at $\langle \xi \rangle \approx 220$ μm over the wavelength range 500 nm $\leq \lambda \leq$ 750 nm. With $\xi \gg L$, the system is deep in the ballistic regime.

4.3.2.1. Intensity. The average output intensity in the steady-state regime $\langle I \rangle$ is examined as the pumping rate P_r is increased. To avoid numerical problems mentioned earlier, $\langle I \rangle$ is found by a spectral integration via Eq. 4.2. The result in the ballistic regime ($\Delta n = 0.05$) is shown in Fig. 4.9(a) and appears very similar to the result of the dielectric slab in Fig. 3.7(a). Figure 4.9(a) also compares results with and without noise. The two cases are nearly identical, except at large pumping rates where the case with noise exhibits slightly larger intensities. In this region, mode dynamics may be responsible for altering the output intensity. If modes are anti-correlated, then the total output intensity may remain relatively constant. However, if they are correlated, there may be a fluctuation in the output emission. We have found that even a small difference in the initial condition *without* noise, such as a different excitation wavelength λ_0 or excitation width $\delta\lambda_0$, may significantly influence laser dynamics much later in the simulation. It follows that including noise may further alter the dynamics. Thus, there may be slight differences between the cases with and without noise because of the changes caused by stochasticity.

Similar to the dielectric slab case, as P_r increases from zero, the system reaches the transparency point at $P_r = 1$. Increasing P_r further, the lasing threshold is reached

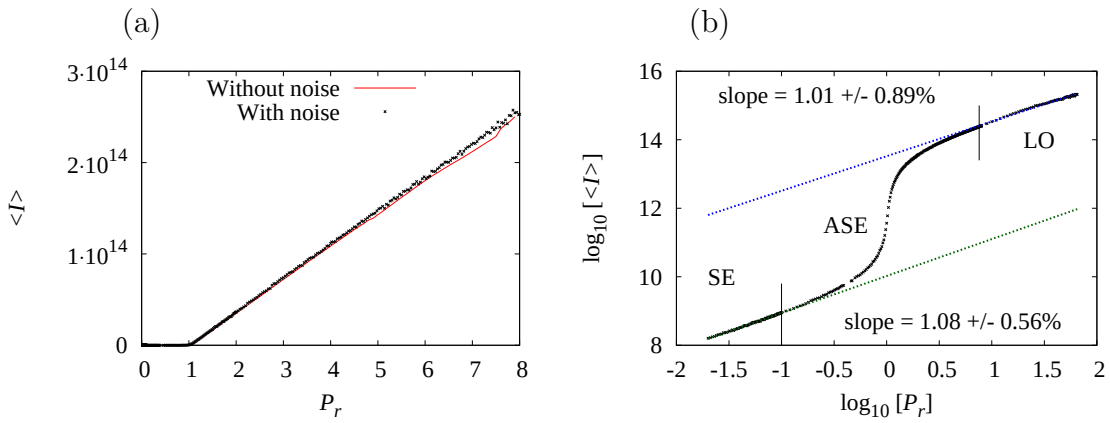

Figure 4.9. Average steady-state intensity $\langle I(k)\rangle$ vs. pumping rate P_r of the random structure with low index contrast $\Delta n = 0.05$, and $\lambda_a = 600$ nm, $\Delta\lambda_a = 10(\Delta\lambda) = 267$ nm. (a) Comparison of steady-state intensity behavior with noise (black points) and without noise (red line). (b) $\langle I(k)\rangle$ with noise is plotted on a $\log_{10}$ scale to easily examine the regions of operation (SE, ASE, LO). Without noise, only the LO region is calculable. Linear fits to the intensity are shown in the SE and LO regions. Vertical black lines delineate where the line fits are taken. Slopes ≈ 1 of lines fitting the intensity show that $\langle I(k)\rangle \propto P_r$. In the ASE region, the intensity increases with a larger-than-linear rate as $(P_r)^p$ $(p > 1)$.

and intensity increases linearly. However, we shall now investigate the region of small pumping rates close to the transparency point. Figure 4.9(b) shows that $\langle I(k)\rangle$ vs. P_r may be separated into 3 distinct regions: spontaneous emission (SE), amplified spontaneous emission (ASE), and lasing oscillation (LO). Far below the transparency point, there is no population inversion. The only emission is spontaneous emission so the output intensity grows linearly with P_r. As the pumping rate increases, so does the population inversion, and the spontaneous emission becomes amplified. However, the gain (even when $\rho_3 > 0$) is less than the leakage loss rate, so there is no lasing oscillation. As seen in Fig. 4.9(b) for $P_r \simeq 1$, the intensity increases as $(P_r)^p$ with $p > 1$. This phenomenon of ASE may often be mistaken for lasing due to output properties resembling the output properties

of a laser, such as a drastic linewidth reduction (as seen for the dielectric slab laser in the previous chapter). Usually, in the case of ASE, the output is mostly influenced by the gain medium and not the laser cavity (as indicated by systems in which there is no laser cavity [**153**]). Some cite this as a distinguishing factor [**154**] between ASE and lasing oscillation. However, from our studies in the previous chapter, we observed spectral narrowing around the modal linewidths due to ASE. Thus, ASE is also influenced by the laser cavity. Furthermore, it was shown [**35**] that one aspect of ASE, the statistics of ASE *spikes* are markedly different than those of lasing peaks. True lasing oscillation manifests in the last region far above the transparency point. Here, there is a enough population inversion to sustain lasing oscillation and the steady-state intensity returns to a linear increase with P_r. The studies in this chapter focus on the transition region between ASE and LO.

To ensure these results are not limited to the particular configuration considered here, simulations with another random seed (to initialize the Γ_i noise terms) and another realization of a random structure (with the same properties) were done. The results were nearly identical. Slight differences only arise due to stochasticity.

4.3.2.2. Spectra. Intensities in the previous section were found by integrating the intensity spectra. The spectra themselves shall be examined here. Intensities behave very similarly for the following cases in that there is always 3 regions of operation (SE, ASE, LO).The steady-state spectra, however, reveal more differences.

First, the spectra for the cases without noise are compared to the passive case. The quasi modes of the passive system were calculated using the transfer matrix method (see Sec. 1.4.4). Figure 4.10 shows the result just above the lasing threshold. For $P_r = 1.06$,

there is single mode lasing with the frequency of the lasing mode pulled toward the maximum of the gain spectrum at $k_a = 10.5\ \mu\text{m}^{-1}$. When gain is introduced, the modes acquire a frequency-dependent phase shift. To understand this so-called frequency pulling, consider a dielectric slab with index n for simplicity. The frequencies of the cold cavity modes $k_{m'}$ are given by Eq. 1.53. A phase shift $\phi_L(k)$ caused by the gain medium, determined by the Lorentzian lineshape, must be added [**155**] yielding a nonlinear equation for the lasing frequency k_m

$$\begin{aligned} k_m + \phi_L(k) =& k_{m'} \\ k_m + \frac{k_m - k_a}{\Delta k_a}\ell_g^{-1}(k_m) =& k_{m'}, \end{aligned} \tag{4.3}$$

where $\ell_g(k)$ is the gain length discussed in Sec. 1.1.2 and depends on P_r as well. If we assume $k_m - k_a$ is small, this term can be replaced with $k_{m'} - k_a$ resulting in a lasing frequency

$$k_m \approx k_{m'} - \frac{k_{m'} - k_a}{\Delta k_a}\ell_g^{-1}(k_{m'}). \tag{4.4}$$

If $k_{m'} > k_a$, k_m is reduced from $k_{m'}$. If $k_{m'} < k_a$, k_m is increased from $k_{m'}$. Thus, the lasing mode frequencies are pulled toward k_a. This effect is seen clearly for $P_r = 1.08$ [Fig. 4.10(b)] where all lasing frequencies are pulled toward k_a.

Concerning the spectra with noise, the three-adjacent-point averaging procedure is used once again to help reduce the influence of ASE spikes. A big difference between the experimental data of Wu and Cao [**35, 36**] and the numerical data presented here, is the spectral spacing and width of lasing peaks. Here, especially far into the ballistic

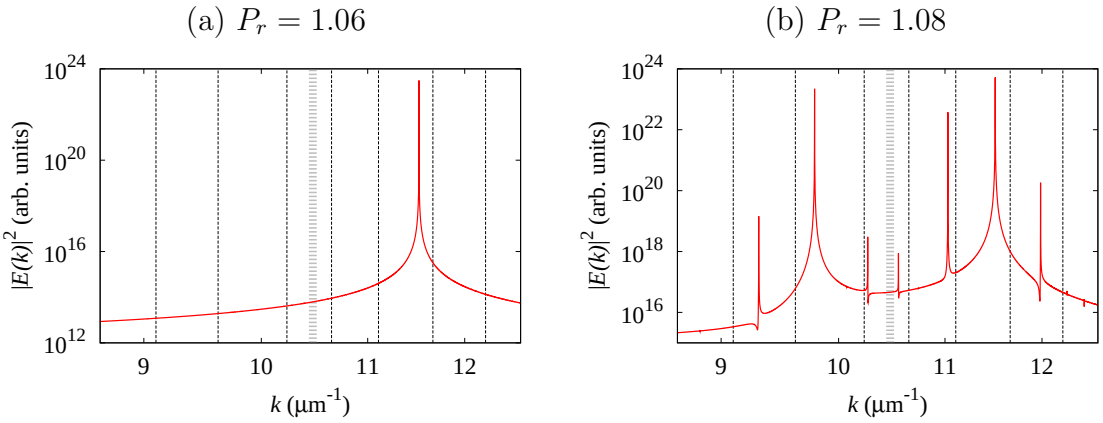

Figure 4.10. Steady-state intensity spectra $|E(k)|^2$ *without* noise (red lines). Vertical dashed lines mark frequency locations of the quasi modes of the passive random system. The vertical dashed gray line marks the gain frequency k_a. (a) Single-mode lasing occurs for $P_r = 1.06$ (just above the lasing threshold). (b) Multimode lasing occurs for $P_r = 1.08$, with lasing frequencies pulled toward k_a in all cases.

regime, we are able to study the lasing peaks as they form with increasing P_r. During this formation, the peaks are quite broad (1–10 nm), compared to the narrow ASE spikes (0.06–0.08 nm). Thus, even after executing the three-adjacent-point averaging procedure above, the ASE spikes remain as sharp modulations. This makes it somewhat difficult to clearly determine the lasing peaks, especially if they are close together. On average, the Thouless number is 1, but particular lasing modes may be much closer together than the average lasing linewidth. If an *iterative* 3pa procedure (Eq. 3.21) is implemented, it is possible to average out the ASE spikes enough to see the formation of peaks. However, choosing the number of iterations is extremely subjective. For this random laser with a relatively large Thouless number, the frequencies of lasing modes are not known as precisely as in the dielectric slab laser. Too few iterations results in some remnants of the

ASE spikes which could be mistaken for lasing peaks. Too many iterations can result in averaging out the lasing peaks themselves.

Output intensity is observed to reach a fairly steady state at least by a simulation time of $t = 16.6$ ps no matter the pumping rate. This was proven by comparing $\langle I(k) \rangle$ taken from Fourier transformations over different temporal ranges up to $t = 267$ ps. Spectra obtained from the range 16.6 ps – 33.2 ps were found to be sufficient.

Figure 4.11 shows the steady-state spectra with noise $I_{3pa}(k)$ for increasing pumping rates. Similar to the data shown in Fig. 4.7, a broad ASE peak is revealed in Fig. 4.11. The spectrum is fairly flat for $P_r < 1$, while for $P_r = 1.00$, the broad peak is centered around $k_a = 10.5\ \mu\text{m}^{-1}$ with a width roughly equal to the atomic linewidth $\Delta k_a = 4.7\ \mu\text{m}^{-1}$. Different from Fig. 4.7, the broad peak narrows in Figs. 4.11(a-d) without smaller peaks rising up. The difference between the data with low index contrast and the high index contrast is very similar experimental results [**156**]. By increasing the density of particles, Cao *et al.* observed the transition from ASE to clear lasing action. Increasing the index contrast Δn is analogous to increasing the density of scattering particles. However, a large enough pumping rate will stimulate lasing action even with low index contrast.

Without noise, a single lasing peak appears for $P_r = 1.06$ [Fig. 4.10(a)]. There is clearly not single-mode lasing in the case with noise for $P_r = 1.06$ [Fig. 4.11(f)]. There is a discernible peak at the same frequency as the lasing mode without noise, but this is due to ASE as suggested by the intensity behavior in Fig. 4.9 (modal intensities themselves will be compared below). Without noise, multimode lasing occurs for $P_r = 1.08$ [Fig. 4.10(b)].

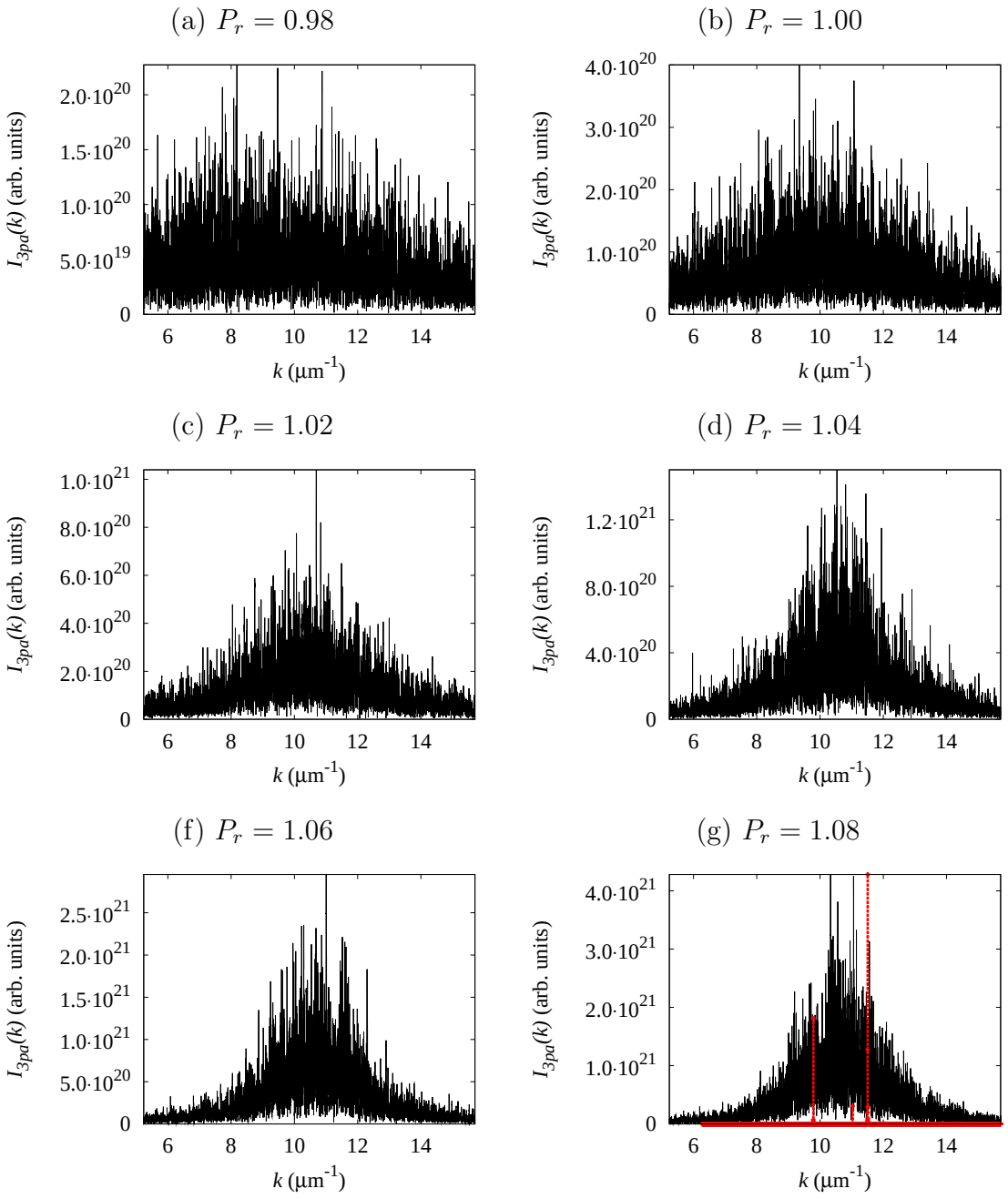

Figure 4.11. Steady-state intensity spectra $I_{3pa}(k)$ in the ASE region. (a) The spectrum is fairly flat for $P_r < 1$. (b) A broad peak begins to form for $P_r = 1$ and (c-d) the peak narrows as P_r increases further. (f) Due to ASE, narrower peaks begin forming amidst the broad background. Without noise, $P_r = 1.06$ yields single-mode lasing [Fig. 4.10(a)]. (g) More small peaks due to ASE become clear, where, without noise (dashed red lines and crosses), multi-mode lasing clearly occurs.

With noise [Fig. 4.11(g)], more small ASE peaks appear corresponding to the frequencies of the case without noise (more discernible when the two spectra are overlayed).

Figure 4.12(a-d) shows that the ASE peaks become sharper and well separated for larger pumping rates. By $P_r = 1.74$ [Fig. 4.12(f)] and $P_r = 2.00$ [Fig. 4.12(g)], there are six significant peaks. These six frequencies have a one-to-one correspondence with the quasi modes of the passive system and the linewidths are sufficiently narrow to separate the modes. This behavior is similar to that found in the dielectric slab. The big difference is that this random laser is operating in the multimode regime due to the leakiness of this random system.

The spectrum for $P_r = 2.00$ in Fig. 4.12(g) is iteratively smoothed via Eq. 3.21. The result is compared to the spectrum without noise in Fig. 4.13. $I_{i3pa}(k)$ reveals six major peaks, enumerated 1–6, not destroyed by the smoothing process. In Fig. 4.13, all peaks except peak 1, coincide with significant peaks in the spectrum without noise (peak 1 corresponds to a very small peak not visible). Without noise, mode 5 reached the lasing threshold first at $P_r = 1.06$. The remaining modes soon followed at $P_r = 1.08$. Though precise thresholds are unknown with noise, they are certainly larger than the case without noise. So as expected, noise has increased the lasing threshold of modes. All six frequencies can be traced back into the ASE regime to at least $P_r = 1.22$. Decreasing the pumping rate broadens the linewidth of each of the six peaks. Thus, Figs. 4.11 and 4.12 are a clear and explicit revelation of the general behavior of ASE for a random system in the ballistic regime (in 1D).

Note that the two modes closest to k_a in Fig. 4.4 appear to be "combined" in Fig. 4.12. Iterative smoothing does destroy any individual character these two modes might

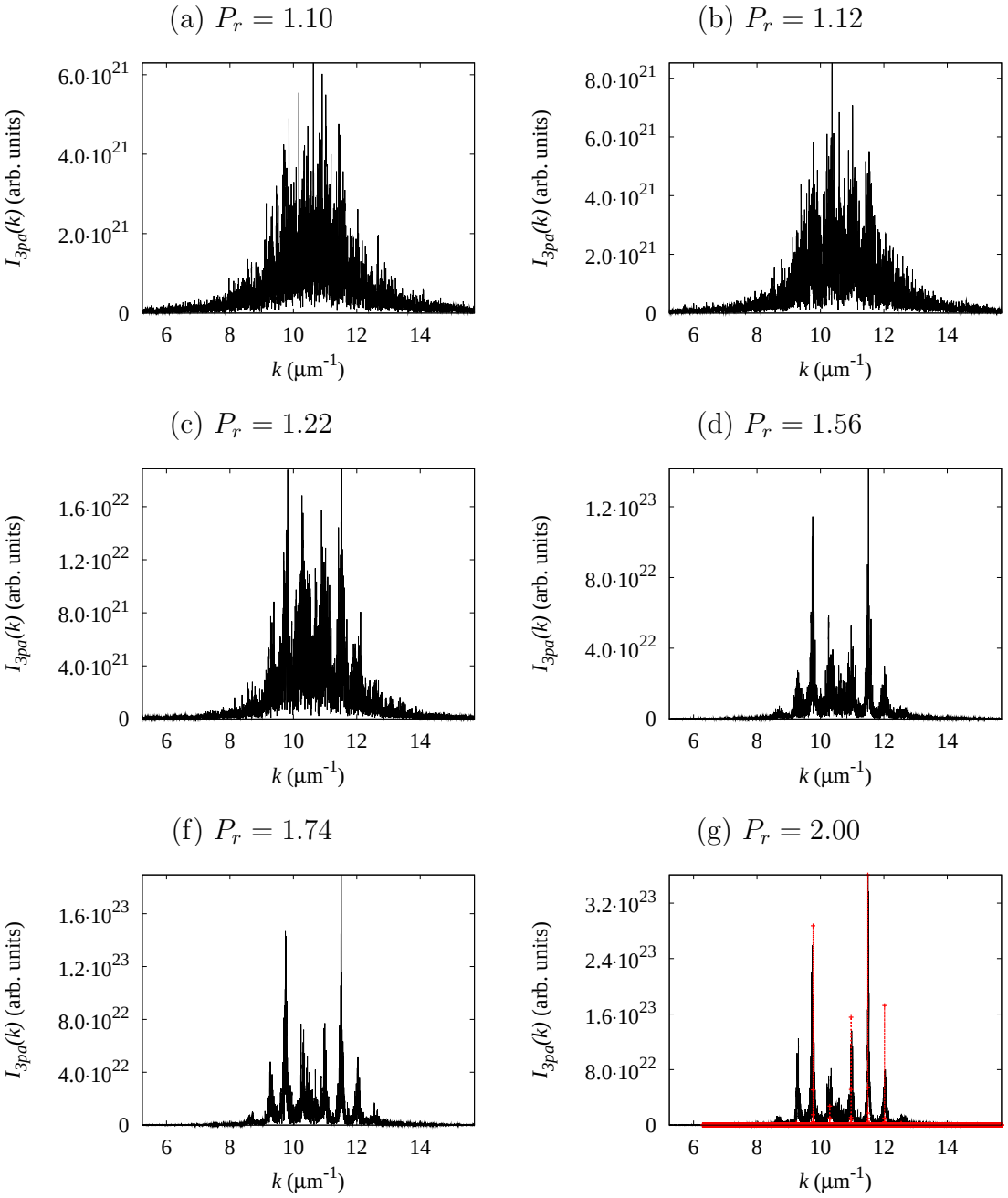

Figure 4.12. Steady-state intensity spectra $I_{3pa}(k)$ for increasing P_r as lasing with resonant feedback finally manifests. (a-d) ASE causes narrowing of modal linewidths. (f-g) Due to the fuzziness of the lasing threshold, it is difficult to determine the exact threshold for lasing action. But the narrow peaks in (g) coincide with the lasing peaks without noise (dashed red lines and crosses).

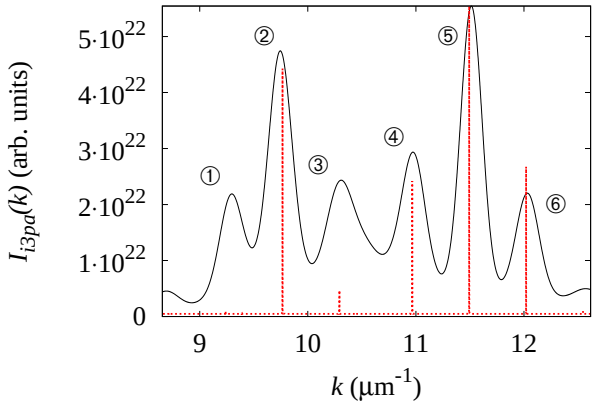

Figure 4.13. Steady-state intensity spectrum iteratively averaged $I_{i3pa}(k)$ compared to the spectrum without noise for a random system with dielectric layers of $\Delta n = 0.05$ and $P_r = 2.00$. The major peaks are enumerated 1–6. All peaks but peak 1 have a corresponding peak in the spectrum without noise, as expected from Fig. 4.15(d).

have, but as shown in Fig. 4.13, only a "composite" peak appears (labeled peak 3). A likely explanation is that a combination of frequency pulling and linewidth broadening due to noise brought these two modes so close together that they appear to be merged. This may also be a result of time averaging, which shall be discussed later.

As the pumping rate increases drastically in Fig. 4.14, the linewidths decrease drastically. Figures 4.14(a) and (b) are perhaps most similar to the experimental results presented in [**36**]. According to experiments, the lasing peaks have a larger spectral width than the ASE spikes, but only twice as large. As we have observed, however, ASE also generates wide peaks around modal frequencies. Thus, in this range of pumping rates, using the smoothed spectrum $I_{3pa}(k)$ does not necessarily make it straightforward to distinguish ASE from lasing action. Only when the spectra are compared with other quantities, such as mode statistics or mode intensities (as will be shown below), can the peaks in this regime be confidently contributed to lasing action.

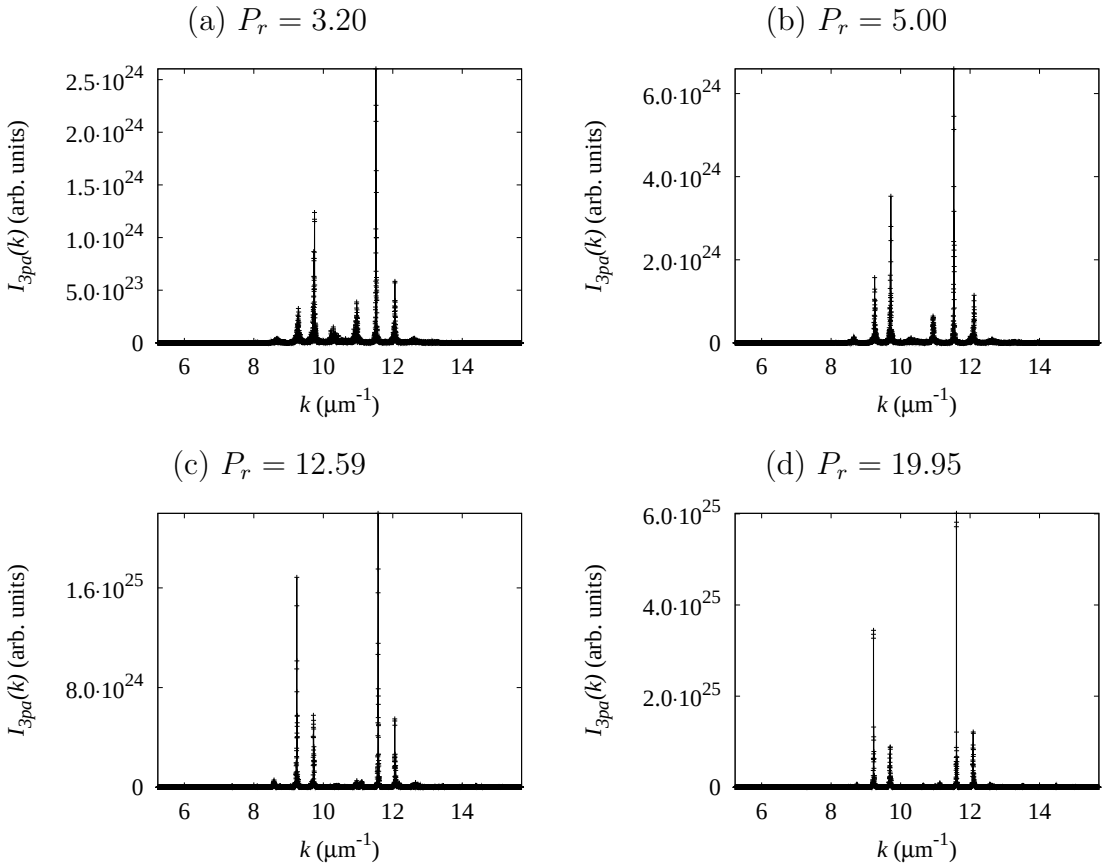

Figure 4.14. Steady-state intensity spectra $I_{3pa}(k)$ for large P_r with clear lasing action. (a-b) There is enough spectral resolution that linewidths may be estimated fairly accurately. (c) There is enough data above the FWHM of the lasing peaks to obtain a rough estimate of the linewidth, but this should not be quantitatively compared to linewidths obtained with smaller P_r. (d) The two largest lasing peaks have a linewidth equal to or smaller than the spectral resolution.

Once the pumping rate has been increased enough, even the lasing peak width becomes narrower than the spectral resolution, just like ASE spikes. The data for $P_r = 12.59$ [Fig. 4.14(c)] provides a rough estimate of the linewidth, but the spectral resolution is too poor once $P_r = 19.95$ [Fig.4.14(d)]. Furthermore, for these large pumping rates, the amplitude of the peaks (relative to neighboring peaks) in the center of the spectrum reduce. This

is most likely due to lasing mode interaction due to spatial hole burning [**45**]. Nonlinear interaction increases for larger pumping rates and the modes which lase first tend to dominate other modes.

The spectra with noise are directly compared to the spectra without noise in Fig. 4.15. From this comparison, it is easier to distinguish the ASE peak for $P_r = 1.06$ [Fig. 4.15(a)] in the case with noise. The width of this ASE peak is $\gtrsim 0.5\ \mu\text{m}^{-1}$. It is consistently present for larger pumping rates and the linewidth decreases monotonically until lasing action begins.

For $P_r = 1.08$ [Fig. 4.15(b)], there are multiple lasing peaks for the case without noise. There is some correspondence to ASE peaks in the spectrum with noise. For $P_r = 1.22$ [Fig. 4.15(c)], there is a large peak in the case with noise at $k \approx 10.3\ \mu\text{m}^{-1}$. There is a corresponding peak in the spectrum without noise, but that peak is orders of magnitude smaller than the neighboring peaks.

For $P_r = 3.20$ [Fig. 4.15(f)] and $P_r = 5.00$ [Fig. 4.15(g)], the relative amplitude of peak 1 with noise decreases while the amplitude of the peak without noise increases. The landscape of population inversion is different without noise. So although the effects of noise on the population inversion decrease with an increased pumping rate, it is not surprising the amplitudes of modes is different in the two cases.

4.3.2.3. Linewidths. In this section, spectral widths shall be compared from the simulations in the ballistic regime. The three widths compared are: (i) width of the broad background peak $\delta\lambda_B$ (associated with ASE for small P_r), (ii) linewidth of mode 2 $\delta\lambda_2$, and (iii) linewidth of mode 5 $\delta\lambda_5$. Modes are enumerated in Fig. 4.13. All widths are calculated using the method developed in Sec. 3.3.2.

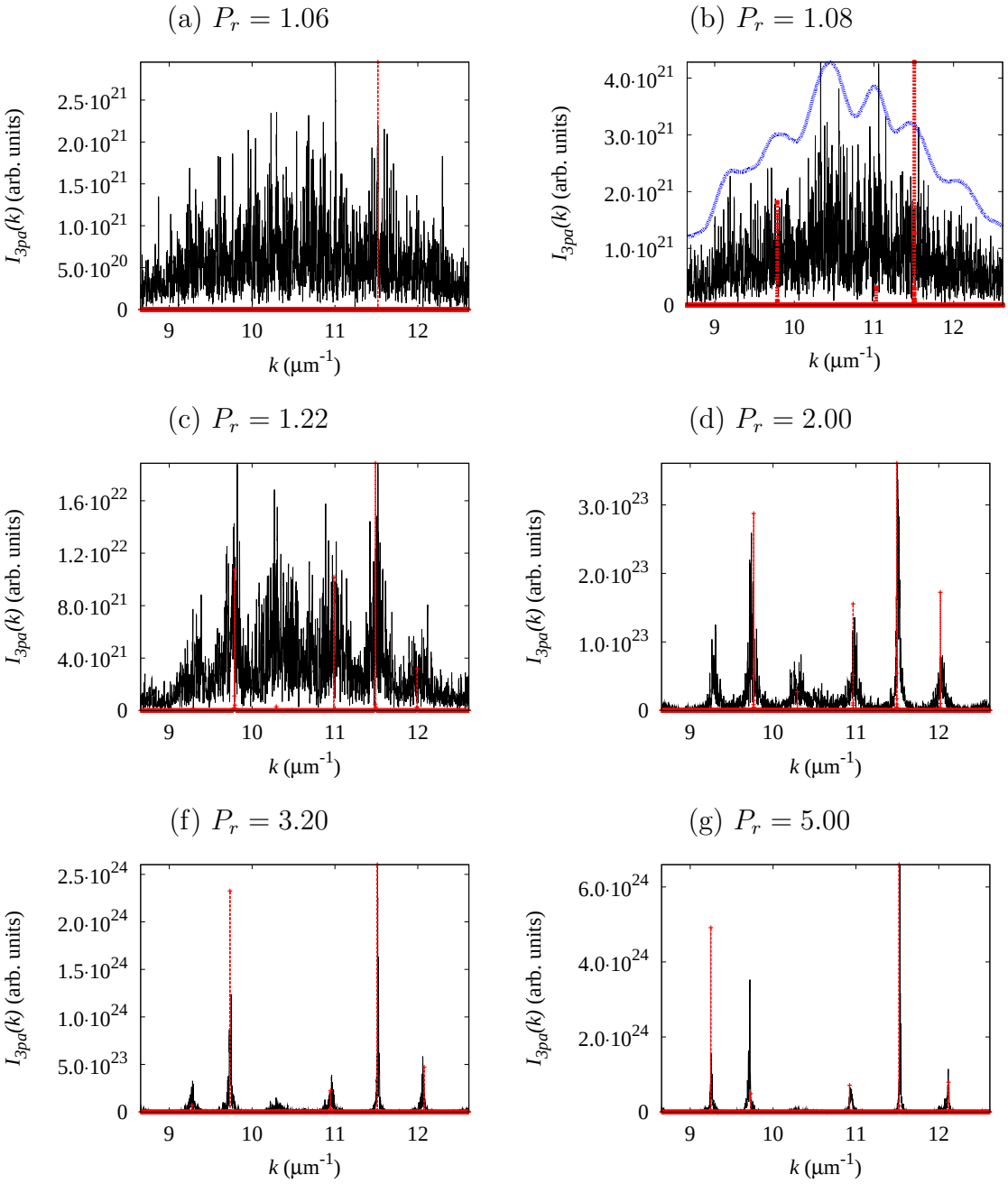

Figure 4.15. Steady-state intensity spectra $I_{3pa}(k)$ comparisons with noise (solid black lines) and without noise (dashed red lines and crosses) for a random system with $\Delta n = 0.05$. (a) The frequency of an ASE peak in the spectrum with noise (mode 5) corresponds to the single-mode lasing frequency without noise. (b) ASE peaks become more evident as indicated by $I_{i3pa}(k)$ (dotted blue line). (c-f) Spectra with and without noise become more similar. (g) Mode amplitudes are different with and without noise. This is not surprising due to the effect of noise on the population inversion.

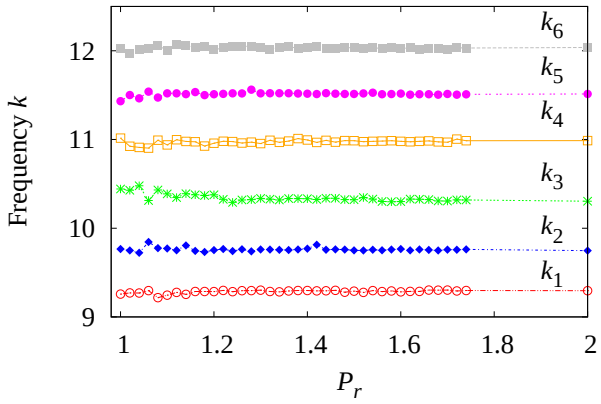

Figure 4.16. Mode frequencies vs. pumping rate for the random structure with index contrast $\Delta n = 0.05$ and $k_a = 10.5\ \mu\text{m}^{-1}$. For small pumping rates the center frequencies of modes are unclear due to noise. As peaks emerge from the background spectrum, the frequencies do not shift much as the pumping rate increases over this small range.

The calculation of $\delta\lambda_B$ is done by fixing the wavelength range to 400 nm $< \lambda <$ 1200 nm. This is the range over which the spectral integration is carried out via Eq. 3.17 to obtain the Lorentz error function $L_{EF}(k)$. The center frequency k_0, usually a fitting parameter, is fixed. In the ASE region, the center of this broad peak should have a maximum at k_a. As lasing oscillations begin, we wish to observe the narrowing of the background spectrum around k_a in the range 400 nm $< \lambda <$ 1200 nm. Thus, even after lasing oscillation begins, k_0 is fixed at k_a and not adjusted during fitting. Because the background is not a constant value, the fitting equation is Eq. 3.17.

The calculations of $\delta\lambda_2$ and $\delta\lambda_5$ are done by choosing a frequency range based on the smoothed spectrum $I_{i3pa}(k)$ in Fig. 4.13. The troughs on either side of the peaks of modes 2 and 5 are chosen as the low and high frequency limits even for values of P_r different from that in Fig. 4.13. From the progression of the spectra with increasing P_r,

the frequencies at the maxima of these two modes do not change significantly, so this frequency range should be a valid choice. This is evidenced by frequency behavior with respect to pumping rate shown in Fig. 4.16. For each P_r value, the peak maximum of each mode is located by finding the maximum of $I_{i3pa}(k)$ within that frequency range. This value serves as the initial guess for the k_0 fitting parameter, which is then allowed to be adjusted during fitting [**136**], along with A_l and s, to obtain the best fit. The method suggested in Sec. 3.3.2, of using a background constant as a fitting parameter over a narrower range of frequencies, was experimented with. However, the frequency range was too restrictive containing little data, resulting in poor fits which even diverged for some values of P_r. Thus, the entire frequency range from trough to trough is considered for all fits and the fitting equation remains Eq. 3.17. For pumping rates near 1.00 in Fig. 4.16, the center frequencies of modes are unclear due to noise. Note that even for these small pumping rates, mode frequencies have already been pulled toward $k_a = 10.5\ \mu\text{m}^{-1}$ by the gain medium. As the pumping rate increases and peaks emerge from the background spectrum, the frequencies do not shift much. According to Eq. 4.3, this indicates a fairly weak dependence of ℓ_g on P_r values within this range.

Figure 4.9 shows that significant change in $\langle I(k) \rangle$ occurs for $1 < P_r < 10$. Figure 4.17 expands this range and also separates the total intensity into modal intensities through spectral integrations over the modes alone. Note that except for mode 1, perhaps, all modes exhibit very similar behavior. Thus, they all appear to reach their lasing thresholds at approximately the same pumping rate, whatever that may be. Without noise, modes reached their respective lasing thresholds for roughly the same pumping rate $P_r = 1.08$ [Fig. 4.10(b)]. Thus, it is not surprising that the modes begin lasing near the same

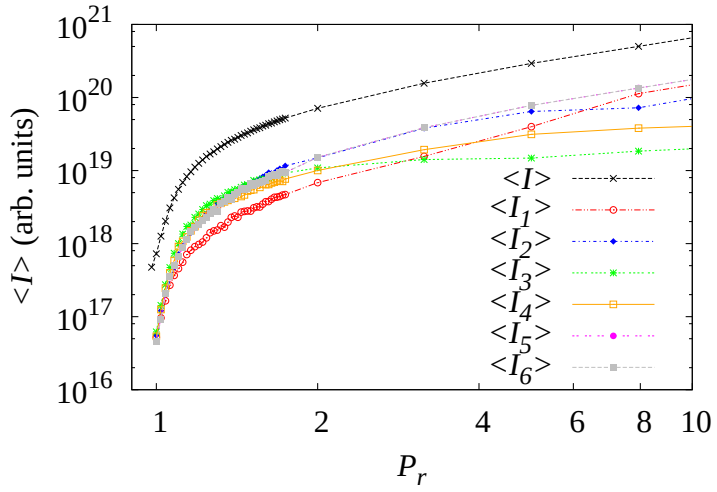

Figure 4.17. Average steady-state intensity $\langle I(k)\rangle$ and modal intensities $\langle I_j\rangle$ vs. pumping rate P_r of the weakly scattering random structure with $\Delta n = 0.05$, $\lambda_a = 600$ nm and $\Delta\lambda_a = 10(\Delta\lambda) = 267$ nm. In the ASE region, $P_r \gtrsim 1$, intensity increases with a super-linear rate while in the LO region, intensity returns to a linear increase with P_r.

pumping rate with noise. Furthermore, it may be suggested that noise has blurred the thresholds of all modes somewhat, putting them even closer to each other.

In any case, the resulting spectral widths are shown in Fig. 4.18 along with corresponding steady-state intensities. As P_r increases from 0.98 to 1.22 in Fig. 4.18(a), $\delta\lambda_B$ decreases by an order of magnitude. This is consistent with experiments [**156**] which show a decrease by a factor of roughly four. The precise factor is determined by the gain material. The mechanism behind this drastic narrowing was discussed in Sec. 1.2.1. For $1.22 \leq P_r \leq 1.74$, $\delta\lambda_B$ remains fairly constant with the absolute minimum at $P_r = 1.56$. From Fig. 4.12, this is the pumping region where peaks begin to clearly emerge out of the broad background. The individual peak amplitudes increase, but the peak amplitudes relative to each other stay relatively the same. Thus, $\delta\lambda_B$ stays relatively constant. For

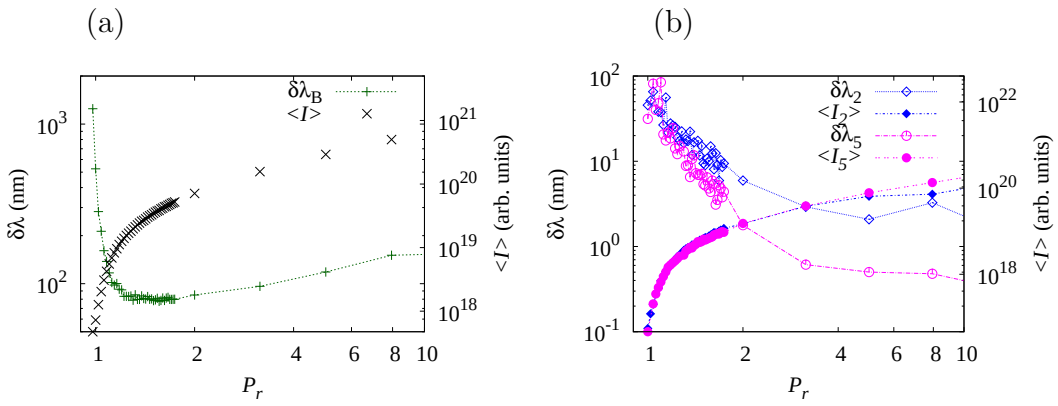

Figure 4.18. Spectral width of (a) the broad peak $\delta\lambda_B$, (b) linewidths $\delta\lambda_2$ and $\delta\lambda_5$ of lasing modes 2 and 5 [see Fig. 4.13(g) for enumeration] vs. P_r. $\delta\lambda_B$ decreases dramatically by an order of magnitude after transparency is reached at $P_r = 1$. The decrease of $\delta\lambda_B$ slows as $\langle I(k)\rangle$ leaves the ASE region and moves into the LO region. $\delta\lambda_B$ flattens by $P_r = 1.22$, reaches its minimum value at $P_r = 1.56$, and slowly increases for larger P_r. This increase is due to modes further away from k_a beginning to lase [e.g., see Fig. 4.14]. (b) The lasing modes themselves have a narrower linewidth which also decreases dramatically for increasing P_r. The linewidth of the dominant lasing mode $\delta\lambda_5$ decreases the most quickly of all calculated lasing modes. Both lasing mode linewidths continue to reduce until spectral resolution is reached for $P_r > 5.00$.

$P_r \geq 2.00$, the outlying modes begin to dominate the lasing modes nearest k_a. Thus, $\delta\lambda_B$ increases.

The mode linewidths $\delta\lambda_2$ and $\delta\lambda_5$ in Fig. 4.18(b) are ill-defined for $1 \leq P_r < 1.06$. This is expected due to the large mode overlap for small P_r. Thus, the linewidths fluctuate and may not be considered as genuine linewidths. As P_r increases from 1.06 to 2.00, the linewidths decrease by an order of magnitude. Most of this narrowing appears to be due to ASE. The peak of lasing mode 5 narrows the most dramatically. This is consistent with all previous figures which show mode 5 to have the largest amplitude. Though all the lasing thresholds are very close and noise introduces fuzziness to the thresholds, mode

5 may technically lase first (as in the noiseless case). As P_r increases past 2.00, the rate of the linewidths' decrease slows. However, the rate of the modal intensity's increase also slows. Flattening of $\delta\lambda_2$ and $\delta\lambda_5$ occurs in the LO regime. However, as discussed below, the last three data points should be ignored due to poor spectral resolution. Physically, the gain will eventually be saturated for large values of P_r and the output intensity and linewidths will genuinely flatten with respect to P_r.

Gordon *et al.* calculated [**11**] the spectral extent of the energy distribution, or linewidth, of a nearly monochromatic beam emitted from a maser. By analogy, Schawlow and Townes calculated [**12**] the linewidth of a laser mode, considering that spontaneous emission broadens the peak. Though the modes in this random laser are not truly lasing until larger intensities are reached, the width of the peaks are still determined by spontaneous emission. Thus, we assume the Schawlow-Townes prediction of linewidth behavior to still be accurate. They found the linewidth to depend on frequency, the width of the corresponding cold cavity resonance, and the field power. In this thesis, the linewidth shall not be quantitatively compared with the Schawlow-Townes prediction (which actually requires correction [**157, 158**]), but the dependence on power (or equivalently, intensity) is easily obtained. The behavior of linewidth with respect to intensity is predicted to follow $\delta\lambda \propto \langle I \rangle^{-1}$.

Figure 4.19 shows $\delta\lambda_2$ and $\delta\lambda_5$ vs. the steady-state intensities of mode 2 $\langle I_2(k) \rangle$ and mode 5 $\langle I_5(k) \rangle$. A linear fit of the data on a log-log scale reveals if the linewidth does decay as a power law and, if so, what the exponent of the decay is. According to the relation of linewidth and intensity above, the slope is expected is expected to be -1.

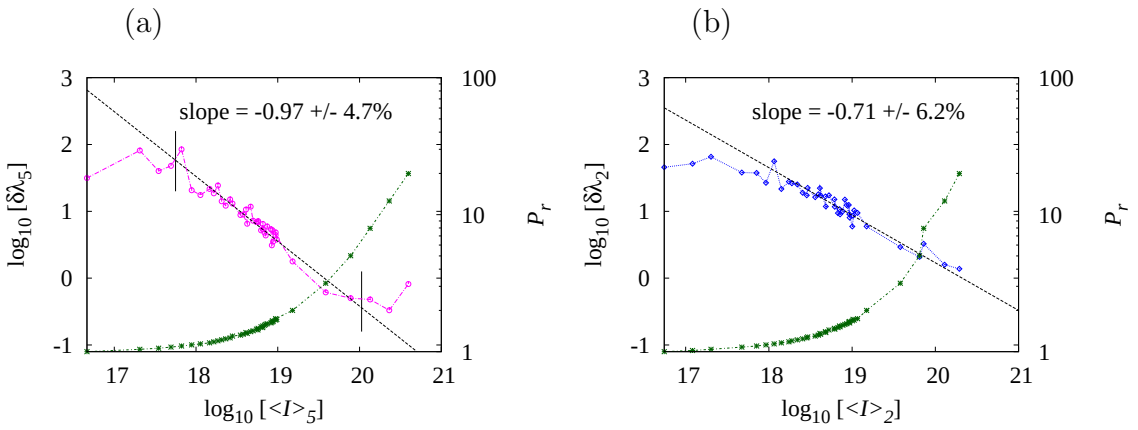

Figure 4.19. Linewidths (a) $\delta\lambda_5$ and (b) $\delta\lambda_2$ of lasing modes 5 and 2 and pumping rate P_r (green asterisks) vs. the steady-state modal intensities $\langle I_5(k)\rangle$ and $\langle I_2(k)\rangle$ for a random system with $\Delta n = 0.05$. (a) The slope ≈ -1 of the fit, means that $\delta\lambda_5 \propto \langle I_5(k)\rangle^{-1}$, the linewidth trend found by Schawlow and Townes. Vertical black lines mark the fitting range. (b) The slope of $\delta\lambda_2$ is shallower than the slope of $\delta\lambda_5$ (> -1).

The smallest value of $\langle I_5(k)\rangle$ for the fitting range for $\delta\lambda_5$ was determined by the pumping rate at which this mode began to lase without noise ($P_r = 1.06$). This pumping rate is also when separate ASE peaks emerge. The largest value of $\langle I_5(k)\rangle$ for the fitting range was determined by the pumping rate at which an accurate estimate of the linewidth is no longer possible due to spectral resolution [see Fig. 4.14]. Data for $P_r > 5.00$, or the last three data points, are neglected.

The fit reveals $\delta\lambda_5$ follows the Schawlow-Townes linewidth trend almost exactly. The slope is -0.97 with an asymptotic standard error of 4.7%. The trend of $\delta\lambda_2$, however, is shallower than the predicted Schawlow-Townes values with a slope of -0.71 and an error of 6.2%. This is not too surprising, as multimode operation is known to affect lasing linewidths [**159, 160**]. A more quantitative investigation shall be carried out in the future.

4.3.3. Low Index Contrast–Nonuniform Gain Distribution

As indicated by recent experiments [**30, 33**] and explored through numerical studies [**47**], it is easier to obtain discrete lasing peaks by locally pumping the system. If the unpumped region of gain consists of three-level or four-level atoms in their ground state, photons leaving the pumped region will not be absorbed or stimulate radiation for the most part. Thus, partial pumping can be modeled as a spatially nonuniform gain distribution. To simulate a spatially nonuniform gain region with the Maxwell-Bloch equations, two-level atoms are placed only in the region $0 \leq x \leq l_G$, where $x = 0$ is the left edge of the structure and $x = l_G$ specifies the right edge of the gain region.

The number of lasing peaks which exist for a system with nonuniform gain shall be compared to the number of lasing peaks for the uniform gain case studied in the previous section. From our observations, noise only seems to increase lasing thresholds. The precise factor of increase is currently unavailable, unfortunately. However, ASE was seen to impart energy to modes irrespective of lasing thresholds [e.g., see Fig. 4.11(g)]. This may give some advantage to modes which would not lase without noise and decrease their relative (to neighboring modes) lasing thresholds. Thus, the threshold increase factor may not be the same for all modes. If noise increases smaller thresholds more than larger thresholds, it could result in more modes lasing simultaneously. This would effectively remove the advantage due to partial pumping. Thus, it is important to check the number of modes with partial pumping when noise is included.

Figure 4.20 compares spectra with and without noise for $l_G = 2140$ nm $\approx L/3$ as P_r increases. With a smaller gain region, the thresholds of lasing modes increase as expected [**161, 32**]. The first mode begins lasing at $P_r = 1.10$ [4.20(a)], whereas the first mode

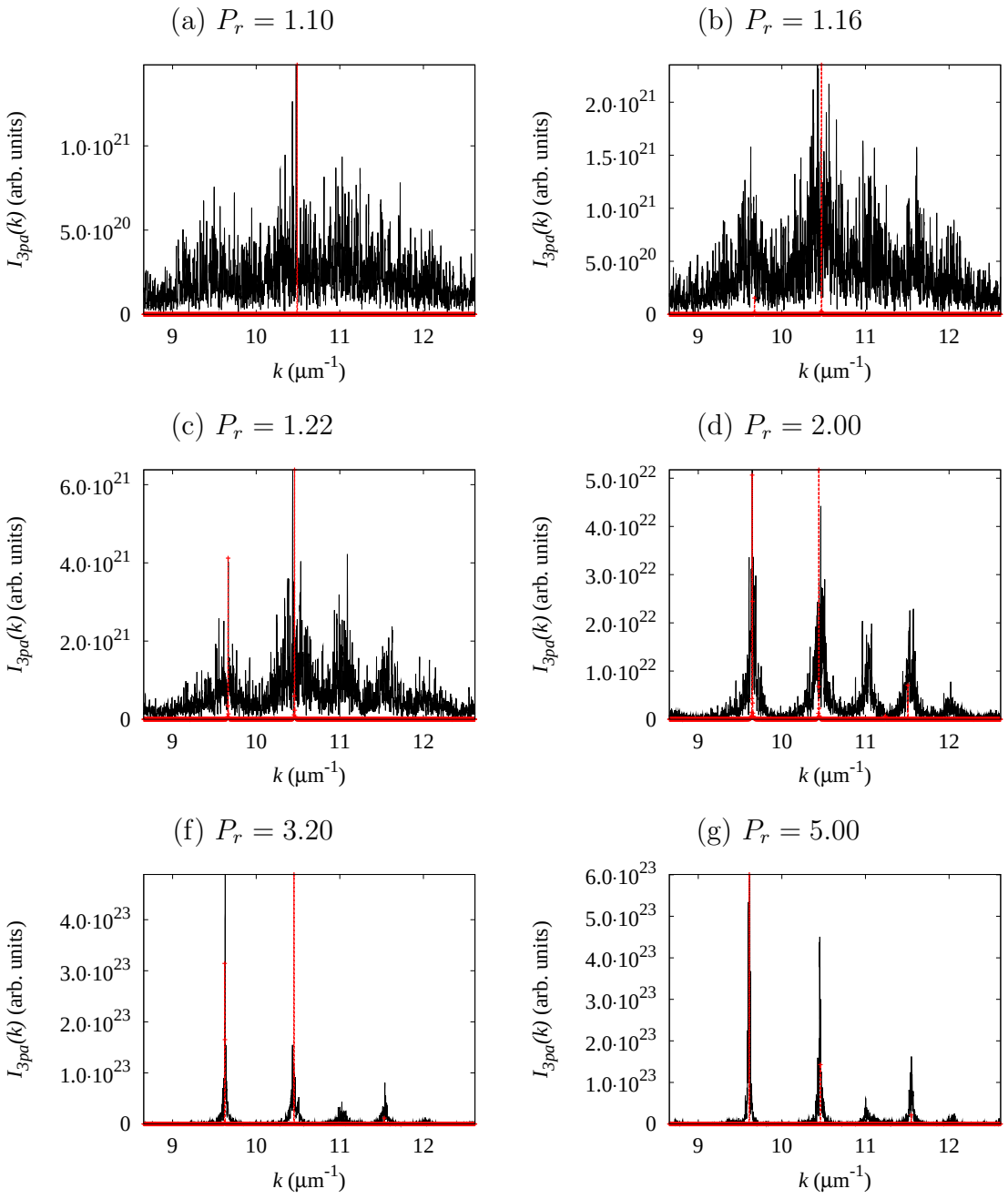

Figure 4.20. Steady-state intensity spectra $I_{3pa}(k)$ comparisons with noise (solid black lines) and without noise (dashed red lines and crosses). (a) With the aid of the spectrum without noise, a small peak in the spectrum with noise (at $k \lesssim 10.5\ \mu\text{m}^{-1}$) can be detected. (b) The narrow peaks now become more evident at this larger pumping rate for the case with noise. (c-g) As P_r increases further, the spectra with noise more closely resembles that without noise The number of modes is less than the case with uniform gain and the modes lasing are more separated in frequency.

began lasing at $P_r = 1.06$ for a spatially uniform gain region. Thresholds of other lasing modes also increase, as evidenced by the single-mode lasing behavior until $P_r = 1.16$ [4.20(b)]. This single mode corresponds to the lasing mode nearest k_a for $l_G/L = 1/3$ in Fig. 4.4(b). With larger values of P_r, it is again easier to distinguish the narrow peaks. For $P_r = 1.22$ [4.20(c)], there are two major peaks without noise, but four major peaks with noise. For $P_r = 2.00$ [4.20(d)], the four major peaks with noise remain, and a third peak arises in the spectrum without noise. The four major peaks become stronger as P_r increases to 3.20 [4.20(f)] and then 5.00 [4.20(g)]. The peak frequencies correspond well to the four central (around k_a) lasing modes found via linear gain shown in Fig. 4.4(b). Since the first lasing threshold is reached for similar values in the uniform and nonuniform gain cases ($P_r = 1.06$ and $P_r = 1.10$), we may compare spectra at the same pumping rates for both cases. There are more peaks with noise than without noise in the nonuniform gain case. However, for $P_r = 5.00$, the number of lasing peaks for a nonuniform gain region is smaller (four) than for a uniform gain region (five) and the frequencies are more separated. Thus, even with noise, the modes with very large lasing thresholds do not appear for the pumping rates considered here and the remaining modes are well separated in frequency. The precise influence, if any, of the large threshold modes should be ascertained in future studies.

4.4. Discussion

For three different cases (Secs. 4.3.1, 4.3.2, and 4.3.3), it has been observed that lasing thresholds are higher with noise than without noise. Changes due to noise near the localization regime are less significant than changes due to noise in the ballistic regime.

The higher index contrast traps light more efficiently resulting in a lower lasing threshold, weakening the influence of ASE. Thus, there is less of a transition region between ASE and LO and the thresholds do not shift as much. In the ballistic regime, with uniform or nonuniform gain, the thresholds experience more increase due to noise. Otherwise, the behavior is similar to the noiseless case.

Before discussing the results of this chapter, other influences on lasing behavior need to be addressed briefly. Dynamical processes [**162**] and/or noise may affect the output intensity so that a true steady state is never reached (e.g., [**163**]). If mode amplitudes are small enough, noise may stimulate random switching between the modes in time [**164, 165**]. It is conceivable here, that noise may cause mode switching and that different modes lase at different times. If the Fourier transformation is taken over a longer time than the time between mode switches, all peaks will appear in the spectrum. An estimate of the time one of the lasing modes spends "turned off" can be calculated using first-passage-time analysis [**166**]. Knowing this information would allow us to precisely determine the time scale on which to compare different Fourier transformations. However, obtaining this estimate requires mode coupling information which is not readily available in our model. Nevertheless, two spectra taken at subsequent time intervals as an example and are compared in Fig. 4.21. These spectra correspond to the system studied in Sec. 4.3.2. The intervals were kept as short as possible (keeping an adequate spectral resolution) to increase the likelihood of finding spectra with different landscapes.

There are some differences between the two spectra in Fig. 4.21. Other than small quantitative changes, the outlying modes, 1, 2, 5, and 6 are qualitatively the same for both intervals. This is to be expected and verifies that noise does indeed quantitatively

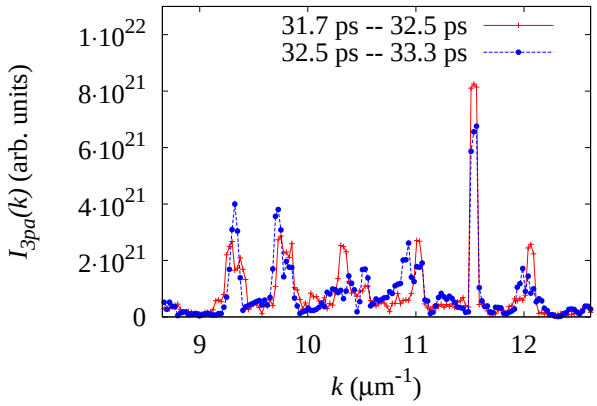

Figure 4.21. Intensity spectra $|E(k)|^2$ taken from two subsequent time intervals: 31.7 ps – 32.5 ps (red crosses) and 32.5 ps – 33.3 ps (blue circles). These times are well after a "steady" state has been reached at $t = 16.7$ ps. A uniform gain region is used in this system which is in the ballistic regime.

influence dynamics of modes with large amplitudes. However, the qualitative character of the two spectra is different for the two central peaks with the lowest amplitudes. From the various simulations without noise (passive system, linear gain system, nonlinear gain system) we know there are two modes on either side of $k_a = 10.5\ \mu\text{m}^{-1}$. In all previous spectra with noise, a single "combined" peak (usually labeled peak 3) appeared. Figure 4.21 suggests the amplitude of these modes is changing in time. An explanation for the temporal change of peak 4 is currently lacking. Dynamics and noise result in complicated behavior requiring further in-depth studies. We neglect these temporal fluctuations in this thesis by performing integrations over a much longer time.

In Sec. 3.3, noise is observed to increase the true lasing threshold of a single-mode dielectric slab laser. The same effect was seen in random lasers. In the ballistic regime, the first threshold was reached at $P_r = 1.06$. With noise, the true lasing threshold is closer to $P_r = 2.00$, though not precisely determined. Qualitatively, it is certain that noise does

affect the lasing thresholds of modes. Even if different modes are lasing at different times, they are lasing nonetheless. Without noise, thresholds are reached for much smaller values of P_r. To be more precise, with noise, the lasing threshold of modes is increased, but only for modes that have small lasing thresholds without noise. The change for modes that had large lasing thresholds without noise remains to be seen. For example, the large threshold modes for $l_G/L = 1/3$ in Fig. 4.4(b) have not yet been observed in simulations with noise included. Noise may actually decrease these lasing thresholds, but this was not observed for the range of pumping rates considered.

Because the thresholds of modes change when considering noise, the number of lasing modes for a particular pumping rate changes. For small pumping rates, the number of true lasing modes decreases. For large pumping rates, the number of true lasing modes either remains the same or increases (depending on future studies into large threshold modes). For intermediate pumping rates, the fuzziness of the lasing threshold makes it difficult to determine the number of lasing modes with noise. As previously mentioned, future studies into the intensity variance should determine lasing thresholds more precisely and help to answer this question.

Concerning partial pumping effects, the lasing thresholds of the *available* lasing modes become increasingly separated when considering partial pumping. Consequently, the lasing frequencies also become increasingly separated. Thus, even with noise for the range of pumping rates examined here, the modes with very large lasing thresholds are ignored and the remaining modes are well separated in frequency. This makes it is easier to obtain discrete lasing peaks with partial pumping.

CHAPTER 5

Spatially Nonuniform Gain Distributions

The previous chapter showed that spatially nonuniform distributions of gain do appear to facilitate the observation of discrete lasing peaks from random lasers. In this chapter, we further explore the consequences of nonuniform gain distributions for open complex systems.

In Section 5.1, numerical methods used to study the lasing modes of 1D random dielectric structures are described. A scheme for decomposing the lasing modes in terms of quasi modes is presented. A method to separate traveling wave and standing wave components from the total electric field is introduced. Results of simulations of passive random systems and random lasers with uniform gain are discussed in Section 5.2. Modal behavior with reduction of the spatial gain region is studied in Section 5.3. Mode mixing results are presented in Section 5.4 and the disappearance and appearance of lasing modes is discussed in Section 5.5.

5.1. Numerical Methods

A numerical method based on the transfer matrix (see Sec. 1.4.4) is used to calculate both the quasi modes and the lasing modes in a random structure. Recall that the boundary conditions for outgoing fields only require $M_{22} = 0$. For structures without gain, wavevectors must be complex in order to satisfy the boundary conditions. The field inside the structure is represented by $p(x)\exp[in(x)\tilde{k}x] + q(x)\exp[-in(x)\tilde{k}x]$, where

$\tilde{k} = k + ik_i$ is the complex wavevector and x is the spatial coordinate. For outgoing only boundary conditions ($M_{22} = 0$), $k_i < 0$. The resulting field distributions associated with the solutions for these boundary conditions are the quasi modes of the passive system.

Linear gain is simulated by appending an imaginary part to the dielectric function $\epsilon(x) = \epsilon_r(x) + i\epsilon_i(x)$, where $\epsilon_r(x) = n^2(x)$. This approximation is only valid at or below threshold [**167**]. In Sec. 1.4.4.2, the complex index of refraction is calculated as $\tilde{n}(x) = \sqrt{\epsilon(x)} = n_r(x) + in_i$, where $n_i < 0$. We consider n_i to be constant everywhere within the random system. This yields a gain length $l_g = 1/k_i = 1/n_i k$ ($k = 2\pi/\lambda$ is the vacuum wavenumber of a lasing mode) which is the same in the dielectric layers and the air gaps. The real part of the index of refraction is modified by the imaginary part as $n_r(x) = \sqrt{n^2(x) + n_i^2}$. A real wavevector $k = 2\pi/\lambda$ describes the lasing frequency. The field inside the structure is now represented by $p(x)\exp[i\tilde{n}(x)kx] + q(x)\exp[-i\tilde{n}(x)kx]$. The frequencies and thresholds are located by determining which values of k and n_i, respectively, satisfy $M_{22} = 0$.

Nonuniform gain is introduced through an envelope function $f_E(x)$ multiplying n_i. The envelope considered here is the step function $f_E(x) = H(-x + l_G)$, where $x = 0$ is the left edge of the random structure and $x = l_G$ is the location of the right edge of the gain region. l_G may be chosen as any value between 0 and L.

The solutions of the system are given by the points at which the complex transfer matrix element $M_{22} = 0$. Where $\mathrm{Re}[M_{22}] = 0$ or $\mathrm{Im}[M_{22}] = 0$, "zero lines" are formed in the plane of either complex $\tilde{k}$ (passive case) or (k, n_i) (active case). The crossing of a real and imaginary zero line results in $M_{22} = 0$ at that location, thus revealing a solution. We

visualize these zero lines by plotting $|\log_{10} \mathrm{Re}\, M_{22}|$ and $|\log_{10} \mathrm{Im}\, M_{22}|$ and using various image processing techniques to enhance the contrast.

The solutions are pinpointed more precisely by using the Secant method. Locations of minima of $|M_{22}|^2$ and a random value located closely to these minima locations are used as the first two inputs to the Secant method. Once a solution converges or $|M_{22}| < 10^{-12}$, a solution is considered found. This method has proved extremely adept at finding genuine solutions when suitable initial guesses are provided.

Verification of these solutions is provided by the phase of M_{22}, calculated as $\theta = \mathrm{atan2}(\mathrm{Im}\, M_{22}, \mathrm{Re}\, M_{22})$. Locations of vanishing M_{22} give rise to phase singularities since both the real and imaginary parts of M_{22} vanish. The phase change around a path surrounding a singularity in units of 2π is referred to as topological charge [**168, 169**]. In the cases studied here, the charge is $+1$ for phase increasing in the clockwise direction and -1 for phase increasing in the counterclockwise direction.

5.1.1. Biorthogonal Decomposition of Lasing Modes

Once a solution is found, the complex spatial field distribution may be calculated. Quasi modes $\psi(x)$ are calculated in the passive case and lasing modes $\Psi(x)$ are calculated in the active case. In order to determine whether or not mode mixing occurs (and if so, to what degree) in the case of nonuniform gain, the lasing modes are decomposed in terms of the quasi modes of the passive system. It was found [**170, 171**] that any spatial function defined inside an open system of length L [we consider the lasing modes $\Psi(x)$ here] can

be expressed as

$$\Psi(x) = \sum_m a_m \psi_m(x), \tag{5.1}$$

where $\psi_m(x)$ are a set of quasi modes characterized by the complex wavevectors $\tilde{k}_m$. The coefficients a_m are calculated by

$$\begin{aligned} a_m =& i \int_0^L \left[\Psi(x)\hat{\psi}_m(x) + \hat{\Psi}(x)\psi_m(x) \right] dx \\ &+ i \left[\Psi(0)\psi_m(0) + \Psi(L)\psi_m(L) \right], \end{aligned} \tag{5.2}$$

where

$$\hat{\psi}_m(x) = -i\tilde{k}_m n^2(x)\psi_m(x) \tag{5.3a}$$

$$\hat{\Psi}(x) = -ik \left[n_r(x) + i n_i f_E(x) \right]^2 \Psi(x). \tag{5.3b}$$

The normalization condition is

$$\begin{aligned} 1 =& i \int_0^L 2\psi(x)\hat{\psi}(x)dx + i \left[\psi^2(0) + \psi^2(L) \right] \\ =& i \int_0^L 2\Psi(x)\hat{\Psi}(x)dx + i \left[\Psi^2(0) + \Psi^2(L) \right]. \end{aligned} \tag{5.4}$$

An advantage of this decomposition method is that a calculation over an infinite system has been reduced to a calculation over a finite system. Error checking is done by using the coefficients found in Eq. (5.2) to reconstruct the lasing mode intensity distribution with Eq. (5.1) yielding $R(x) \equiv \sum_m a_m \psi_m(x)$. We define a reconstruction error E_R to

monitor the accuracy of the decomposition:

$$E_R = \frac{\int |\Psi(x) - R(x)|^2 dx}{\int |\Psi(x)|^2 dx}. \tag{5.5}$$

5.1.2. Standing Wave and Traveling Wave Components

In this section, we describe the method that enables one to define a standing wave component and a traveling wave component of the field at each point x of a 1D system.

For an open structure without gain, the field reads

$$\psi(x) = p(x)\exp[in(x)\tilde{k}x] + q(x)\exp[-in(x)\tilde{k}x], \tag{5.6}$$

where $\tilde{k}$ is the complex wavevector and $n(x)$ is the index of refraction, the value of which alternates between $n(x) = n_1 > 1$ in dielectric layers and $n(x) = n_2 = 1$ in air gaps. For structures with gain, the field reads

$$\Psi(x) = p(x)\exp[i\tilde{n}(x)kx] + q(x)\exp[-i\tilde{n}(x)kx], \tag{5.7}$$

where $\tilde{n}(x) = n(x) + in_i$ is the complex index of refraction. We rewrite both equations in the single form

$$E(x) = p(x)\exp[i\tilde{K}(x)x] + q(x)\exp[-i\tilde{K}(x)x], \tag{5.8}$$

where $\tilde{K}(x) = K_r(x) + iK_i(x)$ and $E(x)$ may be either $\psi(x)$ or $\Psi(x)$.

For now, we will consider the field within a single layer in order to simplify the notation. The following results will be valid within any layer. Since within a layer, the coefficients

$p(x)$, $q(x)$ and the wavevector $\tilde{K}(x)$ do not depend on x, we rewrite Eq. (5.8) as

$$E(x) = p\exp[i\tilde{K}x] + q\exp[-i\tilde{K}x]. \tag{5.9}$$

The complex amplitudes p and q of the right-going and left-going fields, respectively, can be written as $p = P\exp[i\varphi]$ and $q = Q\exp[i\phi]$ where P and Q are the real amplitudes which can be chosen positive. The field becomes

$$\begin{aligned} E(x) =& P\exp[-K_i x]\exp[i(K_r x + \varphi)] \\ &+ Q\exp[K_i x]\exp[-i(K_r x - \phi)] \\ =& \Pi(x)\exp[i(K_r x + \varphi)] \\ &+ \Theta(x)\exp[-i(K_r x - \phi)], \end{aligned} \tag{5.10}$$

where $\Pi(x) \equiv P\exp[-K_i x]$ and $\Theta(x) \equiv Q\exp[K_i x]$. Introducing the global phase $\Phi \equiv [\varphi + \phi]/2$ and the difference $\Delta \equiv [\varphi - \phi]/2$, the field reads

$$\begin{aligned} E(x) =& \exp[i\Phi]\{\Pi(x)\exp[i(K_r x + \Delta)] \\ &+ \Theta(x)\exp[-i(K_r x + \Delta)]\}. \end{aligned} \tag{5.11}$$

Within a single layer, we can set $\Phi = 0$ so that the field becomes

$$\begin{aligned} E(x) =& \Pi(x)\exp[i(K_r x + \Delta)] + \Theta(x)\exp[-i(K_r x + \Delta)] \\ =& E^{(R)}(x) + E^{(L)}(x), \end{aligned} \tag{5.12}$$

where $E^{(R)}(x)$ and $E^{(L)}(x)$ are the right-going and left-going waves, respectively.

We can build a standing wave component with $E^{(R)}(x)$ as

$$\begin{aligned} E^{(S)}(x) =& E^{(R)}(x) + [E^{(R)}(x)]^* \\ =& 2\Pi(x)\cos[K_r x + \Delta] \end{aligned} \tag{5.13}$$

and define the traveling wave component as the remaining part of the total field

$$\begin{aligned} E^{(T)}(x) =& E(x) - E^{(S)}(x) \\ =& E^{(L)}(x) - [E^{(R)}(x)]^* \\ =& [\Theta(x) - \Pi(x)]\exp[-i(K_r x + \Delta)]. \end{aligned} \tag{5.14}$$

Hence, $2\Pi(x)$ and $[\Theta(x) - \Pi(x)]$ are the amplitudes of the standing wave and traveling wave components, respectively.

It is also possible to build a standing wave component with $E^{(L)}(x)$ as

$$\begin{aligned} E^{(S)}(x) =& E^{(L)}(x) + [E^{(L)}(x)]^* \\ =& 2\Theta(x)\cos[K_r x + \Delta] \end{aligned} \tag{5.15}$$

so that the traveling wave component reads

$$\begin{aligned} E^{(T)}(x) =& E(x) - E^{(S)}(x) \\ =& E^{(R)}(x) - [E^{(L)}(x)]^* \\ =& [\Pi(x) - \Theta(x)]\exp[i(K_r x + \Delta)]. \end{aligned} \tag{5.16}$$

Comparing both ways of resolving the total field into its two components, we see that in Eq. (5.14) the traveling wave component is a left-going wave while in Eq. (5.16) it is a right-going wave. Hence, if in the expression of the field in Eq. (5.12), the prevailing wave is the right-going wave $\Pi(x)\exp[i(K_r x+\varphi)]$ (i.e., $\Pi(x) > \Theta(x)$), we choose the standing and traveling wave components of Eqs. (5.15) and (5.16). In the opposite case of $\Pi(x) < \Theta(x)$, we choose the standing and traveling wave components of Eqs. (5.13) and (5.14).

Let us note that the imaginary part of the total field $E(x)$ is given in both cases by

$$\mathrm{Im}[E(x)] = [\Pi(x) - \Theta(x)]\sin[K_r x + \Delta]. \tag{5.17}$$

As expected, the presence of a traveling wave component, i.e., $|\Pi(x) - \Theta(x)| \neq 0$, makes $E(x)$ become complex instead of being real for a pure standing wave.

5.1.3. Effective Potential of a Dielectric Structure

Further physical insight on lasing mode formation and disappearance, as well as new lasing mode appearance is provided by a mapping of an "effective potential" dictated by the random structure. Local regions of the random medium reflect light at certain frequencies but are transparent to others [**172**]. The response of a structure to a field with frequency $\omega = ck$ can be calculated via a wavelet transformation of the real part of the dielectric function $\epsilon_r(x) = n^2(x)$ [**173**]. The relationship between the local spatial frequency q_{res} and the optical wavevector k is approximately $q_{res} = 2k$ in weakly scattering structures.

The Morlet wavelet χ is expressed as

$$\chi\left(\frac{x'-x}{s}\right) = \frac{\pi^{-1/4}}{\sqrt{s}} e^{i\omega_0(x'-x)/s} e^{-(x'-x)^2/2s^2}, \tag{5.18}$$

with nondimensional frequency ω_0 and Gaussian envelope width s [**174**]. With ω_0 fixed, stretching the wavelet through s changes the effective frequency. Wavelets with varying widths are translated along the spatial axis to obtain the transformation

$$W(x, q_{res}) = \int \epsilon_r(x') \chi^* \left(\frac{x'-x}{s}\right) dx'. \tag{5.19}$$

where

$$q_{res} = \frac{\omega_0 + \sqrt{2+\omega_0^2}}{2s}. \tag{5.20}$$

The wavelet power spectrum $|W(x, q_{res})|^2$ is interpreted as an effective potential. Regions of high intensity indicate potential barriers and regions of low intensity indicate potential wells for light frequency $\omega = q_{res}c/2$.

5.2. Passive and Uniform Gain Systems

A random system of $N = 161$ layers is examined in the following as an example of a random 1D weakly scattering system. The indices of refraction of the dielectric layers are $n_1 = 1.05$ and the air gaps $n_2 = 1$. The average thicknesses are $\langle d_1 \rangle = 100$ nm and $\langle d_2 \rangle = 200$ nm giving a total average length of $\langle L \rangle = 24100$ nm. The grid origin is set at $x = 0$ and the length of the random structure L is normalized to $\langle L \rangle$. The degree of randomness is set to $\eta = 0.9$ and the index of refraction outside the random media is $n_0 = 1$. The localization length ξ is calculated following the method in Sec. 1.1.2.

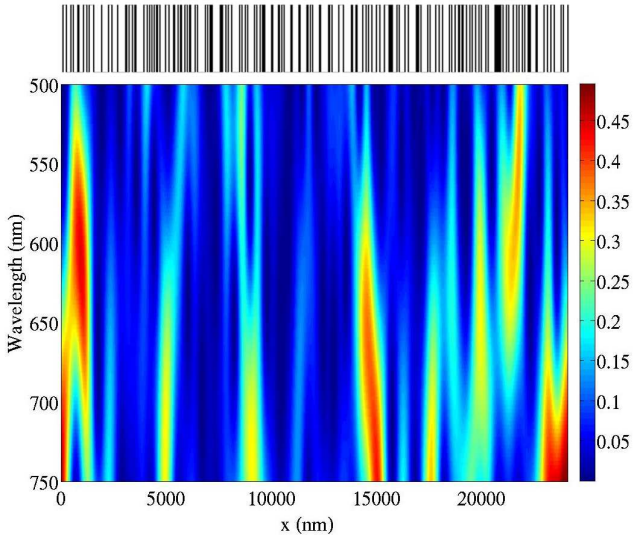

Figure 5.1. Effective potential (wavelet power spectrum) $|W(x)|^2$ of the dielectric function $\epsilon_r(x)$ as a function of position x and wavelength λ. Regions of high intensity indicate potential barriers and regions of low intensity indicate potential wells where intensities are typically trapped. The black lines on the top represent the spatial distribution of dielectric constant $\epsilon_r(x) = n^2(x)$.

The above parameters ensure that the localization length is nearly constant at 200 μm $\leq \xi \leq$ 240 μm over the wavelength range 500 nm $\leq \lambda \leq$ 750 nm. With $\xi \gg L$, the system is in the ballistic regime.

Figure 5.1 shows the effective potential of the structure within the wavelength range of interest via a wavelet transformation. We use a nondimensional frequency of $\omega_0 = 6$ [**175**] and a spatial sampling step of $\Delta x = 2$ nm. The power spectrum $|W(x)|^2$ reveals the landscape of the effective potential dictated by the locations and thicknesses of the dielectric layers.

Figure 5.2 is a phase map of M_{22} in the passive case (with no gain). The phase singularities mark the quasi modes' $\tilde{k}$ values and are indicated by phase changes from $-\pi$ to π along any lines passing through. The topological charge of all quasi modes

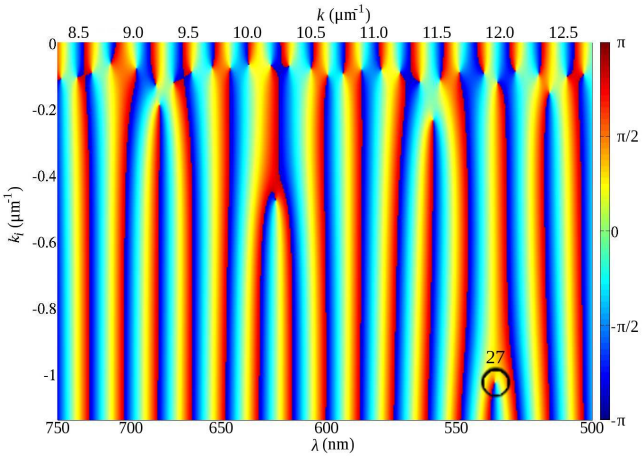

Figure 5.2. A mapping of the phase θ of M_{22} for the passive 1D random system with no gain. The topological charge of all quasi modes seen here is -1. Modes are enumerated from left to right. Quasi mode 27 is encircled in black.

is -1. Adjacent modes are formed by real and imaginary zero lines of M_{22} that are not connected to one another. We calculated M_{22} for increasingly large $|k_i|$ values until machine precision was reached and no additional modes were found. As previously found [**47**], mode frequency spacing is fairly constant in the ballistic regime. The nearly equal spacing of phase singularities in Fig. 5.2 attests to this.

Most quasi modes have similar decay rates except for a few which have much larger decay rates. Modes are enumerated here starting with the lowest frequency mode in our wavelength range of interest. Mode 1 has a wavelength of 748 nm and mode 33 has a wavelength of 502 nm. Most quasi modes have k_i values around -0.1 μm^{-1}. But a few have much larger decay rates, such as mode 27 at $\lambda = 532$ nm which has $k_i = -1.03$ μm^{-1} (encircled in black in Fig. 5.2). Figure 5.3 shows the intensity of mode 27 to be concentrated on one side of the open structure. We observe that it bears similarity to

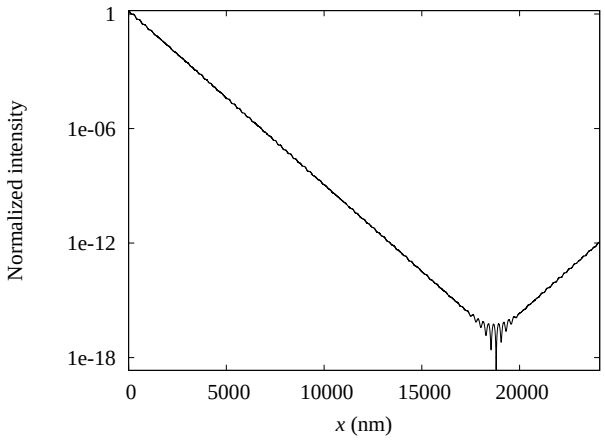

Figure 5.3. Normalized intensity $|\psi(x)|^2$ of a leaky mode - quasi mode 27 ($\tilde{k} = 11.8 - i1.03\ \mu\text{m}^{-1}$) of the passive random 1D structure. The intensity is peaked at the left boundary of the structure, similar to doorway states.

"doorway states" common to open quantum systems [**176**]. Doorway states are concentrated around the boundary of a system and strongly couple to the continuum of states outside the structure. Therefore, they have much larger decay rates.

Figure 5.4 compares the quasi mode frequencies and decay rates to the thresholds (multiplied by k for comparison). For the case of uniform gain, only the lasing modes with large thresholds change significantly from the quasi modes of the passive system [Fig. 5.4(c)]. Finding the corresponding quasi modes for lasing modes with large thresholds is challenging due to changes caused by the addition of a large amounts of gain. However, there is a clear one-to-one correspondence with quasi modes for the remaining lasing modes [Figs. 5.4(a) and (b)]. It is straightforward to find the matching quasi modes for these lasing modes and calculate their differences. The average percent difference between quasi mode frequencies and lasing mode frequencies in Fig. 5.4(a) is 0.013% and in Fig. 5.4(b) is 0.15%. The average percent difference between quasi mode decay rates k_i and lasing thresholds $n_i k$ in Fig. 5.4(a) is 2.5% and in Fig. 5.4(b) is 21%.

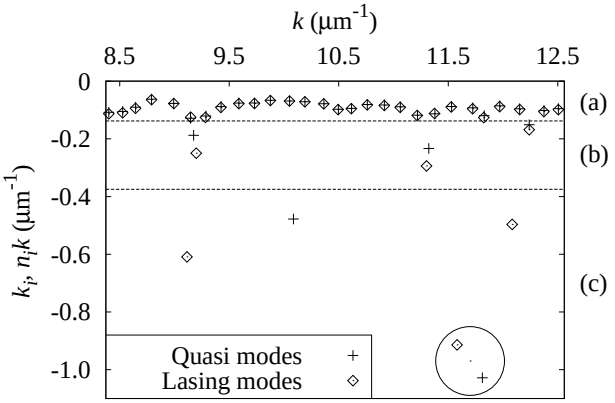

Figure 5.4. The frequencies k of quasi modes (crosses) and lasing modes with linear gain (open diamonds) together with the decay rates k_i of quasi modes and the lasing thresholds $n_i k$ of lasing modes. The horizontal dashed lines separate 3 different regions of behavior: (a) lasing modes are easily matched to quasi modes, (b) clear differences appear but matching lasing modes to quasi modes is still possible, (c) lasing modes have shifted so much it is difficult to match them to quasi modes. The quasi mode with the largest decay rate and the lasing mode with the largest threshold are circled, though they may not be a matching pair.

The normalized intensities of the quasi modes $I_Q(x) \equiv |\psi(x)|^2$ and lasing modes $I_L(x) \equiv |\Psi(x)|^2$ are also compared. Figure 5.5 shows representative 'pairs' of modes from the 3 regions shown in Fig. 5.4. The spatially averaged percent difference between each pair of modes is calculated as $\sigma_d \equiv (2/L) \int \{|I_Q(x) - I_L(x)|/[I_Q(x) + I_L(x)]\}\, dx \times 100$. For small thresholds [Fig. 5.5(a)], the difference between the lasing modes and the matching quasi modes is very small. The average percent difference between all pairs of modes in this region is $\langle \sigma_d \rangle = 4.0\%$. For lasing modes with slightly larger thresholds [Fig. 5.5(b)], there are clear differences. Nevertheless, we may confidently match each lasing mode in this region with its corresponding quasi mode. The average percent difference between all pairs of modes in this region is $\langle \sigma_d \rangle = 68\%$. As mentioned earlier, it is challenging to find matching pairs of lasing modes and quasi modes for large thresholds. Figure 5.5(c)

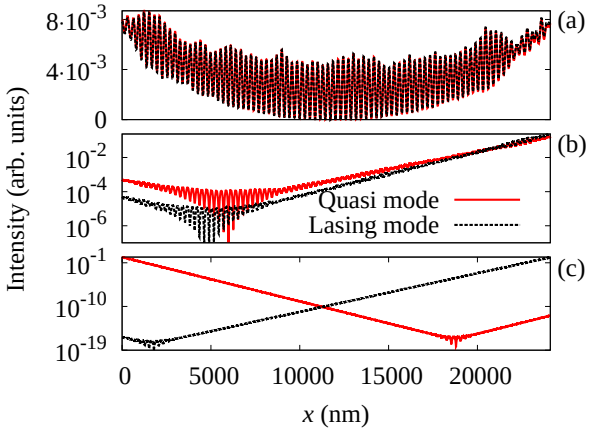

Figure 5.5. Spatial intensity distributions of quasi modes $I_Q(x)$ (red solid lines) and lasing modes $I_L(x)$ (black dashed lines) from each of the 3 regions in Fig. 5.4. Representative samples were chosen for each case. (a) The lasing mode intensity is nearly identical to the quasi mode intensity with $\sigma_d = 2.2\%$. (b) A clear difference appears between the lasing mode and the quasi mode, with $\sigma_d = 90\%$, but they are still similar. (c) The lasing mode with the largest threshold and quasi mode with the largest decay rate are compared, with $\sigma_d = 190\%$. Though these two modes are fairly close to each other [circled in Fig. 5.4(c)], their intensity distributions are quite different.

compares the lasing mode with the largest threshold and the quasi mode with the largest decay rate [circled in Fig. 5.4(a)]. Though these two modes are fairly close to each other in terms of k, k_i, and $n_i k$, their intensity distributions are quite different. Indeed, there may be no correspondence between the two.

The index contrast for this structure is $\Delta n = n_1/n_2 - 1 = 0.05$. Compare this to n_i values in Fig. 5.4: (a) $\langle n_i \rangle \approx 0.01$, (b) $\langle n_i \rangle \approx 0.03$, (c) $\langle n_i \rangle \approx 0.05$. As the threshold n_i approaches Δn, the influence on lasing modes becomes more and more dramatic.

The deviation of the lasing modes from the quasi modes can be explained by the modification of the transfer matrix. In the passive system, k_i is constant, but the imaginary exponent $n(x)k_i$ varies spatially. With the introduction of gain, the imaginary exponent

$n_i k$ becomes constant within the random system, and feedback due to the inhomogeneity of $n(x)k_i$ is removed. However, introducing gain generates additional feedback inside the random system caused by the modification in the real part of the exponent $kn_r(x)$. Neglecting this effect results in some correspondence between lasing modes and quasi modes even at large thresholds [**47**]. Furthermore, since there is no gain outside the random system, $n_i k$ suddenly drops to zero at the system boundary. This discontinuity of $n_i k$ generates additional feedback for the lasing modes. In this weakly scattering system, the threshold gain is high. The large drop of $n_i k$ at the system boundary makes the additional feedback stronger.

5.3. Modal Behavior with Gain Region Reduction

Figure 5.6 maps the (k, n_i) values of lasing modes as nonuniform gain is introduced by reducing the gain region length from $l_G = L$. In this weakly scattering system the intensity distributions of modes are spatially overlapping. This results in a repulsion of mode frequencies [**177**]. As the size of the gain region changes, the envelopes of the intensity distributions change, but for most modes n_i is small enough to leave the optical index landscape unchanged. Thus, the modes continue to spatially overlap as the size of the gain region changes and their frequencies remain roughly the same as in the uniform gain case. Similar frequency behavior can be seen as the gain region length is varied in a simpler cavity with uniform index. However, the threshold values of the lasing modes change as l_G decreases. Due to the limited spatial region of amplification, the thresholds increase. The increase of n_i due to the change of threshold, though considerable, is not

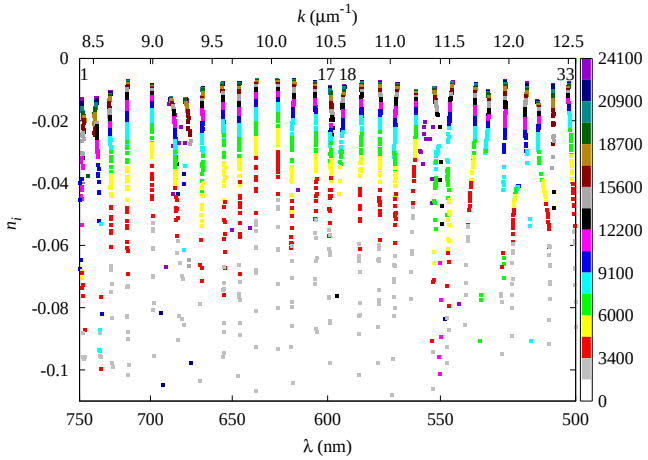

Figure 5.6. Frequencies and thresholds (k, n_i) of the lasing modes of the 1D random structure with gain. Lasing modes 1, 17, 18, and 33 are explicitly marked. The gain region length l_G reduces from uniform gain ($l_G = L$) to nonuniform gain $l_G < L$. The color indicates the value of l_G (units of nm) decremented along the layer interfaces. Due to the random thicknesses of the layers, the l_G increments are unequal. This is the reason for the unequal spacing of the color code.

large enough to significantly impact the lasing frequencies as evidenced by the small change of frequencies as l_G decreases.

The intensity distributions of the lasing modes also change considerably as l_G is reduced. Normalized spatial intensity distributions are given by $|\Psi(x)|^2$ after $\Psi(x)$ has been normalized according to Eq. (5.4). The intensities are sampled with a spatial step of $\Delta x = 2$ nm. With uniform gain ($l_G = 24100$ nm), the intensity of lasing mode 17 ($\lambda = 598$ nm) in Fig. 5.7(a) increases toward the gain boundaries due to weak scattering and strong amplification. When the gain boundary is changed to $l_G = 14284$ nm, the envelope of the spatial intensity distribution changes dramatically. The intensity increases more rapidly toward the boundaries of the gain region and stays nearly constant outside the gain region but still inside the structure. This change can be understood as $|n_i|$ inside

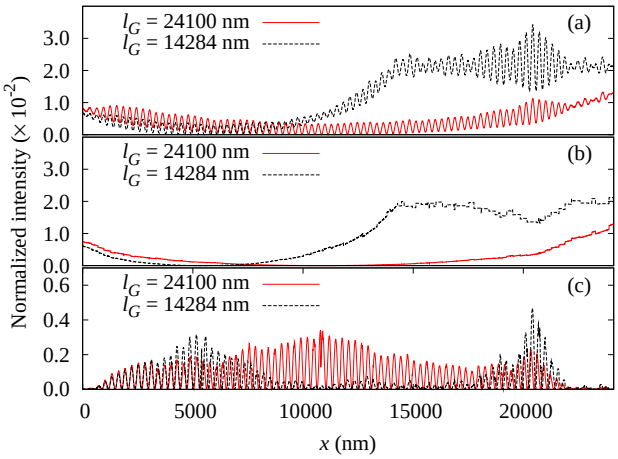

Figure 5.7. Normalized intensity of lasing mode 17 with uniform gain $l_G =$ 24100 nm (red solid lines) and nonuniform gain $l_G = 14284$ nm (black dashed lines). Gain is only located in the region $0 \leq x \leq l_G$. (a) Total intensity $|\Psi(x)|^2$, (b) traveling wave intensity $|\Psi^{(T)}(x)|^2$, and (c) standing wave intensity $|\Psi^{(S)}(x)|^2$. Nonuniform gain significantly changes the spatial intensity envelope as well as the standing wave and traveling wave components.

the gain region causes the intensity to become larger, while outside the gain region $n_i = 0$ and the wavevector is real.

To monitor the change in the trapped component of the intensity, $\Psi(x)$ is separated into a traveling wave and a standing wave component. Figures 5.7(b) and (c) show the traveling wave and standing wave components of lasing mode 17, respectively. For $l_G = L$, the intensity increase towards the structure boundaries is caused mostly by the growth of the traveling wave. The standing wave part is strongest near the center of the system. For $l_G = 14284$ nm, the standing wave exhibits two peaks, one concentrated near the center of the gain region and the other outside the gain region. However, the standing wave intensity outside the gain region should not be directly compared to the standing wave intensity inside the gain region. The total intensity inside the gain region increases toward the gain boundary in this weakly scattering system. Thus, the amplitude of the

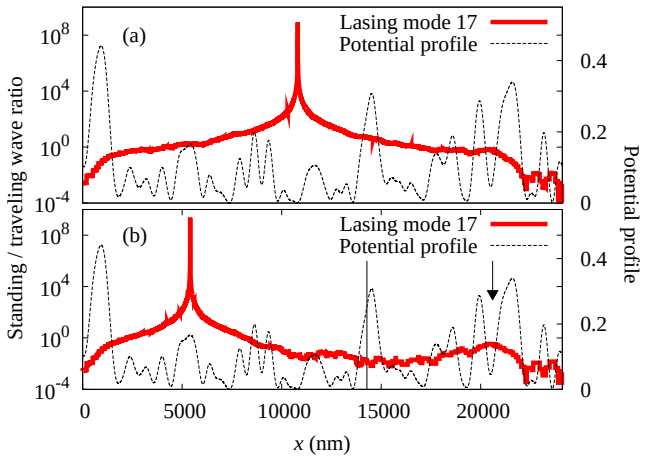

Figure 5.8. Standing/traveling wave ratio $A_{ST}(x)$ (red solid lines) of lasing mode 17 with uniform gain $l_G = L$ (a) and nonuniform gain $l_G = 14284$ nm (b). Gain is located in the regions left of the vertical black solid line. We term the location at which the ratio diverges ($A_{ST}(x) \to \infty$), the standing wave center (SWC). The potential profile $|W(x)|^2$ (black dashed lines) of the dielectric function at the wavelength of mode 17 is overlaid in both (a) and (b).

field outside the gain region, where there is no amplification, is determined by the total field amplitude at the gain boundary. The randomness of the dielectric function outside the gain region traps part of the wave which results in a relatively large standing wave intensity compared to inside the gain region. However, outside the gain region, there is a net flux toward the right boundary of the system meaning the traveling wave intensity in this region is large as well.

The relative strength of the standing wave is calculated through the ratio of standing wave amplitude to traveling wave amplitude. The amplitudes are calculated in Appendix 5.1.2. Depending on whether the prevailing wave is right-going or left-going, the

standing/traveling wave ratio is given by

$$A_{ST}(x) = \begin{cases} \left| \frac{2\Theta(x)}{\Pi(x)-\Theta(x)} \right|^2, \Pi(x) > \Theta(x) \\ \left| \frac{2\Pi(x)}{\Theta(x)-\Pi(x)} \right|^2, \Pi(x) < \Theta(x). \end{cases} \tag{5.21}$$

Results from considering uniform and nonuniform gain for lasing mode 17 are shown in Fig. 5.8. Where the standing wave is largest inside the gain region, $|\Psi^{(T)}(x)| = |\Theta(x) - \Pi(x)| = 0$ and the ratio $A_{ST}(x)$ is infinite. The location where the ratio is diverging is the position of pure standing wave. Fields are emitted in both directions from this position. The prevailing wave to the right of this standing wave center (SWC) is right-going. The prevailing wave to the left of this SWC is left-going. The SWC of the lasing mode is located near the center of the total system when considering uniform gain in Fig. 5.8(a). With the size of the gain region reduced in Fig. 5.8(b), we see that the SWC of the lasing mode (where $A_{ST}(x) \to \infty$) moves to stay within the gain region. Furthermore, note that this mode has a relatively small threshold (see Fig. 5.6). We have found that in general, modes with low thresholds have a SWC near the center of the gain region while high threshold modes have a SWC near the edge of the gain region.

The cause for the small peak of $A_{ST}(x)$ outside the gain region can be found in the potential profile of Fig. 5.1. A slice of the potential profile $|W(x)|^2$ at the wavelength of mode 17 ($\lambda = 598$ nm) is overlaid on the intensities in Fig. 5.8. This suggests the standing wave is weakly trapped in a potential well around $x = 20500$ nm [marked by an arrow in Fig. 5.8(b)].

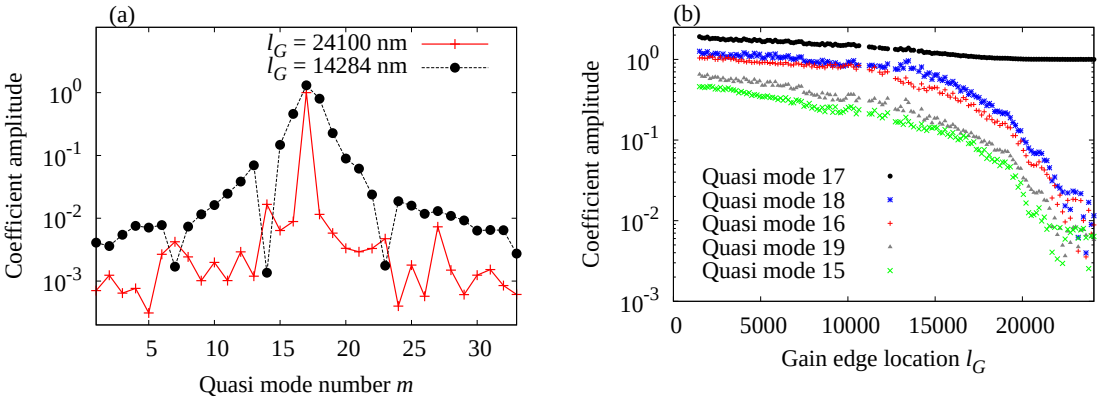

Figure 5.9. Decomposition of lasing mode 17 in terms of passive quasi modes. (a) Decomposition with uniform gain (red crosses) and nonuniform gain (black circles). Leaky quasi modes, i.e., modes with large $|k_i|$ such as modes 7, 14, and 23, contribute to lasing modes markedly different than the others. (b) Five largest coefficients from the decomposition of lasing mode 17. As l_G is reduced, the amount of mode mixing increases dramatically. The reconstruction error E_R for lasing mode 17 is close to 10^{-4} until $l_G =$ 11000 nm then rises to 10^{-2} at $l_G = 3200$ nm. Some coefficients are greater than one. This is possible in open systems.

5.4. Mode Mixing

Lasing modes can be expressed as a superposition of quasi modes of the passive system via Eq. (5.1) for any distribution of gain. Coefficients obtained from the decomposition of the lasing modes in terms of the quasi modes by Eq. (5.2) offer a clear and quantitative way to monitor changes of lasing modes by nonuniform gain. Using Simpson's rule for the numerical integrations and a basis consisting of at least 15 quasi modes at both higher and lower frequencies than the lasing mode being decomposed, we consistently find $E_R \approx 10^{-4}$.

Figure 5.9(a) shows the decomposition of lasing mode 17 with uniform and nonuniform gain. Beginning with the case of uniform gain ($l_G = L$), the largest contribution to lasing mode 17 is from corresponding quasi mode 17. There is a nonzero contribution from other quasi modes on the order 10^{-3}. This reflects slight differences between the lasing mode

profile in the presence of uniform gain and the quasi mode profile [**42, 43, 47**]. With the gain region length reduced to $l_G = 14284$ nm, the coefficients $|a_m|^2$ from quasi modes closer in frequency to the lasing modes increase significantly; i.e., quasi modes closer in frequency are mixed in. The exceptions are the very leaky quasi modes 7, 14, and 23. Unlike leaky quasi mode 27 shown in Fig. 5.3, quasi modes 7, 14, and 23 have intensities which are peaked at the right boundary of the structure. It has been observed that when l_G reduces and the intensity distribution of lasing mode 17 shifts to the left boundary of the structure, there is less overlap with these leaky quasi modes. Thus, the magnitude of the coefficients associated with the leaky modes reduces as shown in Fig. 5.9(a).

Figure 5.9(b) reveals the five largest coefficients $|a_m|^2$ for lasing mode 17 as l_G is incrementally reduced along the dielectric interfaces. While the lasing mode remains dominantly composed of its corresponding quasi mode, neighboring quasi modes mix into the lasing mode significantly. It was shown in [**42, 43**] that linear contributions from gain induced polarization bring about a coupling between quasi modes of the passive system. This coupling arises solely due to the inhomogeneity of the dielectric function, not the openness of the system. While this interaction may play a role in mode mixing with uniform gain, the effect is small compared to the mode mixing caused by the nonuniformity of the gain. This is clearly demonstrated in Fig. 5.9(b), where the coefficients from quasi modes close in frequency are orders of magnitude larger for small l_G than for $l_G = L$.

5.5. Lasing Mode Disappearance and Appearance

As the size of the gain region reduces we observe that some lasing modes disappear and new lasing modes appear. This phenomenon is not limited to random media, but

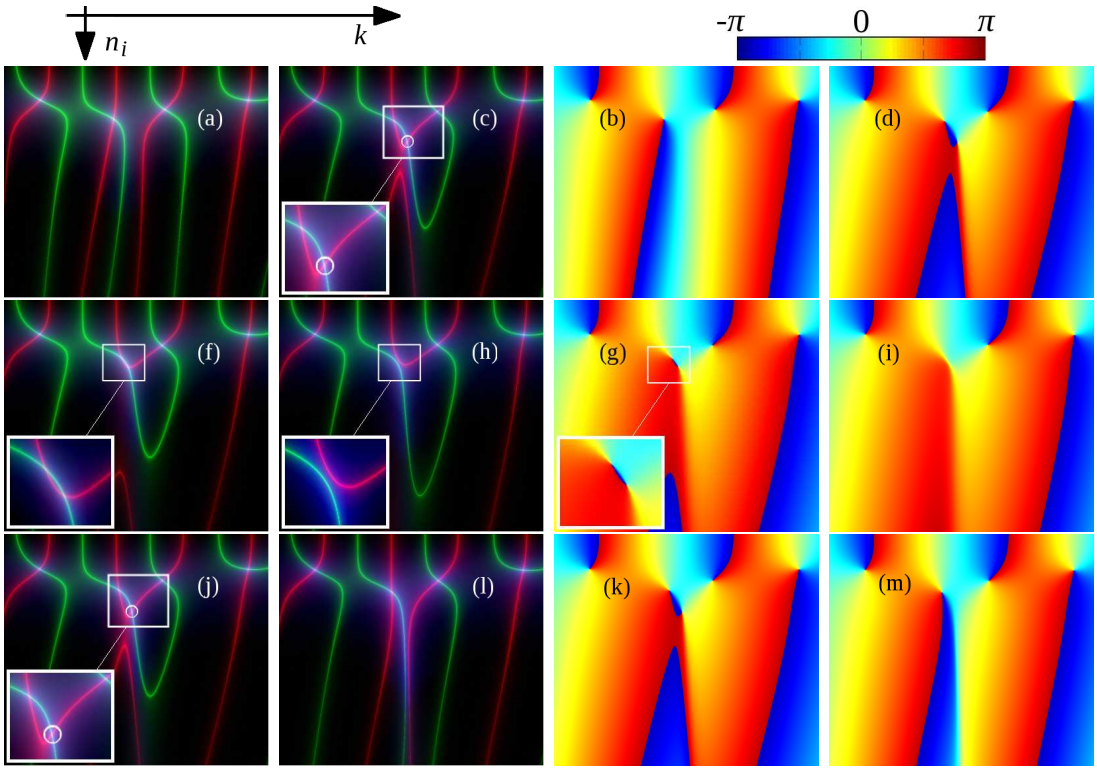

Figure 5.10. (left) Real (green) and Imaginary (red) zero lines of M_{22}. Their crossings indicate (k, n_i) values of lasing modes. (right) Phase maps of M_{22}. All data are in the ranges ($10.3\ \mu\text{m}^{-1} < k < 10.8\ \mu\text{m}^{-1}$) and ($0 \geq n_i \geq -0.074$) covering lasing modes 17 and 18 for $l_G = 14961$ nm (a-b), 14553 nm (c-d), 14523 nm (f-g), 14472 nm (h-i), 14284 nm (j-k), and 14042 nm (l-m). The joining of zero lines in (c) results in the formation of a new lasing mode (new zero line crossing is encircled in white). The inset in (c) is an enlargement of the mode 17 and new mode solutions. In (d), the phase singularity at the new mode has a topological charge of +1, opposite to that of mode 17. The real and imaginary zero lines pull apart in (f) so that the mode 17 and new mode solutions are nearly identical. The phase map in (g) reveals the existence of the two phase singularities. The lines completely separate in (h) resulting in the disappearance of mode 17 and the new mode. The phase map in (i) confirms the disappearance of the two modes. This process reverses itself in (j-m) yielding behavioral symmetry around $l_G = 14472$ nm.

even occurs in a simple 1D cavity with a uniform index of refraction. New lasing modes, to the best of our knowledge, are always created with larger thresholds than the existing

lasing modes adjacent in frequency. The disappearance of lasing modes is not caused by mode competition for gain because gain saturation is not included in our model of *linear gain*. Disappearance/appearance events occur more frequently for smaller values of l_G. New lasing modes appear at frequencies in between the lasing mode frequencies of the system with uniform gain. These new modes exist only within small ranges of l_G. We also find that the disappearance events exhibit behavioral symmetry (as explained below) around particular values of l_G.

We examine the progression of one representative event in detail. The gaps in the decomposition coefficients for lasing mode 17 in Fig. 5.9(b), in the range 10500 nm $\leq l_G \leq$ 14500 nm, indicate lasing mode 17 does not exist for those distributions of gain. Figure 5.10 shows the real and imaginary zero lines of M_{22} and their accompanying phase maps for l_G = 14961 nm, 14553 nm, 14523 nm, 14472 nm, 14284 nm, and 14042 nm. As l_G decreases, the zero lines of lasing modes 17 and 18 join as seen in the transition from Fig. 5.10(a) to (c). This creates a new mode solution (marked by a white circle) with a frequency between lasing modes 17 and 18 and a larger threshold. The existence of a new lasing mode is confirmed by the phase singularity in Fig. 5.10(d). The new mode is close to mode 17 in the (k, n_i) plane and its phase singularity has the opposite topological charge as seen in Fig. 5.10(d). As l_G decreases further, the joined zero lines forming mode 17 and the new mode pull apart. This causes the two solutions to approach each other in the (k, n_i) plane, i.e., the frequency and threshold of mode 17 increase while the frequency and threshold of the new mode decrease. In Figs. 5.10(f) and (g), the solutions are so close that they are nearly identical, yet they still represent two separate solutions. Further decreasing l_G makes the solutions identical. The zero lines then separate and the

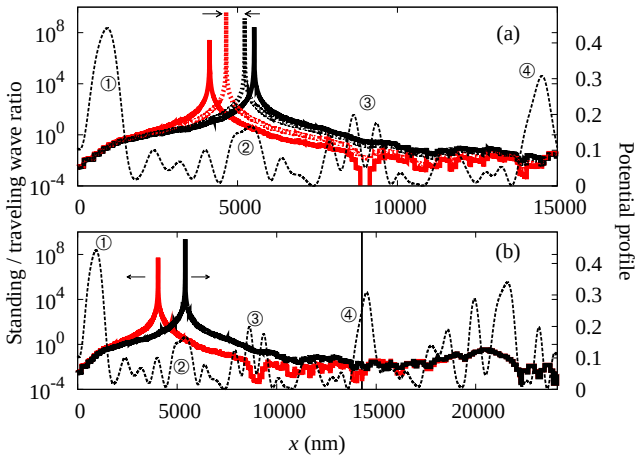

Figure 5.11. (a) Standing/traveling wave ratio $A_{ST}(x)$ of the new lasing mode (red) and lasing mode 17 (black) for $l_G = 14553$ nm (solid lines) and $l_G = 14523$ nm (dotted lines). The potential profile $|W(x)|^2$ (black dashed line) of the dielectric function for this wavelength is overlaid in both (a) and (b) and major potential barriers are marked ① through ④. The intensity distributions of the new lasing mode and lasing mode 17 become more similar an converge on each other as l_G reduces. Reducing l_G further causes these two lasing modes to first disappear then reappear as the process reverses itself. (b) Standing/traveling wave ratio $A_{ST}(x)$ of the new lasing mode (red) and lasing mode 17 (black) after they have reappeared for $l_G = 14284$ nm. The intensity distributions are similar to the distributions for $l_G = 14553$ nm in (a). The vertical black solid line marks the gain edge. The intensity distributions of the modes diverge now as l_G is reduced.

phase singularities of opposite charge annihilate each other in Figs. 5.10(h) and (i). This results in the disappearance of mode 17 and the new mode. The process then reverses itself as l_G is decreased further [Figs. 5.10(j)-(m)] yielding the reappearance of mode 17 and the new mode and their subsequent separation in the (k, n_i) plane. This is the aforementioned behavioral symmetry around $l_G = 14472$ nm.

Examining the standing/traveling wave ratio of lasing mode 17 and the new lasing mode together with the potential profile $|W(x)|^2$ offers some insight of mode annihilation and reappearance in real space. Figure 5.11 shows the intensity distribution for the new

mode and mode 17 along with $|W(x)|^2$. The potential profile is very similar for the new mode and mode 17 since their wavelengths are very close. There are four major potential barriers at the mode 17 wavelength ($\lambda = 598$ nm) for $x < 15000$ nm. This is the spatial region associated with the gain distributions in Fig. 5.10 where l_G is always smaller than 15000 nm. Figure 5.11 shows them at: $x =$ ① 927 nm, ② 5200 nm, ③ 8700 nm, and ④ 14519 nm. Due to oscillations, the centers of barriers ② and ③ are less well defined. The right edge of the gain region at $l_G = 14553$ nm is located just to the right of barrier ④. For $l_G = 14523$ nm, the right edge of the gain region nears the maximum of barrier ④. Figure 5.11(a) shows that for $l_G = 14553$ nm, the SWC of the new mode is between barrier ① and barrier ②. The SWC of mode 17 is in the middle of the gain region at $x = 5300$ nm and its SWC is between barrier ② and barrier ③. Before disappearing, the modes approach each other in the (k, n_i) plane, eventually merge, and their intensity distributions become identical. As l_G is further reduced and the modes reappear, the behavior of the modes' intensity distributions reverses itself as expected from the behavioral symmetry shown in Fig. 5.10. At $l_G = 14284$ nm, the right edge of the gain region has passed barrier ④ and Fig. 5.11(b) [with a different horizontal scale than Fig. 5.11(a)] shows the SWC of the new mode is in roughly the same location as it was for $l_G = 14553$ nm. The SWC of mode 17 is also in roughly the same location as it was for $l_G = 14553$ nm.

The appearance of new lasing modes is unanticipated. In the passive system, the number of standing wave peaks for quasi modes increases incrementally by 1, *e.g.* quasi mode 17 has 82 peaks and quasi mode 18 has 83 peaks. Lasing modes 17 and 18 behave the same way. How exactly does a new lasing mode fit into this scheme? Though closer in frequency and threshold to lasing mode 17, counting the total number of standing wave

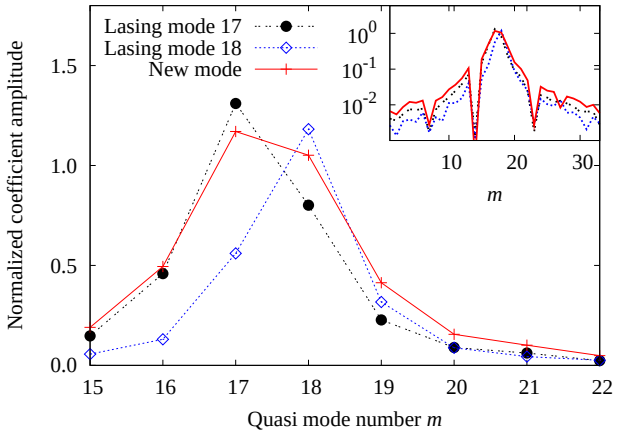

Figure 5.12. Decomposition at $l_G = 14284$ nm of lasing mode 17 (black circles), lasing mode 18 (blue open diamonds), and the new lasing mode (red crosses) in terms of the quasi modes of the passive system. Lasing modes 17 and 18 are mostly composed of their respective quasi modes while the new mode is dominated by a mixture of both quasi mode 17 and 18. The inset shows the decomposition coefficients of outlying quasi modes for lasing mode 17 (black line), lasing mode 18 (blue line), and the new lasing mode (red line).

peaks of the new lasing mode yields the same number as for lasing mode 18. However, the new lasing mode is somewhat compressed in the gain region having one more peak than lasing mode 18. It is decompressed in the region without gain having one less peak than lasing mode 18.

Comparing the decompositions of the lasing modes in terms of quasi modes helps reveal the character of the new lasing mode. Figure 5.12 shows the decomposition of the new lasing mode together with the decomposition of lasing modes 17 and 18 at $l_G = 14284$ nm. The new mode has a slightly larger coefficient amplitude associated with quasi mode 17 than quasi mode 18, but the two amplitudes are nearly equal. We found that as mode 17 and the new mode solutions approach each other by varying l_G, their coefficient

distributions also approach each other until becoming equal as expected from Figs. 5.10 and 5.11.

For a more thorough study of the new lasing modes and confirmation of their existence in the presence of gain saturation, we switch to a more realistic gain model including nonlinearity. The Maxwell-Bloch (MB) equations, as described in Sec. 1.4.3, are employed. The phenomenological decay times due to the excited state's lifetime T_1 and decoherence T_2 are included. The gain spectral width is given by $\Delta\omega_a = 1/T_1 + 2/T_2$ [**14**]. We also include incoherent pumping of atoms. The equations are solved numerically with the spatial grid step $\Delta x = 1.0$ nm and the temporal step $\Delta t = 3.3 \times 10^{-18}$ s. The atomic density $N_{atom}/V = 1.8 \times 10^{13}$ cm^{-3}. Nonuniform gain is simulated by having the two-level atoms only in the region $0 \leq x \leq l_G$.

By setting the atomic transition wavelength λ_a to coincide with the wavelength of mode 1, 2 or the new mode and using a narrow gain spectrum, we are able to investigate the three lasing modes separately. $\Delta\omega_a$ is chosen to be less than the mode spacing to ensure single mode lasing (at smaller pumping rates). At $l_G = 14.295$ μm, the wavelength difference between mode 2 and the new mode, which is smaller than that between mode 1 and the new mode, is $\lambda_2 - \lambda_{nm} = 1.4$ nm. We set $T_1 = 1.0 \times 10^{-12}$ s and $T_2 = 0.73 \times 10^{-12}$ s so that the gain spectral width in terms of wavelength is $\Delta\lambda_a = 0.71$ nm. Initially all atoms are in their ground state and the system is excited by a Gaussian-sinusoidal pulse with center wavelength $\lambda_0 = \lambda_a$ and spectral width $\Delta\lambda_0 = \Delta\lambda_a$. When the pumping rate P_r is above a threshold value, the electromagnetic fields build up inside the system until a steady state is reached.

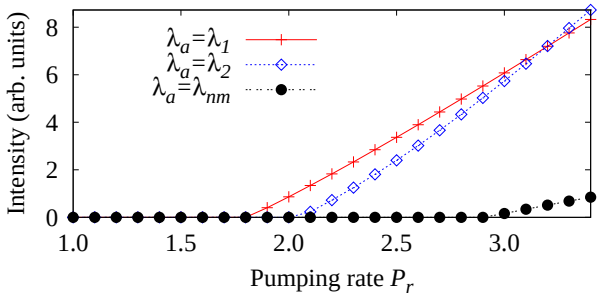

Figure 5.13. Steady-state output intensity vs. pumping rate P_r from Maxwell-Bloch simulations with different gain spectra. The wavelength of the atomic transition λ_a is equal to λ_1 (red crosses), λ_2 (blue open diamonds), and λ_{nm} (black circles) [**178**].

Figure 5.13 shows the steady-state output intensity with $\lambda_a = \lambda_1$, λ_2, or λ_{nm} as P_r is varied. $P_r = 1$ corresponds to the transparency point, namely, the excited state population of atoms is equal to that of the ground state. The lasing threshold pumping rate for mode 1 is reached first at $P_r = 1.9$, then mode 2 at $P_r = 2.1$ and the new mode at $P_r = 3.0$. These thresholds agree qualitatively with the values of the TM calculation.

When $\lambda_a = \lambda_{nm}$, the first lasing mode is the new mode, instead of mode 1 or 2. Figure 5.14(a) shows the output emission spectrum just above the lasing threshold at $P_r = 3.0$. It consists of a single lasing mode with the wavelength equal to that of the new mode calculated with the TM method. The spatial intensity distribution obtained from the Maxwell-Bloch (MB) calculation is compared to that from the TM calculation in Fig. 5.14(b). The MB distribution $|\phi_{MB}(x)|^2$ is found by integrating the intensity over one optical period. It is then normalized to the TM distribution $|\phi_{TM}(x)|^2$ as $\int_0^L |\phi_{MB}(x)|^2 dx = \int_0^L |\phi_{TM}(x)|^2 dx$. The two intensity distributions are almost identical. The average percent difference between them is 7.77%. This result indicates the nonlinear effect due to gain saturation is small when the pumping rate is just above the lasing

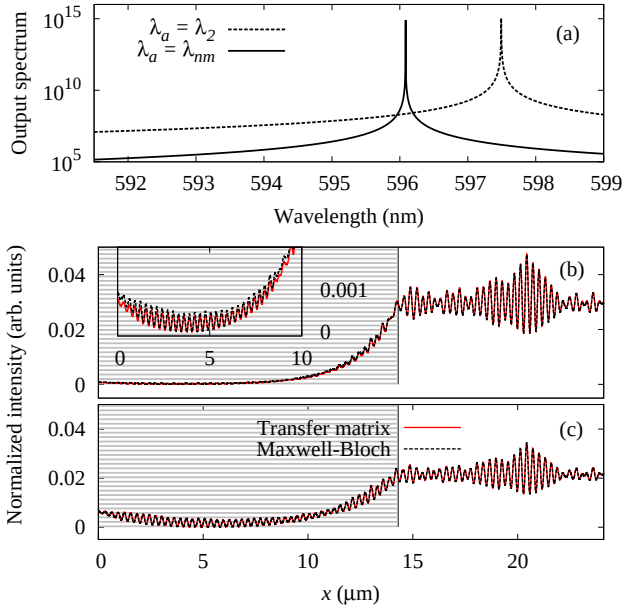

Figure 5.14. (a) Emission spectra taken from two Maxwell-Bloch simulations with λ_a equal to λ_{nm} (solid line) and λ_2 (dashed line). In both cases, $\Delta\lambda_a = 0.71$ nm, $l_G = 14.295\ \mu$m. $P_r = 3.0$ for the solid curve and 2.1 for the dashed curve. The emission intensity reaches a steady state by a simulation time of $t = 300 \times 10^{-12}$ s. The spectra are taken from 1400×10^{-12} s to 1700×10^{-12} s. The MB intensity distribution $|\phi_{MB}(x)|^2$ (black dashed line) is compared to the TM intensity distribution $|\phi_{TM}(x)|^2$ (red solid line) for the new lasing mode (b) and mode 2 (c). The inset in (b) is an expansion of the curves for $0\ \mu\text{m} < x < 10\ \mu$m.

threshold. When the peak of the gain spectrum is shifted from λ_{nm} to λ_1 or λ_2, the first lasing mode is switched to mode 1 or 2. Figure 5.14(c) plots the spatial intensity distribution of mode 2 obtained by the MB calculation with $\lambda_a = \lambda_2$ and $P_r = 2.1$ as well as that obtained by the TM calculation. The two distributions are almost the same and they are different from the distribution with uniform gain. Comparing Fig. 5.14(b) to (c), we see the spatial intensity distribution of the new lasing mode differs significantly from that of mode 2 within the gain region. Outside the gain region the two distributions are not much different because their wavelengths are very close.

When optical gain is located on the left side of the structure, we observe that the intensity distributions of new lasing modes are heavily concentrated on the right side of the gain region. This makes the emission intensity through the right boundary of the random system much larger than that through the left boundary. We calculate the the ratio of right to left output flux $S_x \equiv |\phi(x = L)|^2/|\phi(x = 0)|^2$. For the new lasing mode in Fig. 5.14(b) $S_x = 40$, indicating the laser output is mostly to the right. As a comparison, $S_x = 1.1$ for mode 1 and $S_x = 3.3$ for mode 2. Thus, the new lasing mode has much more directional output than modes 1 and 2.

CHAPTER 6

Conclusion

In an effort to simulate fluctuations in macroscopic systems caused by interactions of atoms and photons with reservoirs Such interactions induce temporal decay of photon number, atomic polarization and excited state's population, which can be described phenomenologically by decay constants. The fluctuation-dissipation theorem demands temporal fluctuations or noise to accompany these decays.

In Ch. 2, we included noise caused by the interaction of the light field with external reservoir in an open system. We have calculated the fluctuations of EM fields in open cavities due to output coupling with the FDTD method. The fluctuation dissipation theorem dictates that the cavity field dissipation by leakage be accompanied by thermal noise, which is simulated here by classical electrodynamics. The absorbing boundary of the FDTD grid is treated as a blackbody, which radiates into the grid. We have synthesized the noise sources whose spectrum is equal to that of blackbody radiation. Careful selection of numerical parameters in the FDTD simulation avoids the distortion of the noise spectrum by wave propagation in the 1D grid. It is numerically confirmed that the noise fields propagating in vacuum retain the blackbody spectrum and temporal correlation function. When a cavity is placed in the grid, the thermal radiation is coupled into the cavity and contributes to the thermal noise for the cavity field. We calculate the thermal noise in a 1D dielectric slab cavity. In the Markovian regime where the cavity photon lifetime τ is much longer than the coherence time of thermal radiation

τ_c, the FDTD-calculated amount of thermal noise in a cavity mode agrees with that given by the quantum Langevin equation. This validates our numerical model of thermal noise which originates from cavity openness or output coupling. Our FDTD simulation also demonstrates that in the non-Markovian regime the steady-state number of thermal photons in a cavity mode exceeds that in a vacuum mode. This is attributed to the constructive interference of the thermal field inside the cavity.

In Ch. 3, we developed a numerical model to simulate noise caused by the interaction of atoms with reservoirs such as lattice vibrations and atomic collisions. Specifically, an FDTD algorithm was developed to incorporate stochastic noise in macroscopic systems into the Maxwell-Bloch equations. Such noise, resulting from atom-reservoir interactions, accompanies the dephasing of atomic polarization and decay of and pumping to the excited state population. We applied our algorithm to a numerical simulation of superfluorescence in a 1D system. The results are in good agreement with previous experimental and theoretical studies. An incoherent pumping rate was then included (as well as associated fluctuations) and the influence of noise on a dielectric slab laser was studied. The lasing threshold was found to increase due to noise. A method was developed to objectively calculate the mode linewidth with increasing pumping rates. The result followed the predicted Schawlow-Townes linewidth trend. Although our simulations only include classical noise, nonclassical noise may be incorporated as well. Since they consist of nonlinear terms [**126**], the incorporation of nonclassical fluctuations to the FDTD algorithm may be numerically challenging. Given the rapid progress in development of various numerical methods of including nonlinearity in the Maxwell-Bloch equations [**179, 180**], we are optimistic that the quantum noise terms may be successfully integrated into our method.

In Ch. 4, the effects of noise on a random laser were studied employing the above FDTD-based model which is particularly well suited for studies of light-matter interaction and transient processes in complex systems. Three random lasers yielded very similar results in that lasing thresholds were always found to increase. However, the transition from amplified spontaneous emission to lasing oscillation was different in each case. High index contrast gave lower lasing thresholds, thereby keeping the transition region short. Low index contrast extended this transition region. Again, the trend of mode linewidths was examined. In this case, the laser operated in the multimode regime, which only resulted in a Schawlow-Townes linewidth trend for the dominant mode. The mode with the second largest amplitude showed a linewidth which decreased more slowly with the pumping rate. The third system studied was a partially pumped random laser with low index contrast. As expected, thresholds increased more for this case. However, it was found that lasing action may be more easily obtained due to some modes with large thresholds increasing the effective frequency spacing of the small threshold modes. The number of available lasing modes did not reduce, as previously though, but larger separation in frequency and threshold facilitates lasing action in partially pumped lasers.

These studies are hoped to shed light on the transition from ASE to lasing oscillation in random lasers which is poorly understood. Most notably, ASE can understandably be confused with lasing with nonresonant feedback. It is hoped that future studies with this method will provide clues toward distinguishing the two processes.

In Ch. 5 we extended the study of lasing with partial pumping, or equivalently, spatially nonuniform gain. We demonstrated the characteristics of lasing modes to be

strongly influenced by nonuniformity in the spatial gain distribution in 1D random structures. While the entire structure plays the dominant role in determining the frequency of the lasing modes, the gain distribution mostly determines the lasing thresholds and spatial distributions of intensity. The gain distribution also appears to be solely responsible for the creation of new lasing modes. We have verified the existence of new lasing modes in numerous random structures as well as dielectric slabs of uniform refractive index. All of these changes caused by nonuniform gain take place without the influence of nonlinear interaction between the field and gain medium. Our conclusion is that nonuniformity of the gain distribution alone is responsible for the complicated behavior observed here.

By decomposing the lasing modes in terms of a set of quasi modes of the passive system, we illustrated how the lasing modes change. The contribution of a quasi mode to a lasing mode was seen to depend mostly on its proximity in frequency k and the spatial distribution of gain. The more the gain changed from uniformity, the greater the mixing in of neighboring quasi modes. Thus, great care must be taken even close to the lasing threshold when using the properties of quasi modes to predict characteristics of lasing modes in weakly scattering systems with local pumping.

The change of intensity distributions of lasing modes as the size of the gain region is varied appears to be general. With reduction of the size of the gain region, the peak of the standing/traveling wave ratio $A_{ST}(x)$, or the standing wave center (SWC) of the mode, moves to stay within the gain region. Modes with low thresholds have a SWC near the middle of the gain region while high threshold modes have a SWC near the edge of the gain region. Changing the gain distribution thus changes the intensity distributions of lasing modes. The exact modal distributions, however, appear correlated with the

potential profile. In the cases studied here, the new lasing mode and lasing mode 17 lay in between two large potential barriers. Decreasing the size of the gain region brought the intensity distributions closer together until they disappeared. These changes took place by varying the edge of the gain region only hundreds of nanometers. Thus, even a slight change in the gain distribution may have drastic consequences for lasing modes.

Because of the excellent agreement found between the MB and TM calculations, we conclude that new lasing modes do appear in random lasers with spatially nonuniform distributions of optical gain. Typically, as in the case studied here, they are sensitive to the spatial gain distribution and disappear if the distribution is altered slightly. These new lasing modes offer more control of random laser performance as their properties such as frequency and output directionality can be quite different from those of existing lasing modes. Moreover, the properties of new lasing modes can be easily altered by varying the spatial profile of the pump beam, without modifying the random structures.

References

[1] J. C. Maxwell, "A dynamical theory of the electromagnetic field," Philos. Trans. R. Soc. London, vol. 155, pp. 459–512, 1865.

[2] J. S. Reid, C. H.-T. Wang, and J. M. T. Thompson, "James Clerk Maxwell 150 years on," Phil. Trans. R. Soc. A, vol. 366, pp. 1651–1659, 2008.

[3] O. Heaviside, Electrical Papers. Two volumes, London: Macmillan and Co., 1892.

[4] J. W. Gibbs, The Scientific Papers of J. Willard Gibbs. London: Longmans, Green, and Co., 1906.

[5] E. Akkermans and G. Montambaux, Mesoscopic Physics of Electrons and Photons. Cambridge: Cambridge University Press, 2007.

[6] S. John, "Localization of light," Phys. Today, vol. 44, pp. 32–40, 1991.

[7] S. John, "Electromagnetic absorption in a disordered medium near a photon mobility edge," Phys. Rev. Lett., vol. 53, pp. 2169–2172, 1984.

[8] P. W. Anderson, "The question of classical localization A theory of white paint?," Philos. Mag. B, vol. 52, pp. 505–509, 1985.

[9] H. Cao, "Lasing in random media," Waves in Random and Complex Media, vol. 13, pp. R1–R39, 2003.

[10] A. Einstein, "On the quantum theory of radiation," Phys. Zs., vol. 18, p. 121, 1917.

[11] J. P. Gordon, H. J. Zeiger, and C. H. Townes, "The maser–new type of microwave amplifier, frequency standard, and spectrometer," Phys. Rev., vol. 99, pp. 1264–1274, 1955.

[12] A. L. Shawlow and C. H. Townes, "Infrared and optical masers," Phys. Rev., vol. 112, p. 1940, 1958.

[13] R. G. Gould, "The laser, light amplification by stimulated emission of radiation," The Ann Arbor Conference on Optical Pumping, the University of Michigan, 1959.

[14] A. E. Siegman, Lasers. Mill Valley: University Science Books, 1986.

[15] R. V. Ambartsumian, N. G. Basov, P. G. Kryukov, and V. S. Letokhov, "Laser with nonresonant feedback," JETP Lett., vol. 3, p. 167, 1966.

[16] R. V. Ambartsumian, N. G. Basov, P. G. Kryukov, and V. S. Letokhov, "A laser with nonresonant feedback," IEEE J. Quantum Electron., vol. 2, pp. 442–446, 1966.

[17] N. G. Basov and V. S. Letokhov, "Optical frequency standards," Sov. Phys. Usp., vol. 11, pp. 855–880, 1969.

[18] W. D. Callister, Materials Science and Engineering, An Introduction. New York: John Wiley & Sons, Inc., 4th ed., 1997.

[19] V. S. Letokhov, "Generation of light by a scattering medium with negative resonance absorption," Sov. Phys. JETP, vol. 26, pp. 835–840, 1968.

[20] N. M. Lawandy, R. M. Balachandran, A. S. L. Gomes, and E. Sauvain, "Laser action in strongly scattering media," Nature, vol. 368, pp. 436–438, 1994.

[21] A. Z. Genack and J. M. Drake, "Scattering for super-radiation," Nature, vol. 368, pp. 400–401, 1994.

[22] P. Sheng, Introduction to Wave Scattering, Localization, and Mesoscopic Phenomena. New York: Academic Press, 1995.

[23] H. Cao, Y. G. Zhao, H. C. Ong, S. T. Ho, J. Y. Dai, J. Y. Wu, and R. P. H. Chang, "Ultraviolet lasing in resonators formed by scattering in semiconductor polycrystalline films," Appl. Phys. Lett., vol. 73, pp. 3656–3658, 1998.

[24] H. Cao, Y. G. Zhao, S. T. Ho, E. W. Seelig, Q. H. Wang, and R. P. H. Chang, "Random laser action in semiconductor powder," Phys. Rev. Lett., vol. 82, pp. 2278–2281, 1999.

[25] S. V. Frolov, Z. V. Vardeny, K. Yoshino, A. Zakhidov, and R. H. Baughman, "Stimulated emission in high-gain organic media," Phys. Rev. B, vol. 59, p. R5284, 1999.

[26] S. V. Frolov, Z. V. Vardeny, A. Zakhidov, and R. H. Baughman, "Laser-like emission in opal photonic crystals," Opt. Commun., vol. 162, pp. 241–246, 1999.

[27] K. Yoshino, S. Tatsuhara, Y. Kawagishi, M. Ozaki, A. A. Zakhidov, and Z. V. Vardeny, "Amplified spontaneous emission and lasing in conducting polymers and fluorescent dyes in opals as photonic crystals," Appl. Phys. Lett., vol. 74, pp. 2590–2592, 1999.

[28] D. S. Wiersma, M. P. van Albada, B. A. van Tiggelen, and A. Lagendijk, "Experimental evidence for recurrent multiple scattering events of light in disordered media," Phys. Rev. Lett., vol. 74, pp. 4193–4196, 1995.

[29] C. Gouedard, D. Husson, and C. Sauteret, "Generation of spatially incoherent short pulses in laser-pumped neodymium stoichiometric crystals and powders," J. Opt. Soc. Am. B, vol. 10, pp. 2358–2363, 1993.

[30] R. C. Polson and Z. V. Vardeny, "Organic random lasers in the weak-scattering regime," Phys. Rev. B, vol. 71, p. 045205, 2005.

[31] H. Cao, "Review on latest developments in random lasers with coherent feedback," J. Phys. A: Math. Gen., vol. 38, pp. 10497–10535, 2005.

[32] Y. Ling, H. Cao, A. L. Burin, M. A. Ratner, X. Liu, and R. P. H. Chang, "Investigation of random lasers with resonant feedback," Phys. Rev. A, vol. 64, p. 063808, 2001.

[33] X. Wu, A. Yamilov, A. A. Chabanov, A. A. Asatryan, L. C. Botten, and H. Cao, "Random lasing in weakly scattering systems," Phys. Rev. A, vol. 74, p. 053812, 2006.

[34] S. Mujumdar, M. Ricci, R. Torre, and D. Wiersma, "Amplified extended modes in random lasers," Phys. Rev. Lett., vol. 93, p. 053903, 2004.

[35] X. Wu and H. Cao, "Statistics of random lasing modes in weakly scattering systems," Opt. Lett., vol. 32, pp. 3089–3091, 2007.

[36] X. Wu and H. Cao, "Statistical studies of random-lasing modes and amplified-spontaneous-emission spikes in weakly scattering systems," Phys. Rev. A, vol. 77, p. 013832, 2008.

[37] C. Vanneste and P. Sebbah, "Selective excitation of localized modes in active random media," Phys. Rev. Lett., vol. 87, p. 183903, 2001.

[38] X. Jiang and C. M. Soukoulis, "Localized random lasing modes and a path for observing localization," Phys. Rev. E, vol. 65, p. 025601, 2002.

[39] H. Cao, J. Y. Xu, D. Z. Zhang, S.-H. Chang, S. T. Ho, E. W. Seelig, X. Liu, and R. P. H. Chang, "Spatial confinement of laser light in active random media," Phys. Rev. Lett., vol. 84, p. 5584, 2000.

[40] D. S. Wiersma, "The physics and applications of random lasers," Nature Physics, vol. 4, p. 359, 2008.

[41] V. M. Apalkov, M. E. Raikh, and B. Shapiro, "Random resonators and prelocalized modes in disordered dielectric films," Phys. Rev. Lett., vol. 89, p. 016802, 2002.

[42] L. Deych, "Effects of spatial nonuniformity of cavity dielectric constant on lasing dynamics," Proc. SPIE, vol. 5924, p. 59240B, 2005.

[43] L. Deych, "Effects of spatial nonuniformity on laser dynamics," Phys. Rev. Lett., vol. 95, p. 043902, 2005.

[44] C. Vanneste, P. Sebbah, and H. Cao, "Lasing with resonant feedback in weakly scattering random systems," Phys. Rev. Lett., vol. 98, p. 143902, 2007.

[45] H. E. Türeci, L. Ge, S. Rotter, and A. D. Stone, "Strong interactions in multimode random lasers," Science, vol. 320, p. 643, 2008.

[46] A. Yamilov, X. Wu, H. Cao, and A. L. Burin, "Absorption-induced confinement of lasing modes in diffusive random media," Opt. Lett., vol. 30, p. 2430, 2005.

[47] X. Wu, J. Andreasen, H. Cao, and A. Yamilov, "Effect of local pumping on random laser modes in one dimension," J. Opt. Soc. Am. B, vol. 24, p. A26, 2007.

[48] R. J. Horowicz, H. Heitmann, Y. Kadota, and Y. Yamamoto, "Gaas microcavity quantum-well laser with enhanced coupling of spontaneous emission to the lasing mode," Appl. Phys. Lett., vol. 61, p. 393, 1992.

[49] C. Gmachl, F. Capasso, E. E. Narimanov, J. U. Nöckel, A. D. Stone, J. Faist, D. L. Sivco, and A. Y. Cho, "High-power directional emission from microlasers with chaotic resonators," Science, vol. 280, p. 1556, 1998.

[50] T. Fukushima, T. Harayama, P. Davis, P. O. Vaccaro, T. Nishimura, and T. Aida, "Ring and axis mode lasing in quasi-stadium laser diodes with concentric end mirrors," Opt. Lett., vol. 27, p. 1430, 2002.

[51] G. D. Chern, H. E. Türeci, A. D. Stone, R. K. Chang, M. Kneissl, and N. M. Johnson, "Unidirectional lasing from ingan multiple-quantum-well spiral-shaped micropillars," Appl. Phys. Lett., vol. 83, p. 1710, 2003.

[52] M. Hentschel and T. Y. Kwon, "Designing and understanding directional emission from spiral microlasers," Opt. Lett., vol. 34, p. 163, 2009.

[53] X. H. Wu, A. Yamilov, H. Noh, H. Cao, E. W. Seelig, and R. P. H. Chang, "Random lasing in closely packed resonant scatterers," J. Opt. Soc. Am. B, vol. 21, p. 159, 2004.

[54] C. Vanneste and P. Sebbah, "Localized modes in random arrays of cylinders," Phys. Rev. E, vol. 71, p. 026612, 2005.

[55] S. Gottardo, R. Sapienza, P. D. García, A. Blanco, D. S. Wiersma, and C. López, "Resonance-driven random lasing," Nat. Photonics, vol. 2, p. 429, 2008.

[56] P. D. García, M. Ibisate, R. Sapienza, D. S. Wiersma, and C. López, "Mie resonances to tailor random lasers," Phys. Rev. A, vol. 80, p. 013833, 2009.

[57] P. D. García, R. Sapienza, and C. López, "Photonic glasses: A step beyond white paint," Adv. Mater., vol. 21, p. 1, 2009.

[58] J. Ripoll, C. M. Soukoulis, and E. N. Economou, "Optimal tuning of lasing modes through collective particle resonance," J. Opt. Soc. Am. B, vol. 21, p. 141, 2004.

[59] T. Savels, A. P. Mosk, and A. Lagendijk, "Gain narrowing in few-atom systems," Phys. Rev. Lett., vol. 98, p. 103601, 2007.

[60] D. S. Wiersma and S. Cavalieri, "Light emission: A temperature-tunable random laser," Nature, vol. 414, p. 708, 2001.

[61] K. Lee and N. M. Lawandy, "Laser action in temperature-controlled scattering media," Opt. Commun., vol. 203, p. 169, 2002.

[62] S. Gottardo, S. Cavalieri, O. Yaroshchuk, and D. S. Wiersma, "Quasi-two-dimensional diffusive random laser action," Phys. Rev. Lett., vol. 93, p. 263901, 2004.

[63] H. Fujiwara, Y. Hamabata, and K. Sasaki, "Numerical analysis of resonant and lasing properties at a defect region within a random structure," Opt. Express, vol. 17, p. 3970, 2009.

[64] P. Sebbah and C. Vanneste, "Random laser in the localized regime," Phys. Rev. B, vol. 66, p. 144202, 2002.

[65] W. H. Louisell, Quantum statistical properties of radiation. New York: John Wiley & Sons, 1973.

[66] R. Brown, "A brief account of microscopical observations made in the months of June, July, and August, 1827, on the particles contained in the pollen of plants; and on the general existence of active molecules in organic and inorganic bodies," Philos. Mag., vol. 4, pp. 161–173, 1828.

[67] E. Nelson, Dynamical theories of Brownian motion. Princeton: Princeton University Press, 2nd ed., 2001.

[68] A. Einstein, Investigations on the Theory of the Brownian Movement. Mineola: Dover, 1956.

[69] H. Haken, Light: Waves, Photons, Atoms. New York: North-Holland Physics Publishing, 1981.

[70] M. Lax, "Quantum noise. IV. quantum theory of noise sources," Phys. Rev., vol. 145, p. 110, 1966.

[71] M. P. Langevin, "On the theory of Brownian motion," C. R. Acad. Sci. (Paris), vol. 146, pp. 530–533, 1908.

[72] C. Luo, A. Narayanaswamy, G. Chen, and J. Joannopoulos, "Thermal radiation from photonic crystals: A direct calculation," Phys. Rev. Lett., vol. 93, p. 213905, 2004.

[73] D. Chan, M. Soljačić, and J. Joannopoulos, "Direct calculation of thermal emission for three-dimensionally periodic photonic crystal slabs," Phys. Rev. E, vol. 74, p. 036615, 2006.

[74] F. Marquardt, "An introduction to the basics of dephasing." Available at `http://www.quantum3000.narod.ru/papers/edu/dephasing.pdf`.

[75] P. W. Milonni, The Quantum Vacuum: an introduction to quantum electrodynamics. London: Academic Press, Inc., 1994.

[76] D. Marcuse, "Computer simulation of laser photon fluctuations: Theory of a single-cavity laser," IEEE J. Quantum Electron., vol. 20, pp. 1139–1148, 1984.

[77] D. Marcuse, "Computer simulation of laser photon fluctuations: Single-cavity laser results," IEEE J. Quantum Electron., vol. 20, pp. 1148–1155, 1984.

[78] G. Gray and R. Roy, "Noise in nearly-single-mode semiconductor lasers," Phys. Rev. A, vol. 40, pp. 2452–2462, 1989.

[79] M. Kira, F. Jahnke, W. Hoyer, and S. W. Koch, "Quantum theory of spontaneous emission and coherent effects in semiconductor microstructures," Prog. Quantum Electron., vol. 23, pp. 189–279, 1999.

[80] H. F. Hofmann and O. Hess, "Quantum Maxwell-Bloch equations for spatially inhomogeneous semiconductor lasers," Phys. Rev. A, vol. 59, pp. 2342–2358, 1999.

[81] G. M. Slavcheva, J. M. Arnold, and R. W. Ziolkowski, "FDTD simulation of the nonlinear gain dynamics in active optical waveguides and semiconductor microcavities," IEEE J. Sel. Topics Quantum Electron., vol. 10, pp. 1052–1062, 2004.

[82] C. W. J. Beenakker, "Thermal radiation and amplified spontaneous emission from a random medium," Phys. Rev. Lett., vol. 81, pp. 1829–1832, 1998.

[83] V. Y. Fedorov and S. E. Skipetrov, "Photon noise in a random laser amplifier with fluctuating properties," Phys. Rev. A, vol. 79, p. 063822, 2009.

[84] Photon noise (or "shot noise"), which is fluctuation of intensity measurements due to the counting of discrete packets of light, is not studied in this thesis.

[85] P. Lodahl and A. Lagendijk, "Transport of quantum noise through random media," Phys. Rev. Lett., vol. 94, p. 153905, 2005.

[86] P. Lodahl, A. P. Mosk, and A. Lagendijk, "Spatial quantum correlations in multiple scattered light," Phys. Rev. Lett., vol. 95, p. 173901, 2005.

[87] H. Cao, Y. Ling, J. Y. Xu, C. Q. Cao, and P. Kumar, "Photon statistics of random lasers with resonant feedback," Phys. Rev. Lett., vol. 86, pp. 4524–4527, 2001.

[88] C. Garrod, Statistical Mechanics and Thermodynamics. New York: Oxford University Press, 1995.

[89] M. Planck, "On the law of distribution of energy in the normal spectrum," Annalen der Physik, vol. 4, p. 553, 1901.

[90] H. Haken, Laser Theory. Berlin: Springer-Verlag, 1983.

[91] R. Lang and M. Scully, "Fluctuations in mode locked 'single-mode' laser oscillation," Opt. Commun., vol. 9, p. 331, 1973.

[92] K. Ujihara, "Quantum theory of a one-dimensional laser with output coupling. linear theory," Phys. Rev. A, vol. 16, p. 652, 1977.

[93] B. M. Horton, "Noise-modulated distance measuring systems," Proc. IRE, vol. 47, p. 821, 1959.

[94] I. Theron, E. Walton, S. Gunawan, and L. Cai, "Ultrawide-band noise radar in the VHF/UHF band," IEEE Trans. Antennas Propag., vol. 47, p. 1080, 1999.

[95] K. Yee, "Numerical solution of initial boundary value problems involving Maxwell's equations in isotropic media," IEEE Trans. Antennas Propag., vol. 14, pp. 302–307, 1966.

[96] A. Taflove and S. Hagness, Computational Electrodynamics. Boston: Artech House, 3rd ed., 2005.

[97] C. Guiffaut and K. Mahdjoubi, "A parallel FDTD algorithm using the MPI library," IEEE Trans. Antennas Propag., vol. 43, pp. 94–103, 2001.

[98] M. Snir, S. Otto, S. Huss-Lederman, D. Walker, and J. Dongarra, MPI: The Complete Reference. Cambridge, MA: MIT Press, 2nd ed., 1996.

[99] R. W. Ziolkowski, J. M. Arnold, and D. M. Gogny, "Ultrafast pulse interactions with two-level atoms," Phys. Rev. A, vol. 52, p. 3082, 1995.

[100] R. Liboff, Introductory Quantum Mechanics. Addison Wesley, 4th ed., 2003.

[101] L. Allen and J. H. Eberly, Optical resonance and two-level atoms. New York: Dover Publications, 1987.

[102] A. Yariv, Quantum Electronics. New York, NY: John Wiley & Sons, Inc., 1989.

[103] P. W. Milonni and J. H. Eberly, Lasers. New York: John Wiley & Sons, Inc., 1988.

[104] B. Bidégaray, A. Bourgeade, and D. Reignier, "Introducing physical relaxation terms in Bloch equations," J. Comput. Phys., vol. 170, pp. 603–613, 2001.

[105] B. Bidégaray, "Time discretizations for Maxwell-Bloch equations," Numer. Meth. Part. D. E., vol. 19, pp. 284–300, 2003.

[106] R. Hamming, Numerical Methods for Scientists and Engineers. New York, NY: Dover Publications, Inc., 1986.

[107] M. Born and E. Wolf, Principles of Optics. New York: Pergamon Press, 1975.

[108] J. Jackson, Classical Electrodynamics. New York: John Wiley & Sons, Inc., 3rd ed., 1999.

[109] J. Berenger, "A perfectly matched layer for the absorption of electromagnetic waves," J. Comput. Phys., vol. 114, p. 185, 1994.

[110] A. S. Nagra and R. A. York, "FDTD analysis of wave propagation in nonlinear absorbing and gain media," IEEE Trans. Antennas Propag., vol. 46, pp. 334–340, 1999.

[111] X. Jiang and C. M. Soukoulis, "Time dependent theory for random lasers," Phys. Rev. Lett., vol. 85, p. 70, 2000.

[112] R. Ziolkowski, "Realization of an all-optical triode and diode with a two-level-atom-loaded diffraction grating," Appl. Opt., vol. 36, p. 8547, 1997.

[113] R. Ziolkowski, "The incorporation of microscopic material models into the FDTD approach for ultrafast optical pulse simulations," IEEE Trans. Antennas Propag., vol. 45, p. 375, 1997.

[114] K. Böhringer and O. Hess, "A full-time-domain approach to spatiotemporal dynamics of semiconductor lasers. I. Theoretical formulation," Prog. Quantum Electrcon., vol. 32, pp. 159–246, 2008.

[115] K. Böhringer and O. Hess, "A full-time-domain approach to spatiotemporal dynamics of semiconductor lasers. II. Spatio-temporal dynamics," Prog. Quantum Electrcon., vol. 32, pp. 247–307, 2008.

[116] J. Andreasen, H. Cao, A. Taflove, P. Kumar, and C. qi Cao, "Finite-difference time-domain simulation of thermal noise in open cavities," Phys. Rev. A, vol. 77, p. 023810, 2008.

[117] C. Kittel, Introduction to Solid State Physics. New York: John Wiley & Sons, Inc., 1996.

[118] V. Freilikher, E. Kanzieper, and A. Maradudin, "Coherent scattering enhancement in systems bounded by rough surfaces," Phys. Rep., vol. 288, p. 127, 1997.

[119] M. Brysbaert, "Algorithms for randomness in the behavioral sciences: A tutorial," Behav. Res. Meth. Ins. C., vol. 23, pp. 45–60, 1991.

[120] Y. Kano and E. Wolf, "Temporal coherence of black body radiation," Proc. Phys. Soc., vol. 80, p. 1273, 1962.

[121] E. Wigner, "On the quantum correction for thermodynamic equilibrium," Phys. Rev., vol. 40, pp. 749–759, 1932.

[122] E. C. G. Sudarshan, "Equivalence of semiclassical and quantum mechanical descriptions of statistical light beams," Phys. Rev. Lett., vol. 10, pp. 277–279, 1963.

[123] R. J. Glauber, "Photon correlations," Phys. Rev. Lett., vol. 10, pp. 84–86, 1963.

[124] R. J. Glauber, "Coherent and incoherent states of the radiation field," Phys. Rev., vol. 131, pp. 2766–2788, 1963.

[125] P. D. Drummond and C. W. Gardiner, "Generalised P-representations in quantum optics," J. Phys. A: Math. Gen., vol. 13, pp. 2353–2368, 1980.

[126] P. D. Drummond and M. G. Raymer, "Quantum theory of propagation of nonclassical radiation in a near-resonant medium," Phys. Rev. A, vol. 44, pp. 2072–2085, 1991.

[127] J. L. Skinner and D. Hsu, "Pure dephasing of a two-level system," J. Phys. Chem., vol. 90, pp. 4931–4938, 1986.

[128] M. S. Malcuit, J. J. Maki, D. J. Simpkin, and R. W. Boyd, "Transition from superfluoescence to amplified spontaneous emission," Phys. Rev. Lett., vol. 59, pp. 1189–1192, 1987.

[129] J. J. Maki, M. S. Malcuit, M. G. Raymer, R. W. Boyd, and P. D. Drummond, "Influence of collisional dephasing processes on superfluorescence," Phys. Rev. A, vol. 40, pp. 5135–5142, 1989.

[130] F. Haake, H. King, G. Schröoder, J. Haus, and R. Glauber, "Fluctuations in superfluorescence," Phys. Rev. A., vol. 20, pp. 2047–2063, 1979.

[131] J. Andreasen and H. Cao, "Finite-different time-domain formulation of stochastic noise in macroscopic atomic systems," J. Lightwave Technol., vol. 27, pp. 4530–4535, 2009.

[132] M. Lax, "The theory of laser noise," Proc. SPIE, vol. 1376, pp. 2–20, 1990.

[133] H. Yokoyama, "Physics and device applications of optical microcavities," Science, vol. 256, p. 66, 1992.

[134] D. J. Thouless, "Maximum metallic resistance in thin wires," Phys. Rev. Lett., vol. 39, pp. 1167–1169, 1977.

[135] FFTW. Available at `http://www.fftw.org`.

[136] Fityk. Available at `http://www.unipress.waw.pl/fityk`.

[137] W. H. Press, B. P. Flannery, S. A. Teukolsky, and W. T. Vetterling, Numerical Recipes in FORTRAN 77. Cambridge: Cambridge University Press, 1992.

[138] R. V. Ambartsumian, P. G. Kryukov, and V. S. Letokhov, "Emission statistics of a laser with nonresonant feedback," JETP Lett., vol. 5, pp. 312–314, 1967.

[139] R. V. Ambartsumian, P. G. Kryukov, V. S. Letokhov, and Y. A. Matveyets, "Statistical emission properties of a nonresonant feedback laser," Sov. Phys. JETP, vol. 26, pp. 1109–1114, 1968.

[140] V. S. Letokhov, "Quantum statistics of multiple-mode emission of an atomic ensemble," Sov. Phys. JETP, vol. 26, p. 1246, 1968.

[141] G. Zacharakis, N. A. Papadogiannis, G. Filippidis, and T. G. Papazoglou, "Photon statistics of laserlike emission from polymeric scattering gain media," Opt. Lett., vol. 25, pp. 923–925, 2000.

[142] F. DeMartini and G. R. Jacobovitz, "Anomalous spontaneousstimulated-decay phase transition and zero-threshold laser action in a microscopic cavity," Phys. Rev. Lett., vol. 60, p. 1711, 1988.

[143] G. Björk and Y. Yamamoto, "Analysis of semiconductor microcavity lasers using rate equations," IEEE J. Quantum Electron., vol. 27, pp. 2386–2396, 1991.

[144] F. DeMartini, F. Cairo, P. Mataloni, and F. Verezegnassi, "Thresholdless microlaser," Phys. Rev. A, vol. 46, p. 4220, 1992.

[145] Y. Yamamoto, S. Machida, and G. Björk, "Micro-cavity semiconductor lasers with controlled spontaneous emission," Opt. Quantum Electron., vol. 24, pp. S215–S243, 1992.

[146] Y. Yamamoto and R. E. Slusher, "Optical processes in microcavities," Phys. Today, vol. 46, pp. 66–73, 1993.

[147] X. Wang, R. A. Linke, G. Devlin, and H. Yokoyama, "Lasing threshold behavior of microcavities: observation by polarization and spectroscopic measurements," Phys. Rev. A, vol. 47, pp. R2488–R2491, 1993.

[148] T. Kobayashi, T. Segawa, A. Morimoto, and T. Sueta, 1982 (1985). 43rd (46th) fall meeting of the Japanese Society of Applied Physics.

[149] L. Mandel, "Latent heat of a homogeneously broadened two-mode laser," Opt. Commun., vol. 42, pp. 356–359, 1982.

[150] P. R. Rice and H. J. Carmichael, "Photon statistics of a cavity-QED laser: A comment on the laserphase-transition analogy," Phys. Rev. A, vol. 50, p. 4318, 1994.

[151] R. Jin, D. Boggavarapu, M. S. III, P. Meystre, H. M. Gibbs, and G. Khitrova, "Photon-number correlations near the threshold of microcavity lasers in the weak-coupled regime," Phys. Rev. A, vol. 49, pp. 4038–4042, 1994.

[152] Z. G. Xie, S. Götzinger, W. Fang, H. Cao, and G. S. Solomon, "Influence of a single quantum dot state on the characteristics of a microdisk laser," Phys. Rev. Lett., vol. 98, p. 117401, 2007.

[153] P. Sperber, W. Spangler, B. Meier, and A. Penzkofer, "Experimental and theoretical investigation of tunable picosecond pulse generation in longitudinally pumped dye laser generators and amplifiers," Opt. Qauntum Electron., vol. 20, pp. 395–431, 1988.

[154] I. D. W. Samuel, E. B. Namdas, and G. A. Turnbull, "How to recognize lasing," Nat. Photonics, vol. 3, p. 546, 2009.

[155] B. E. A. Saleh and M. C. Teich, Fundamentals of Photonics. New York: John Wiley & Sons, Inc., 1991.

[156] H. Cao, J. Y. Xu, S.-H. Chang, and S. T. Ho, "Transition from amplified spontaneous emission to laser action in strongly scattering media," Phys. Rev. E, vol. 61, p. 1985, 2000.

[157] M. Lax in Physics of Quantum Electronics (P. L. Kelly, B. Lax, and P. E. Tannenwald, eds.), New York: McGraw Hill, 1966.

[158] C. H. Henry, "Theory of the linewidth of semiconductor lasers," IEEE J. Quantum Electron., vol. 18, pp. 259–264, 1982.

[159] W. Elsässer and E. O. Göbel, "Dependence of the linewidth of a semiconductor laser on the mode distribution," IEEE J. Quantum Electron., vol. 21, pp. 687–692, 1985.

[160] U. Krüger and K. Petermann, "Dependence of the linewidth of a semiconductor laser on the mode distribution," IEEE J. Quantum Electron., vol. 26, pp. 2058–2064, 1990.

[161] G. V. Soest, M. Tomita, and A. Lagendijk, "Amplifying volume in scattering media," Opt. Lett., vol. 24, p. 306, 1999.

[162] I. McMackin, C. Radzewicz, M. Beck, and M. G. Raymer, "Instabilities and chaos in a multimode, standing-wave, cw dye laser," Phys. Rev. A, vol. 38, pp. 820–833, 1988.

[163] B. Das, G. M. Alman, N. B. Abraham, and E. B. Rockower, "Intensity fluctuations and cross correlations in coupled-mode optical systems," Phys. Rev. A, vol. 39, pp. 5153–5162, 1989.

[164] P. Lett, W. Christian, S. Singh, and L. Mandel, "Macroscopic quantum fluctuations and first-order phase transition in a laser," Phys. Rev. Lett., vol. 47, pp. 1892–1895, 1981.

[165] S. Singh, "Statistical properties of single-mode and two-mode ring lasers," Phys. Rep., vol. 108, pp. 217–273, 1984.

[166] R. Roy, R. Short, J. Durnin, and L. Mandel, "First-passage-time distributions under the influence of quantum fluctuations in a laser," Phys. Rev. Lett., vol. 45, p. 1486, 1980.

[167] X. Jiang, Q. Li, and C. M. Soukoulis, "Symmetry between absorption and amplification in disordered media," Phys. Rev. B, vol. 59, p. R9007, 1999.

[168] S. Zhang, B. Hu, Y. Lockerman, P. Sebbah, and A. Z. Genack, "Observation of singularities in multiply scattered microwave fields," J. Opt. Soc. Am. A, vol. 24, p. A33, 2007.

[169] B. I. Halperin, "Statistical mechanics of topological defects," in Physics of Defects (R. Balian, M. Kleman, and J. P. Poirier, eds.), Amsterdam: North-Holland, 1981.

[170] P. T. Leung, S. S. Tong, and K. Young, "Two-component eigenfunction expansion for open systems described by the wave equation I: completeness of expansion," J. Phys. A, vol. 30, p. 2139, 1997.

[171] P. T. Leung, S. S. Tong, and K. Young, "Two-component eigenfunction expansion for open systems described by the wave equation II: linear space structure," J. Phys. A, vol. 30, p. 2153, 1997.

[172] U. Kuhl, F. M. Izrailev, and A. A. Krokhin, "Enhancement of localization in one-dimensional random potentials with long-range correlations," Phys. Rev. Lett., vol. 100, p. 126402, 2008.

[173] K. Y. Bliokh, Y. P. Bliokh, and V. D. Freilikher, "Resonances in one-dimensional disordered systems: localization of energy and resonant transmission," J. Opt. Soc. Am. B, vol. 21, p. 113, 2004.

[174] C. Torrence and G. P. Compo, "A practical guide to wavelet analysis," Bull. Amer. Meteorol. Soc., vol. 79, p. 61, 1998.

[175] M. Farge, "Wavelet transforms and their applications to turbulence," Annu. Rev. Fluid Mech., vol. 24, p. 395, 1992.

[176] J. Okołowicz, M. Płoszajczak, and I. Rotter, "Dynamics of quantum systems embedded in a continuum," Phys. Rep., vol. 374, p. 271, 2003.

[177] B. Kramer and A. MacKinnon, "Localization: theory and experiment," Rep. Prog. Phys., vol. 56, p. 1469, 1993.

[178] J. Andreasen and H. Cao, "Creation of new lasing modes with spatially nonuniform gain," Opt. Lett., vol. 34, pp. 3586–3588, 2009.

[179] C. Besse, B. Bidégaray-Fesquet, A. Bourgeade, P. Degond, and O. Saut, "A Maxwell-Bloch model with discrete symmetries for wave propagation in nonlinear crystals: an application to KDP," M2AN Math. Model. Numer. Anal., vol. 38, pp. 321–344, 2004.

[180] A. Bourgeade and O. Saut, "Numerical methods for the bidimensional Maxwell-Bloch equations in nonlinear crystals," J. Comput. Phys., vol. 213, pp. 823–843, 2006.

Vita

Jonathan Andreasen was born in 1981 in Belleville, IL. His undergraduate studies were performed at Illinois State University starting in 1999. During this time he received internships at Argonne National Laboratory, Pacific Northwest National Laboratory, and Peking University. He obtained the Bachelor of Science degree in Computational Physics in 2003 after which he came to Northwestern University. He received the Master of Science degree at Northwestern University in 2005 and began studying lasing and electromagnetic fluctuations in open complex systems under the guidance of Prof. Hui Cao. From 2008–2009 he worked as a visiting assistant in research at Yale University and in 2009 was a visiting student at Université de Nice-Sophia Antipolis. He serves as a reviewer for the Optical Society of America and the MIT Center for Electromagnetic Theory and Applications. He is the author and co-author of several peer-reviewed journal articles listed below:

(1) J. Andreasen and H. Cao, "Creation of New Lasing Modes with Spatially Nonuniform Gain," *Opt. Lett.*, **34**, 3586 (2009).

(2) J. Andreasen, H. Cao, J. Wiersig, A. E. Motter, "Marginally Unstable Periodic Orbits in Semiclassical Mushroom Billiards," *Phys. Rev. Lett.*, **103**, 154101 (2009).

(3) J. Andreasen and H. Cao, "Finite-different time-domain formulation of stochastic noise in macroscopic atomic systems," *J. Lightwave Technol.*, **27**, 4530 (2009).

(4) J. Andreasen, H. Cao, A. Taflove, P. Kumar, and C.-qi Cao, "Finite-Difference Time-Domain Simulation of Thermal Noise in Open Cavities," *Phys. Rev. A*, **77**, 023810 (2008).

(5) X. Wu, J. Andreasen, H. Cao, and A. Yamilov, "Effect of local pumping on random laser modes in one dimension," *J. Opt. Soc. Am. B* **24**, A26-A33 (2007).

(6) S.H. Goderya, N.P. Sajeeth, and J. Andreasen, "Advances in Automated Algorithms for Morphological Classifications of Galaxies Based on Shape Features, " *Proceedings of the Astronomical Data Analysis Software and Systems XIII Conference, Society of the Pacific Conference Series*, **314**, 617 (2003).

(7) J. Andreasen and Q. Ouyang, "Cooperative Trends in Modified Image Scoring Model," *Chin. Phys. Lett.*, **19** 1887 (2002).

(8) F. Lofaj, S.M. Wiederhorn, G.G. Long, B.J. Hockey, P.R. Jemian, L. Browder, J. Andreasen, and U. Tffner, "Non-Cavitation Tensile Creep in Lu-Doped Silicon Nitride," *J. Eur. Ceram. Soc.*, **22** 2479 (2002).